Thesis

A Quantum Gas Microscope of Two-electron Atoms with Fluorescence and Faraday Imaging

by

Ryuta Yamamoto

A dissertation

Presented to the Division of Physics and Astronomy
in the Graduate School of Science of Kyoto University
in partial fulfillment of the requirements
for the doctor degree

August, 2016

Abstract

Ultracold quantum gases in an optical lattice enable us to study a strongly correlated system. The single-site-resolved imaging and the single-site addressing technique, called a quantum gas microscope (QGM), are the very useful tool for studying this system and furthermore for control of single atoms which will have great impacts to a quantum information processing. In fact, a lot of interesting experiments are reported using these techniques. The present QGM techniques, however, have been realized with alkali-metal atoms except for a recent work [1] and it is worth while to extend the applicability of these techniques to atomic species beyond alkali-metal atoms for a further revolution.

In this thesis, we successfully demonstrate a site-resolved imaging of individual bosonic ytterbium (^{174}Yb) atoms in a Hubbard-regime two-dimensional optical lattice with a short lattice constant of 266 nm using two imaging methods – fluorescence and Faraday imaging. In both methods, the strong $^1S_0$-$^1P_1$ transition of the wavelength $\lambda = 399$ nm is used for high-resolution imaging and the intercombination $^1S_0$-$^3P_1$ transition of the wavelength $\lambda = 556$ nm is simultaneously applied as a narrow-line laser cooling for suppression of the heating by probe light.

In fluorescence imaging, we measure the temperature after imaging process and we successfully achieve a low temperature of $T = 7.4(13)\,\mu$K, corresponding to a mean oscillation quantum number along the horizontal axis of 0.22(4) during imaging process. we detect on average 200 fluorescence photons from a single atom within 400 ms exposure time. We also succeed in preserving atoms at the same optical lattice sites during imaging process and estimate the detection fidelity of 87(2)%. The realization of a QGM of Yb atoms in a Hubbard-regime optical lattice with enough fidelity opens up the possibilities for studying various kinds of quantum many-body systems such as Bose and Fermi gases, and their mixtures, and also long-range-interacting systems such as Rydberg states.

In Faraday imaging, we detect the polarization rotation of probe light of single atoms with a polarizing beam splitter placed in front of CCD camera. we successfully demonstrate a site-resolved imaging with the Faraday effect and the observed Faraday rotation angle reaches 3.0(2) degrees for a single atom. Differently from a fluorescence imaging, a site-resolved imaging using

the Faraday effect enables us to suppress the heating by the probe light at a large detuning of the probe light and the linearly increasing feature of the ratio of Faraday signal strength S to photon scattering rate Γ_{sc} at a large detuning is observed. In addition, we perform the different type of site-resolved imaging such as dark field Faraday imaging (DFFI) and absorption imaging and we reveal the different feature of the spatial distribution of single atoms in these imaging methods. With DFFI which enables us to obtain a back-ground-free signal like a fluorescence imaging, we estimate the detection fidelity of 84(17)% and this detection fidelity is almost the same quality of that of fluorescence imaging. The realization of the non-destructive Faraday QGM will open up the possibilities for quantum control and quantum feedback of individual atoms in a quantum many-body system which will have great impacts to not only the physics of quantum many-body system but also the quantum information processing.

Contents

List of Figures

List of Tables

Chapter 1

Introduction

1.1 Ultracold atoms

The technique of cooling free atoms with radiation pressure of laser beams was first proposed by D. J. Wineland and H. Dehmelt [2], and T. W. Hänsch and A. L. Schawlow [3]. Thanks to the significant performance improvement of a laser system, ions were first trapped by laser cooling technique in 1978 [4, 5]. After that, the laser cooling technique also enabled us to trap neutral atoms in 1985 [6]. Due to the development of methods to cool and trap atoms with laser light, Steven Chu, Claude Cohen-Tannoudji, and William D. Phillips won the Nobel prize in physics in 1997.

Using this laser cooling technique we can cool atoms at very low temperature, typically $\sim \mu$K, and we expected to realize quantum degeneracy, that is, Bose-Einstein condensate (BEC) and Fermi degeneracy (FD). Temperature we can reach by laser cooling is, however, limited by photon recoil energy, typically $\sim 100\,$nK, and experimentally reached temperature is $\sim \mu$K. Moreover, when atom density is much high like BEC, the loss induced by laser light is increased and the creation of BEC with only laser cooling is quite difficult. For solving this problem, cooling lights are cut off after cooling atoms until sufficiently low temperature and then atoms are loaded into a magnetic trap. Atoms are further cooled by selective removal of atoms with high energy and subsequent thermal equilibrium (evaporative cooling technique). As a result, a BEC of dilute quantum gases was first realized in 1995 [7–9] and due to this achievement, Eric A. Cornell, Wolfgang Ketterle, and Carl E. Wieman won the Nobel prize in physics in 2001. A BEC is also realized using an optical dipole trap with a far off-resonant laser light, enabling to trap atomic species other than alkali atoms (e.g. alkaline-earth atom). Note that in contrast with the BEC of liquid helium which is realized under the strongly interacting system, the realized BEC with ultracold dilute gases enables us to study physics of weakly

Table 1.1: List of the realized quantum degeneracy in each atom species. Left: Realized Bose-Einstein condensate in each atom species. Right: Realized Fermi degeneracy in each atom species.

Year	Atom
1995	^{87}Rb [7], ^{7}Li [8], ^{23}Na [9]
1998	^{1}H [10]
2000	^{85}Rb [11]
2001	^{41}K [12], ^{4}He [13, 14]
2003	^{133}Cs [15], ^{174}Yb [16]
2005	^{52}Cr [17]
2007	^{39}K [18], ^{170}Yb [19]
2009	^{40}Ca [20], ^{176}Yb [21], ^{84}Sr [22, 23]
2010	^{86}Sr [24], ^{88}Sr [25]
2011	^{168}Yb [26], ^{164}Dy [27]
2012	^{168}Er [28]
2015	^{160}Dy, ^{162}Dy [29]

Year	Atom
1999	^{40}K [30]
2001	^{6}Li [31, 32]
2007	^{173}Yb [33]
2010	^{171}Yb [34], ^{87}Sr [35, 36]
2012	^{161}Dy [37]
2014	^{167}Er [38]

interacting systems. Similarly, FD is also realized with the same cooling method. I summarize the atom species of successfully creation of BEC and of FD in table 1.1 so far.

1.2 Quantum simulation in an optical lattice

The realization of quantum degeneracy enables us to study many fascinating physics. In 1998, P. Zoller's group first proposed that strongly interacting systems can be realized with ultracold atoms trapped in periodic potential generated by standing wave of laser light (i.e. optical lattice), which leads to Hubbard type lattice models [39]. Although Hubbard model includes only the terms of the on-site interaction $\mathcal{U}$ and the tunneling $\mathcal{J}$ from one site to the nearest neighbors, this toy model gives us the tool for studying many fascinating physics such as magnetism including high-T_c superconductivity. Moreover, we can easily tune the lattice parameters $\mathcal{U}$ and $\mathcal{J}$ of Hubbard model by varying the laser intensity of optical lattices and ultracold atoms in an optical lattice are a versatile tool for the quantum simulation of condensed matter systems. In fact, ultracold atoms in optical lattices have proven extremely

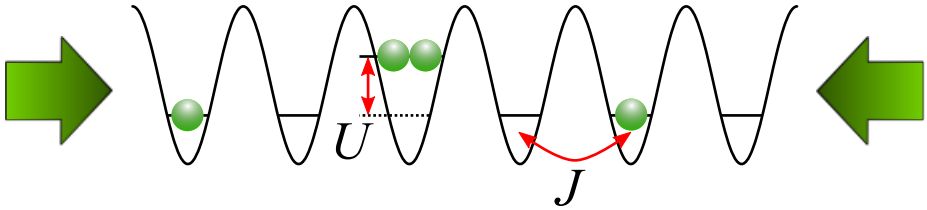

Figure 1.1: Schematics of an optical lattice. Green arrows and green spheres represent the laser lights and the trapped atoms, respectively. $\mathcal{U}$ and $\mathcal{J}$ indicates the on-site interaction and the tunneling matrix element from one site to the adjacent site in a Hubbard model.

useful for the study of quantum phases and the dynamical evolutions of strongly correlated many-body system described by a Hubbard model. Well-known examples include a quantum phase transition from a superfluid (SF) to a Mott insulator (MI) for bosonic species [40–42] and a crossover from a metal to a MI for fermionic species [43, 44].

1.3 Quantum gas microscope

To fully exploit the potential of ultracold atoms in an optical lattice as a quantum simulator, it is great advantage to have access to the in-trap atom distribution with single-atom resolution. In 2007, a site-resolved imaging was realized in ref. [45]. The lattice spacing in this experiment is, however, 4.9 μm which is quite large for studying physics in a Hubbard model.

In contrast, a quantum gas microscope (QGM) with short lattice spacing which enables us to study physics in a Hubbard model has been realized with bosonic ^{87}Rb for the first time in 2009 [46]. In ensuing year, the site-resolved imaging has been used to study the SF to MI transition [47, 48]. In 2011, a single-site addressing with a tightly focused beam was realized [49] and this technique enables us to prepare the arbitrary initial states. Using the realized site-resolved imaging and single-site addressing technique, many fascinating experiments are reported [50–69].

Site-resolved imaging systems have been realized for other alkaline atomic species such as fermionic ^{40}K [70–72] and ^{6}Li [73, 74] atoms very recently. Fermionic QGM will give us the platform for studying many fascinating physics such as magnetism. In fact, the site-resolved observation of metallic, band insulator and Mott insulator states is reported using these systems [75, 76]. Moreover, single-site-resolved spin and charge correlations in 1D chain [77] and 2D plane [78, 79] are reported.

In table 1.2, I summarize the realized QGM experiments so far.

Table 1.2: List of the realized quantum gas microscopes. Note that NA represents the numerical aperture of an objective and the values enclosed in parentheses in the column of NA indicate the enhanced NA with solid immersion lens.

Year	Group	Atom	Cooling	NA (Effective)	Lattice spacing	Resolution (FWHM)	Ref.
2009	M. Greiner (Harvard Univ.)	^{87}Rb (Boson)	PGC[1]	0.55 (0.8)	640 nm	(x) 570 / (y) 630 nm	[46]
2015		^{6}Li (Fermion)	RSC[2]	0.6 (0.87)	569 nm	520 nm	[73]
2010	I. Bloch (MPQ)	^{87}Rb (Boson)	PGC[1]	0.68	532 nm	700 nm	[47]
2015		^{6}Li (Fermion)	RSC[2]	0.5	1.15 μm	895 nm	[74]
2015	M. W. Zwierlein (MIT)	^{40}K (Fermion)	RSC[2]	0.60 (0.87)	541 nm	640 nm	[70]
2015	S. Kuhr (Univ. of Strathclyde)	^{40}K (Fermion)	EITC[3]	0.68	532 nm	630 nm	[71]
2015	J. H. Thywissen (Univ. of Toronto)	^{40}K (Fermion)	EITC[3]	0.8	526.8 nm	600 nm	[72]
2015	M. Kozuma (Tokyo Tech)	^{174}Yb (Boson)	-	0.55 (0.81)	544 nm	(x) 318 / (y) 310 nm	[1]
2016	This work	^{174}Yb (Boson)	SC[4]and DC[5]	0.75	266 nm	364 nm	[80]

[1] Polarization-gradient cooling [81]
[2] Raman sideband cooling [82–89]
[3] Electromagnetically-induced transparency cooling [90, 91]
[4] Sideband cooling [92–94]
[5] Doppler cooling [95]

1.3.1 Quantum gas microscope of ytterbium atom

Extending the applicability of a QGM technique to atomic species beyond alkali-metal atoms is an important step for a further revolution. In particular, a successful application of a QGM technique to two-electron atoms such as alkali-earth metal and ytterbium (Yb) atoms is remarkable because it offers many unique possibilities for the quantum simulation and quantum information researches. In fact, recent studies demonstrate that a system of two-electron atoms in an optical lattice is an ideal platform for the study of SU($\mathcal{N}$) physics [96–99], two-orbital SU($\mathcal{N}$) physics [100–103], and topological physics [104]. In addition, a variety of stable isotopes, 5 bosonic and 2 fermionic isotopes in the case of Yb atoms for example, enables us to study various kinds of many-body systems such as ultracold Bose and Fermi gases and Bose-Bose [26,105], Bose-Fermi [36,105,106], and Fermi-Fermi [97] mixtures in an optical lattice. The existence of nuclear spin degrees of freedom in the ground state $^1S_0$ and long-lived metastable states $^3P_0$ and $^3P_2$ offers unique possibilities for quantum memory and quantum computation [107–110]. Additionally we can tune interatomic interactions between the $^1S_0$ and $^3P_2$ states by an anisotropy-induced magnetic Feshbach resonance [111, 112]. Furthermore, a high-resolution laser spectroscopy of atoms in an optical lattice using the ultranarrow $^1S_0$-$^3P_0$ and $^1S_0$-$^3P_2$ optical transitions is also demonstrated both for bosons and fermions, revealing the novel behavior of the atomic interaction of the system [101–103,111,113,114]. There has been also considerable interest in high-lying Rydberg states of two-electron atoms [115, 116] in an optical lattice [117] because of an additional degrees of freedom for probing and manipulation provided by the remaining valence electron of a singly excited Rydberg state. The successful application of a QGM technique to these systems will definitely enhance our understanding of the physics described in the above.

The important progress towards this direction has been reported quite recently in ref. [1], in which a site-resolved imaging system has been realized without cooling process for bosonic ^{174}Yb atoms in a two-dimensional (2D) optical lattice with a lattice constant of 544 nm. The achieved resolution of $\sim$ 310 nm (full width at half maximum, FWHM) is impressively small. A further study is still necessary, however, to successfully perform the above mentioned interesting researches for Yb atoms using a QGM. First, a crucial aspect of QGM is the high-fidelity of the imaging process characterized by pinned, loss, and hopping rates during the fluorescence imaging, which should be evaluated by comparing two successive images taken for the same atoms. Second, the Hubbard-regime optical lattice needs a shorter lattice constant, especially for heavier atoms of Yb. These conditions should be simultaneously satisfied with the single-site resolved imaging and single-atom sensitivity.

In this work, I achieve site-resolved imaging of individual ^{174}Yb atoms in a 2D

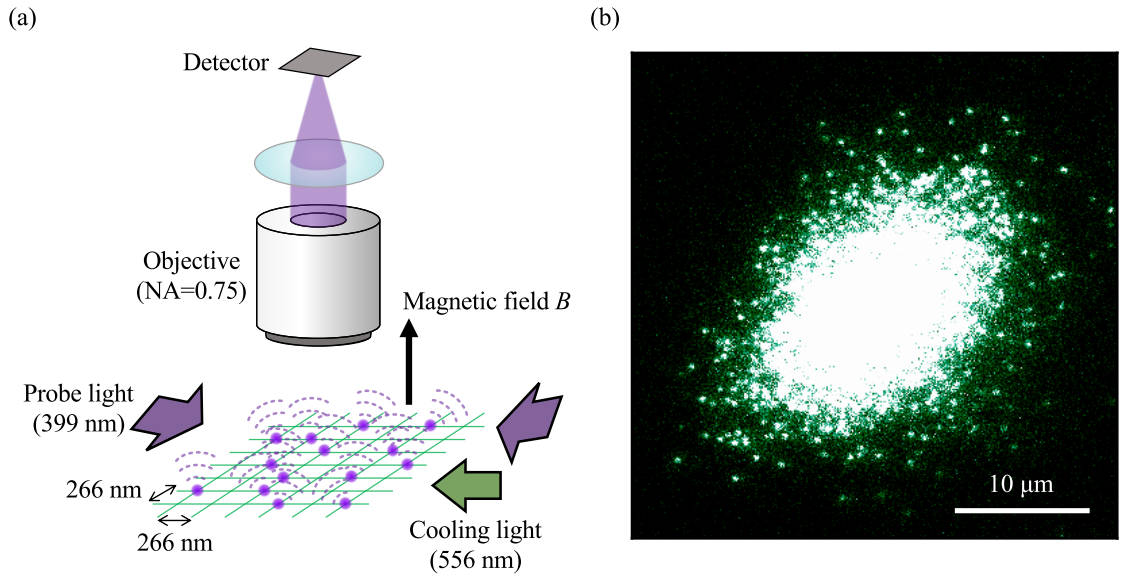

Figure 1.2: QGM with fluorescence imaging. (a) Schematic of site-resolved imaging system for fluorescence imaging. (b) One illustrative example of a QGM with dense atom sample.

optical lattice with a short lattice constant of 266 nm which ensures the Hubbard-regime [118]. To keep atoms at the same lattice sites during the fluorescence imaging, I simultaneously cool atoms by additionally applying narrow-line optical molasses with the $^1S_0$-$^3P_1$ transition ($\lambda = 556\,\mathrm{nm}$, the Doppler limit temperature $T_D = 4.4\,\mu\mathrm{K}$, natural linewidth $\Gamma/2\pi = 182\,\mathrm{kHz}$), resulting in a low temperature of $T = 7.4(13)\,\mu\mathrm{K}$, corresponding to a mean oscillation quantum number along the horizontal axis 0.22(4) during imaging process. In particular, the careful tuning of the relative angle between an applied magnetic field and a polarization of lattice laser beams realizes the cancellation of the inhomogeneity of the light-shifts, which enhances a cooling efficiency of narrow-line laser cooling, both for sideband cooling along the horizontal direction and Doppler cooling along the vertical direction. The realization of such high efficient cooling makes possible to suppress the heating due to the probe light using the $^1S_0$-$^1P_1$ transition ($\lambda = 399\,\mathrm{nm}$, the Doppler limit temperature $T_D = 690\,\mu\mathrm{K}$, natural linewidth $\Gamma/2\pi = 29\,\mathrm{MHz}$) for high-resolution imaging. We achieve a lifetime $\tau > 7\,\mathrm{s}$ of atoms during fluorescence imaging much longer than a typical imaging time of 400 ms, enabling to take multiple images for the same atomic sample and to successfully estimate the imaging fidelity to be 87(2)%. The realization of a QGM with enough fidelity for Yb atoms in a Hubbard-regime optical lattice opens up the possibilities for studying various kinds of quantum many-body systems such as Bose and Fermi gases, and their mixtures in an optical lattice, and also long-range-interacting systems such as Rydberg states.

1.3.2 Site-resolved imaging with the Faraday effect

In the currently developed QGM methods, atoms are measured by detecting fluorescent photons from atoms irradiated with near resonant probe light, resulting in the destruction of the quantum state of atoms such as internal spin states. In addition, the measurement inevitably induces considerable recoil heating, requiring elaborate cooling scheme in a deep optical lattice.

An ultimate quantum measurement and control such as quantum non-demolition (QND) measurement and quantum feedback control is, on the one hand, demonstrated for a single mode of field state with a cavity-quantum-electrodynamics (QED) system [119, 120], for a collective spin ensemble by a dispersive atom-light interaction [121–127], and also for a superconducting quantum bit by a circuit QED system [128]. In order to realize an ultimate quantum measurement and control for each atom in an optical lattice, we need to develop a new detection method of QGM which does not rely on the destructive fluorescent measurement. Promising results along this line were already reported on the detection of a single atom trapped with a tightly-focused laser beam and a single ion in an ion-trap with a dispersive method in ref. [129] and ref. [130], respectively. Here I note that, although the use of an optical cavity provides an intriguing sensitivity for a single atom [131–133], this cannot be simply combined with a QGM technique because a cavity spatial mode determines the spatial resolution and therefore the single-site resolution is not expected.

We report the development of a new detection method of QGM using the dispersive Faraday effect (Faraday QGM), and achieve a site-resolved imaging of single isolated atoms in an optical lattice. The observed Faraday rotation angle reaches 3.0(2) degrees for a single atom. We demonstrate the non-destructive feature of this Faraday imaging method by comparing the detuning dependence of the Faraday signal to that of the photon scattering rate. In addition, we also demonstrate an absorption imaging and a dark field Faraday imaging (DFFI) of QGM, and reveal the different shapes of the point spread functions (PSFs) for these methods, which are fully explained by theoretical analysis. Our result is an important first step towards an ultimate QND measurement and quantum feedback control of a quantum many-body system with a single-site resolution, which will have significant impacts on quantum information processing and the physics of quantum many-body system [134].

1.4 Outline of thesis

- In chapter 1, I introduce the background and the goal of this thesis.

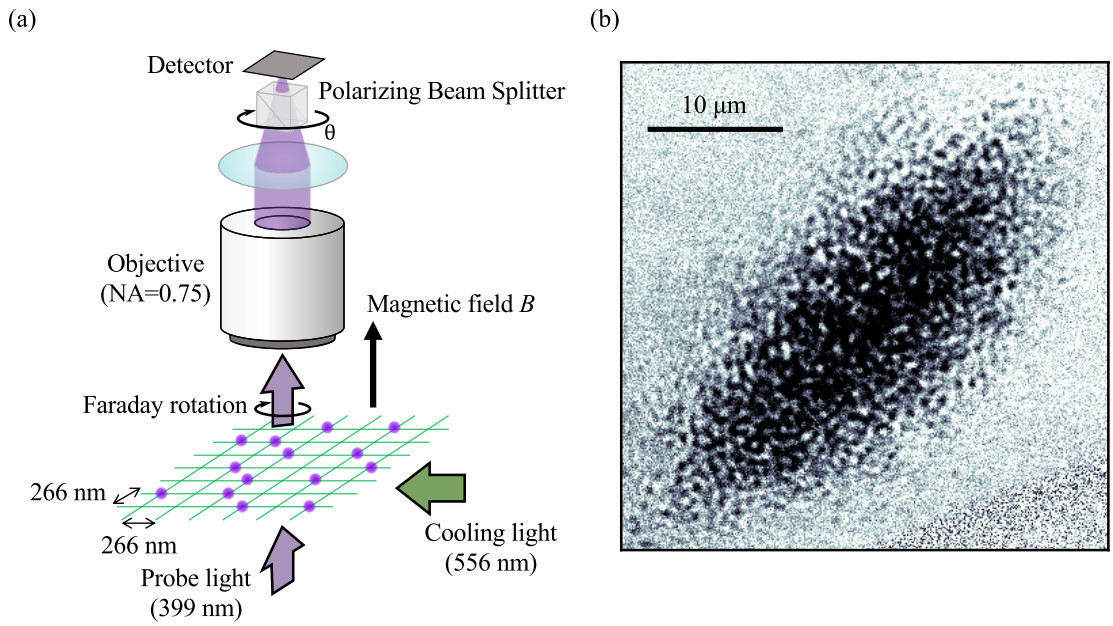

Figure 1.3: QGM with the dispersive Faraday effect. (a) Schematic of site-resolved imaging system for Faraday QGM. (b) One illustrative example of Faraday QGM with dense atom sample.

- In chapter 2, I describe basic properties of ytterbium atoms.
- In chapter 3, I describe theoretical backgrounds for this work.
- In chapter 4, I describe the method for realization of a QGM of bosonic ^{174}Yb atom with fluorescence imaging and estimate the performance of the realized QGM.
- In chapter 5, I describe a new site-resolved imaging method using the dispersive Faraday effect and discuss the performance of the proposed method.
- In chapter 6, I conclude the thesis and discuss prospects on future experiments.

Chapter 2

Ytterbium atom

Ytterbium (Yb) atom is one of rare-earth atoms and the fourteenth element in the lanthanide series. The atomic number of Yb is $Z = 70$. "Ytterbium" was named after the village of "Ytterby" in Sweden. In 1878, Jean Charles Galissard de Marignac discovered a component of Yb and another rare-earth atom, lutetium. In 1907, this component was separated into Yb and lutetium. A pure sample of Yb was obtained only in 1953.

Stable isotopes

Yb atom has rich stable isotopes (seven stable isotopes), differently from alkali atoms. Five of them are bosonic isotopes (^{168}Yb, ^{170}Yb, ^{172}Yb, ^{174}Yb, and ^{176}Yb) and two of them are fermionic isotopes (^{171}Yb and ^{173}Yb). The mass, abundance, nuclear spin I, and magnetic moment μ of each isotope are summarized in table 2.1. So far, all bosonic isotopes except for ^{172}Yb which has a large negative s-wave scattering length and is unstable of BEC are reached in BEC [16, 19, 21, 26]. FD is also realized in both ^{171}Yb [34] and ^{173}Yb [33]. Moreover, the several types of quantum gas mixture (Bose-Bose, Bose-Fermi, and Fermi-Fermi mixtures) are realized in same experimental setup, and, in fact, have been conducted.

Energy levels

The electron configuration of the ground-state Yb atom is denoted as $[\mathrm{Xe}]4f^{14}6s^2$ and Yb atom has two valence electrons. The low-lying energy levels of Yb atom are shown in figure 2.1. The properties of optical transitions for laser cooling and imaging are listed in table 2.2. Likewise, the properties of optical transition for ultranarrow laser spectroscopy are listed in table 2.3.

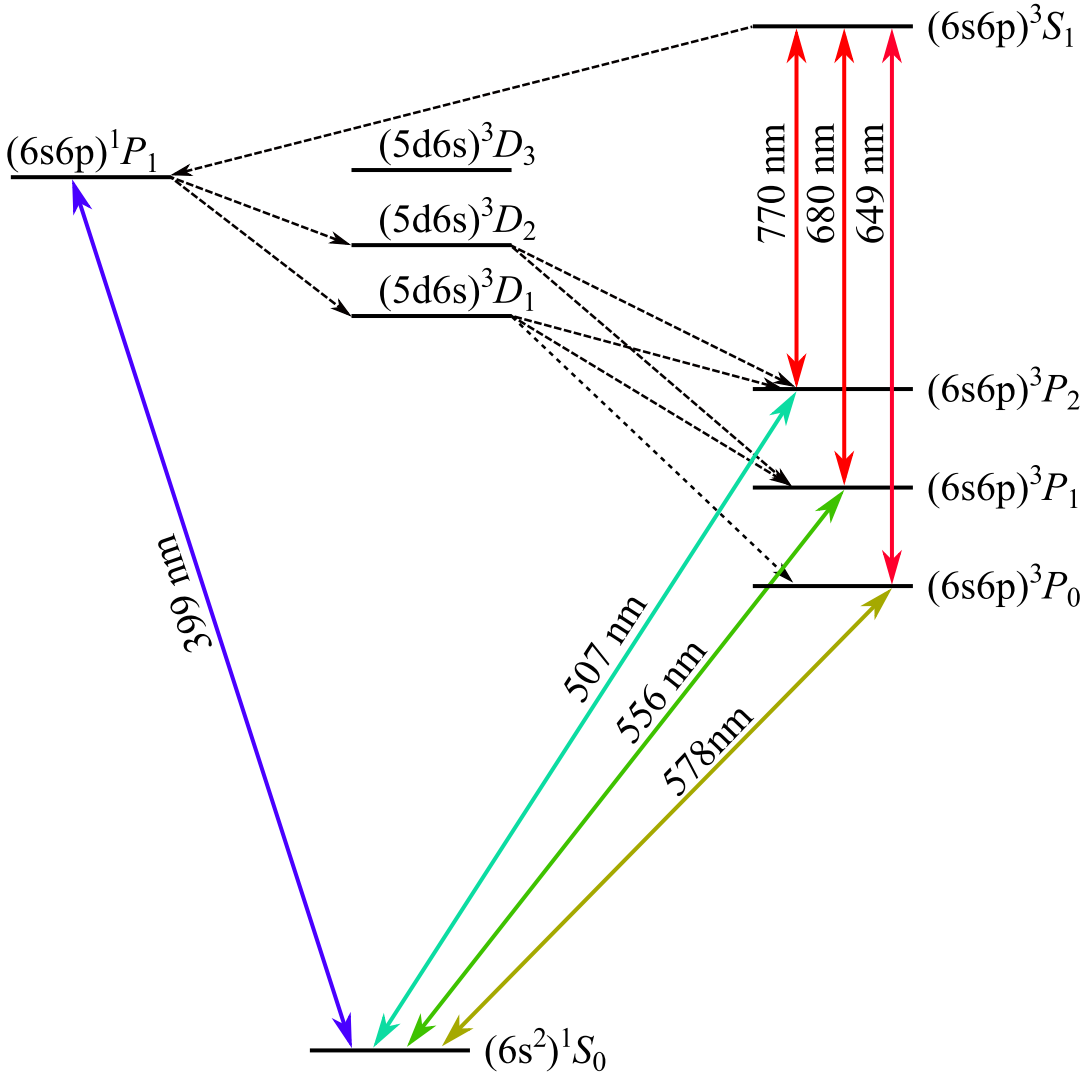

Figure 2.1: Low-lying energy levels of ytterbium atom. Dotted lines indicate the branching of each energy level.

s-wave scattering length

A s-wave scattering length plays quite important role in an ultracold atom experiment because the s-wave scattering length characterize the elastic collisional property between ultracold atoms. Elastic collision is indispensable to evaporative cooling, which is an essential part of generating quantum degenerate gases. Moreover, in the case that s-wave scattering length is negative, BEC is unstable. The s-wave scattering lengths of all Yb isotopes are experimentally determined by a high-resolution two-color photoassociation spectroscopy and mass-scaling law [136] and listed in table 2.4.

Table 2.1: Atomic data for ytterbium [135].

Isotope	Mass (m_u)	Abundance	Nuclear Spin I	Magnetic moment μ (μ_N)
^{168}Yb	167.933894	0.13%	0	
^{170}Yb	169.934759	3.05%	0	
^{171}Yb	170.936323	14.3%	1/2	0.4919
^{172}Yb	171.936378	21.9%	0	
^{173}Yb	172.938208	16.12%	5/2	-0.6776
^{174}Yb	173.938859	31.8%	0	
^{176}Yb	175.942564	12.7%	0	

Table 2.2: Relevant optical transitions for laser cooling and imaging.

	Symbol	$^1S_0$-$^1P_1$	$^1S_0$-$^3P_1$	Unit
Wavelength	λ	398.9	555.8	nm
Lifetime	τ	5.5	875	ns
Natural linewidth	$\frac{\Gamma}{2\pi} = \frac{1}{2\pi\tau}$	28.9	0.182	MHz
Saturation intensity	$I_s = \frac{\pi hc\Gamma}{3\lambda^3}$	59.6	0.138	mW/cm^2
Doppler cooling limit	$T_D = \frac{\hbar\Gamma}{2k_\mathrm{B}}$	694	4.4	μK
Landé g-factor	g_J	1.035	1.49285	

Table 2.3: Relevant optical transitions for ultranarrow spectroscopy.

	Symbol	$^1S_0$-$^3P_2$			Unit
		Boson	^{171}Yb	^{173}Yb	
Wavelength	λ		507.35		nm
Lifetime	τ	15	6.3	7.2	s
Natural linewidth	$\frac{\Gamma}{2\pi} = \frac{1}{2\pi\tau}$	10.6	25	22	mHz
Saturation intensity	$I_s = \frac{\pi hc\Gamma}{3\lambda^3}$	1.1	2.5	2.2	$\times 10^{-8}$ mW/cm^2
Landé g-factor	g_J	1.50			

	Symbol	$^3P_0$-$^3S_1$	$^3P_1$-$^3S_1$	$^3P_2$-$^3S_1$	Unit
Wavelength	λ	649	680.0	769.9	nm
Lifetime	τ	648	233	170	ns
Natural linewidth	$\frac{\Gamma}{2\pi} = \frac{1}{2\pi\tau}$	1.54	2.33	5.89	MHz
Saturation intensity	$I_s = \frac{\pi hc\Gamma}{3\lambda^3}$	0.738	1.79	1.69	mW/cm^2

Table 2.4: Calculated s-wave scattering lengths in nm for Yb isotopic combinations [136].

	^{168}Yb	^{170}Yb	^{171}Yb	^{172}Yb	^{173}Yb	^{174}Yb	^{176}Yb
^{168}Yb	**13.33(18)**	6.19(8)	4.72(9)	3.44(10)	2.04(13)	0.13(18)	-19.0(1.6)
^{170}Yb		**3.38(11)**	1.93(13)	-0.11(19)	-4.30(36)	-27.4(2.7)	11.08(12)
^{171}Yb			**-0.15(19)**	-4.46(36)	-30.6(3.2)	22.7(7)	7.49(8)
^{172}Yb				**-31.7(3.4)**	22.1(7)	10.61(12)	5.62(8)
^{173}Yb					**10.55(11)**	7.34(8)	4.22(10)
^{174}Yb						**5.55(8)**	2.88(12)
^{176}Yb							**-1.28(23)**

Chapter 3

Theoretical background

3.1 Optical dipole trap

An optical dipole trap with a far-off resonant laser beam is very important tool for trapping neutral atoms and generating quantum degenerate gases. For two-level atom with a resonant frequency ω_0, the optical dipole trap with a laser frequency ω is given by [137]

$$U(\boldsymbol{r}) = -3\pi c^2 \frac{\Gamma/\omega_0^2\left(\omega_0^2-\omega^2\right)}{\left(\omega_0^2-\omega^2\right)^2+\left(\omega^3/\omega_0^2\right)^2\Gamma^2} I(\boldsymbol{r}) = -\frac{h}{4}\alpha I(\boldsymbol{r}), \tag{3.1}$$

where Γ, α, and $I(\boldsymbol{r})$ represent a natural linewidth, a polarizability, and a laser intensity, respectively. For Yb atoms, the polarizability of the ground state $^1S_0$ with a wavelength $\lambda = 532\,\mathrm{nm}$ is calculated as $\alpha_g = 37.9\,\mathrm{Hz/(W/cm^2)}$. Note that the calculated polarizability α_g includes the contribution from the $^1P_1$ and $^3P_1$ states.

In most experiment, a Gaussian beam is used for optical dipole trap and its intensity profile is given by

$$I(\boldsymbol{r}) = \frac{2P}{\pi w^2(z)} \exp\left[-2\frac{r^2}{w^2(z)}\right], \tag{3.2}$$

where P is a laser power and $w(z) = w_0\sqrt{1+(z/z_R)^2}$ a beam waist at position z, respectively. Here w_0 and $z_R = \pi w_0^2/\lambda$ indicate a beam waist at focal plane and a Rayleigh length, respectively. By expanding $I(\boldsymbol{r})$ around focus position, we can obtain the trap frequency as

$$\omega_r = \sqrt{\frac{4U_0}{mw_0}}, \omega_z = \sqrt{\frac{2U_0}{mz_R^2}}. \tag{3.3}$$

Here $U_0 = h\alpha I_0/4$ and $I_0 = 2P/\pi w_0^2$.

3.2 Optical lattice

The intensity profile of two laser beams interfered at an angle θ (see figure 3.1) is given by

$$I_{\mathrm{OL}}(\boldsymbol{r}) = \frac{2P}{\pi}\left(\frac{\exp\left[-2\frac{Z^2(\theta/2)+y^2}{w^2(X(\theta/2))}\right]}{w^2(X(\theta/2))} + \frac{\exp\left[-2\frac{Z^2(-\theta/2)+y^2}{w^2(X(-\theta/2))}\right]}{w^2(X(-\theta/2))} + 2\cos(kz\sin\theta/2)\frac{\exp\left[-\frac{Z^2(\theta/2)+y^2}{w^2(X(\theta/2))} - \frac{Z^2(-\theta/2)+y^2}{w^2(X(-\theta/2))}\right]}{w(X(\theta/2))w(X(-\theta/2))}\right), \quad (3.4)$$

where $X(\theta) = x\cos\theta + z\sin\theta$, $Z(\theta) = -x\sin\theta + z\cos\theta$. Note that I assume a laser power, a beam waist, and a focus position of two beams are the same. Using equation (3.1) and (3.4), we can describe the potential of an optical lattice.

Similarly, trap frequency of optical lattice along each axis is also described as

$$\omega_x = \sqrt{\frac{8U_0}{m}\left(\frac{\cos^2\theta/2}{z_R^2} + \frac{2\sin^2\theta/2}{w_0^2}\right)}, \quad (3.5)$$

$$\omega_y = \sqrt{\frac{16U_0}{mw_0^2}}, \quad (3.6)$$

$$\omega_z = \sqrt{\frac{8U_0}{m}\left\{\left(\frac{1}{z_R^2} + k^2\right)\sin^2\frac{\theta}{2} + \frac{2\cos^2\theta/2}{w_0^2}\right\}}. \quad (3.7)$$

In the case of $\theta = \pi$, the two laser beams are counterpropagating and the trap

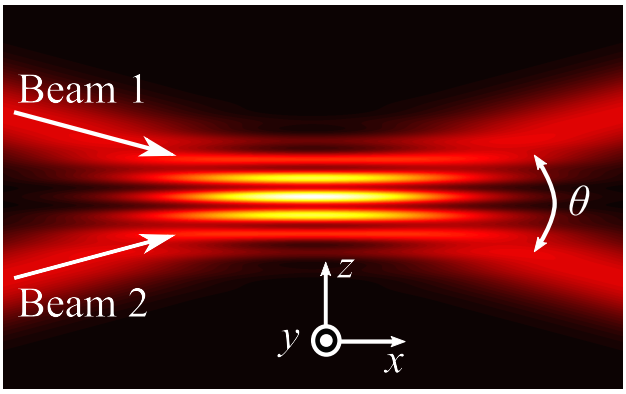

Figure 3.1: Intensity profile of two laser beams interfered at an angle θ.

frequency along each axis can be written as

$$\begin{cases} \omega_x = \omega_y = \sqrt{\dfrac{16U_0}{mw_0^2}}, & (3.8) \\ \omega_z = \sqrt{\dfrac{8U_0}{m}\left(\dfrac{1}{z_R^2} + k^2\right)} \cong \dfrac{2E_R}{\hbar}\sqrt{s}. & (3.9) \end{cases}$$

Here $U_0 = sE_R/4$ and $E_R = \hbar^2 k^2/2m$ is the recoil energy of lattice beam. For Yb atoms, the recoil energy with a wavelength $\lambda = 532\,\mathrm{nm}$ is given by $E_R = h \times 4\,\mathrm{kHz} = k_\mathrm{B} \times 200\,\mathrm{nK}$.

3.3 Light shift (AC Stark shift)

When the hyperfine-structure interaction is much larger than the Zeeman splitting and the Stark interaction, the Stark interaction can be described as [138]

$$\begin{aligned} V^{EE} &= -\frac{h}{4}I\left\{\alpha_{nJ}^S - i\alpha_{nJ}^V \frac{[\boldsymbol{u}^* \times \boldsymbol{u}]\cdot\boldsymbol{J}}{2J}\right. \\ &\quad \left. + \alpha_{nJ}^T \frac{3\left[(\boldsymbol{u}^*\cdot\boldsymbol{J})(\boldsymbol{u}\cdot\boldsymbol{J}) + (\boldsymbol{u}\cdot\boldsymbol{J})(\boldsymbol{u}^*\cdot\boldsymbol{J}) - 2\boldsymbol{J}^2\right]}{2J(2J-1)}\right\}, \end{aligned} \tag{3.10}$$

where α_{nJ}^S, α_{nJ}^V, and α_{nJ}^T are the conventional dynamical scalar, vector, and tensor polarizabilites of the atom in the fine-structure level $|nJ\rangle$, respectively. Furthermore, when the Zeeman splitting is much larger than the light shift and the mixing of different magnetic sublevels m_J can be discarded, the light shift is given as

$$\Delta E = -\frac{h}{4}I\left(\alpha_{nJ}^S + C\alpha_{nJ}^V \frac{m_J}{2J} - D\alpha_{nJ}^T \frac{3m_J^2 - J(J+1)}{2J(2J-1)}\right), \tag{3.11}$$

where $C = |u_{-1}|^2 - |u_1|^2$ and $D = 1 - 3\,|u_0|^2$ with the spherical tensor components $u_{\pm 1}$ and u_0 of $\boldsymbol{u}$. Note that the linearly polarized laser light is applied in most experimental situations and thus $C = 0$ and $D = 1 - 3\cos^2\theta$ where θ is the angle between the quantization axis (parallel to external magnetic field) and the polarization of a laser beam.

The experimentally measured scalar and tensor polarizabilities of the excited $^3P_1$ and $^3P_2$ states of Yb atoms are summarized in table 3.1. With these measured values, the ratio of the polarizability of each excited state to that of the ground state $^1S_0$ in each angle θ can be calculated (see figure 3.2).

Table 3.1: Experimentally measured scalar and tensor polarizabilities of excited states of Yb atoms in a wavelength $\lambda = 532\,\mathrm{nm}$. All values in table are derived using the theoretically calculated polarizability of the ground state $^1S_0$ $\alpha_g = 37.9\,\mathrm{Hz/(W/cm^2)}$. The values of $^3P_2$ state are measured by T. Tomita [139].

	Symbol	$(6s6p)^3P_1$	$(6s6p)^3P_2$	Unit
Scalar	α^S_{nJ}	22.4(2)	46.0(16)	$\mathrm{Hz/(W/cm^2)}$
Tensor	α^T_{nJ}	-7.6(1)	7.5(22)	

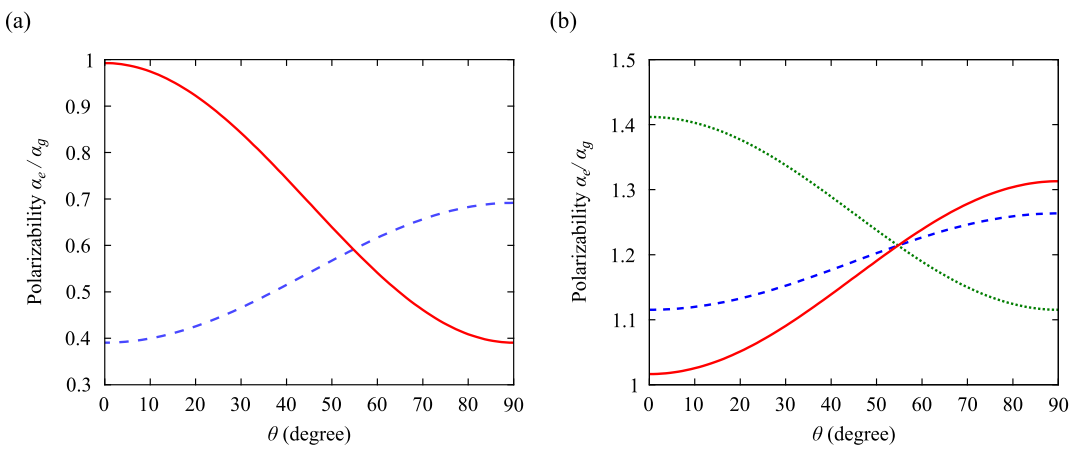

Figure 3.2: Ratio of the theoretically calculated polarizability of each excited state to that of the ground state for bosonic Yb atoms. (a) Ratio of the theoretically calculated polarizability of the $^3P_1$ state to that of the $^1S_0$ state. A red solid and a blue dashed curves represent the polarizabilities of magnetic sublevel $m_J = 0$ and $|m_J| = 1$, respectively. (b) Ratio of the theoretically calculated polarizability of the $^3P_2$ state to that of the $^1S_0$ state. A red solid, a blue dashed, and a green dotted curves represent the polarizabilities of magnetic sublevel $m_J = 0$, $|m_J| = 1$, and $|m_J| = 2$, respectively. α_g and α_e represent the polarizability of the ground and the excited states, respectively. θ indicates the angle between the quantization axis and the polarization of a laser beam.

3.4 Photon collection efficiency

For estimation of the fluorescence signal of single atoms, a photon collection efficiency η is required. In this section, I calculate the photon collection efficiency in two following cases. Here θ is defined as the angle between z-axis and the direction of scattered light, and φ as the angle between x-axis and the projection of scattered light into x-y plane, schematically shown in figure 3.3(a).

Isotropic radiation

An isotropic radiation pattern is quite simple and the photon collection efficiency is given as

$$\eta = \int \mathrm{d}\Omega\ \Phi(\theta,\varphi) = \frac{1}{2}\left(1-\sqrt{1-\mathrm{NA}^2}\right), \tag{3.12}$$

where the radiation probability $\Phi(\theta,\varphi) = (4\pi)^{-1}$, the numerical aperture $\mathrm{NA} \equiv n\sin\theta_0$, and n the index of refraction of the medium.

Dipole radiation

In a dipole radiation pattern, the radiation probability $\Phi(\theta,\varphi)$ can be described as

$$\Phi(\theta,\varphi) = \begin{cases} \dfrac{3}{8\pi}\left(1-\sin^2\theta\cos^2\varphi\right), & (\hat{d}\perp\hat{e}_z) \quad (3.13) \\ \dfrac{3}{8\pi}\left(1-\cos^2\theta\right), & (\hat{d}\parallel\hat{e}_z) \quad (3.14) \end{cases}$$

where $\hat{d}$ represents the unit vector of the electric dipole moment. With these equation, the photon collection efficiency η is given by

$$\eta = \int \mathrm{d}\Omega\ \Phi(\theta,\varphi) = \begin{cases} \dfrac{1}{2}\left[1-\sqrt{1-\mathrm{NA}^2}\left(1-\dfrac{\mathrm{NA}^2}{4}\right)\right], (\hat{d}\perp\hat{e}_z) & (3.15) \\ \dfrac{1}{2}\left[1-\sqrt{1-\mathrm{NA}^2}\left(1+\dfrac{\mathrm{NA}^2}{2}\right)\right].(\hat{d}\parallel\hat{e}_z) & (3.16) \end{cases}$$

The lines in figure 3.3 indicate the calculated results of equation (3.12), (3.15), and (3.16).

3.5 Point spread function

In this section, I introduce a point spread function (PSF) of a single atom. The discussion of resolution of single atom is quite important for a single-site-resolved imaging. Here many textbooks (e.g. ref. [140]) explain the diffraction theory and,

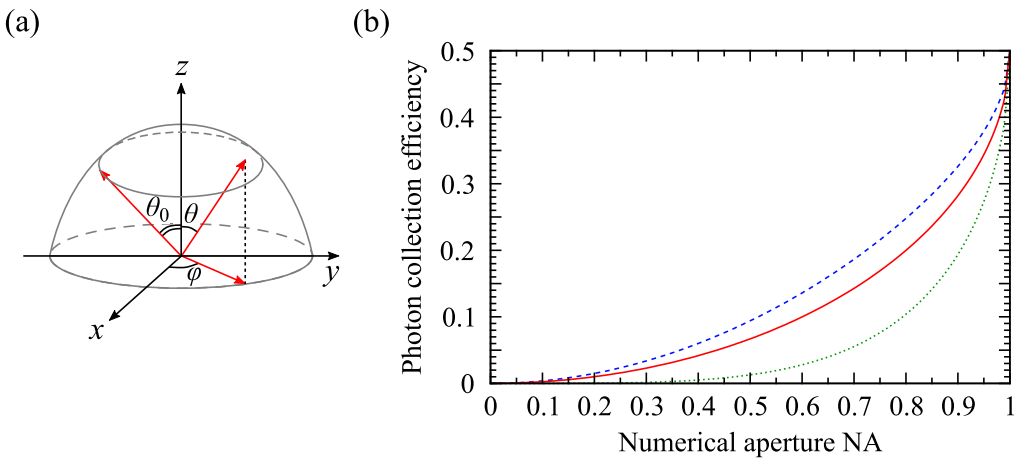

Figure 3.3: Photon collection efficiency. (a) Schematic of coordinate of the point. θ_0 indicates the maximum angle of photon collection. (b) Calculated photon collection efficiency with NA. A red solid curve indicates the photon collection efficiency with an isotropic radiation. A blue dashed and a green dotted line show the photon collection efficiencies with a dipole radiation of $\hat{d} \perp \hat{e}_z$ and $\hat{d} \parallel \hat{e}_z$, respectively. Here $\hat{d}$ represents the unit vector of the electric dipole moment.

in incoherent scattered light, an electric field at imaging plane can be described as

$$E(r) \propto \frac{2J_1(k\mathrm{NA}r)}{k\mathrm{NA}r}, \tag{3.17}$$

where $J_1(x)$ represents Bessel function of the first kind and k the wavenumber of the incident light with a wavelength λ, respectively. Thus, a PSF of single atoms can be given by

$$PSF(r) \propto |E(r)|^2 \propto \left(\frac{2J_1(k\mathrm{NA}r)}{k\mathrm{NA}r}\right)^2. \tag{3.18}$$

On the other hand, a PSF can be well approximated by a Gaussian function as

$$PSF(r) \approx \exp\left[-\frac{r^2}{2\sigma^2}\right], \tag{3.19}$$

where $\sigma \approx 0.349 \times A_0 \approx 0.213 \times \lambda/\mathrm{NA}$. In table 3.2, I summarize the definition of diffraction-limited resolution and the resolutions calculated with $\lambda = 399\,\mathrm{nm}$ and $\mathrm{NA} = 0.75$. Here the Reyleigh's and Sparrow's definitions indicate the resolution of the first zero-crossed point and of the FWHM, respectively. The profiles of equation (3.18) and (3.19) are shown in figure 3.4.

Table 3.2: Diffraction-limited resolution. The resolutions calculated with $\lambda = 399\,\mathrm{nm}$ and $\mathrm{NA} = 0.75$ are shown in right column.

Definition	Symbol	Resolution
Reyleigh	$2A_0 \approx 1.220\frac{\lambda}{\mathrm{NA}}$	649 nm
Sparrow (FWHM)	$2A_1 \approx 0.515\frac{\lambda}{\mathrm{NA}}$	274 nm
Gaussian	$\sigma \approx 0.349 \times A0 \approx 0.213\frac{\lambda}{\mathrm{NA}}$	113 nm

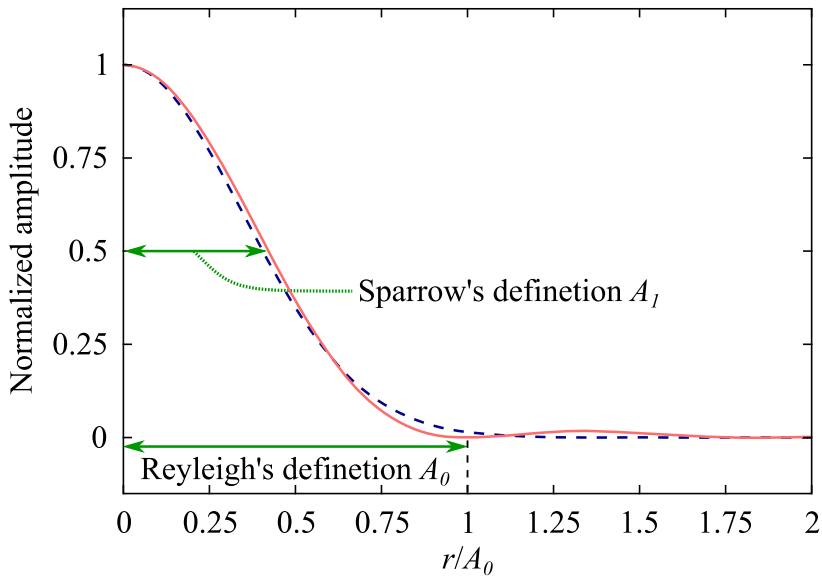

Figure 3.4: Theoretically calculated point spread function (PSF). A red solid and a blue dashed lines show the ideal PSF of equation (3.18) and the approximated Gaussian function of equation (3.19).

Chapter 4

Site-resolved fluorescence imaging

4.1 Experimental setup and atom preparation

Our experiment starts from loading bosonic ^{174}Yb atoms into a magneto-optical trap (MOT) in a metal chamber and transferring the atoms into a glass cell (Schott AG BOROFLOAT) using an optical tweezer (OT). The detail of the MOT and OT setup is described in ref. [141]. The position of atoms in the glass cell is about 5.5 mm below the surface of the glass cell, and just 6.23 mm under a high-resolution objective with numerical aperture of NA = 0.75 (Mitutoyo G Plan Apo HR50x (custom)), which is schematically shown in figure 4.1(b). After creating a BEC of 5×10^4 atoms after 10 s evaporative cooling in a crossed optical trap formed by the OT beam and another 532 nm beam, we load the BEC into a vertical lattice generated by the interference of two laser beams with the wavelength of $\lambda = 532\,\mathrm{nm}$ propagating at a relative angle of $\alpha = 6.2°$. The vertical lattice has a spacing of $\lambda/2\sin(\alpha/2) = 4.9\,\mu\mathrm{m}$ and the trap frequency along the vertical axis (z-axis) of $\omega_z = 2\pi \times 2\,\mathrm{kHz}$ at this loading stage, as explained in detail in ref. [142].

The atoms just after being loaded into the vertical lattice spread over several, typically three, layers, as shown in the left panel of figure 4.2(a). In this situation, although we can focus on the atoms in one selected layer with an objective depth of less than $1\,\mu$m, we always have contributions from the atoms in other layers which considerably blur the image. To observe a clear image for the atoms in only one layer, we blow away the atoms in unnecessary layers. This is done by alternately exciting the atoms into the $^3P_2(m_J = -1)$ state under a bias magnetic field $B_z = 1.4\,\mathrm{G}$ and a magnetic field gradient $\Delta B = 6.2\,\mathrm{mG}/\mu\mathrm{m}$, corresponding to the Zeeman shift $\Delta E_{\mathrm{Zeeman}} = h \times 64\,\mathrm{kHz/layer}$, followed by the rapid inelastic collisional decay and repumping back the atoms into the ground state (see figure 4.2(b)). Here the ultranarrow optical transition of $^1S_0$-$^3P_2(m_J = -1)$ with the resonant wavelength of 507 nm and natural linewidth $\Gamma/2\pi = 10\,\mathrm{mHz}$ is used for the excitation and

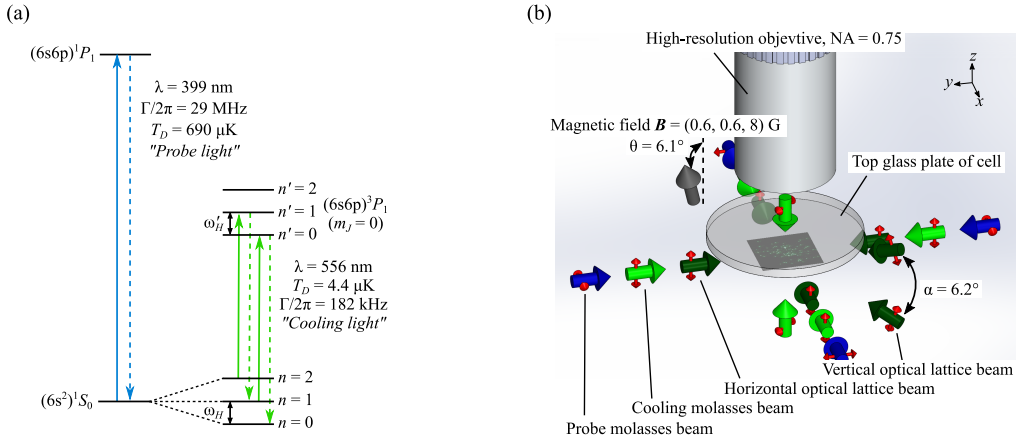

Figure 4.1: (a) Low-lying energy levels of ^{174}Yb atoms relevant for imaging and cooling scheme. The $^1S_0$-$^1P_1$ transition is used for high-resolution imaging and the $^1S_0$-$^3P_1$ transition for high efficient cooling. n and n' show the vibrational level of the $^1S_0$ and $^3P_1(m_J = 0)$ states, respectively. ω_H and ω'_H show the trap frequency along the horizontal lattice of the $^1S_0$ and $^3P_1(m_J = 0)$ states, respectively. (b) Experimental setup for high-resolution imaging in a deep optical lattice. Dark and light green and blue arrows show the direction of lattice, 556 nm cooling molasses, and 399 nm probe molasses beams, respectively. Red arrows show the polarization of each laser beam. The high-resolution objective with NA = 0.75 is just above the glass cell, made of plates with 3 mm thickness. The wavelength of all lattice beams is 532 nm and the beam waists of lattice beams along x, y, and z directions are $(w_x, w_y, w_z) \cong (23, 23, 15)$ μm, respectively.

$^3P_2(m_J = -1)$-$^3S_1$ and $^3P_0$-$^3S_1$ for repumping (see figure 4.2(c)). As a result, we successfully prepare the atoms in only a single layer, as shown in the right panel of figure 4.2(a).

Finally, we load the 2D atom cloud in a single layer into horizontal 2D optical lattices (x- and y-axes) by simultaneously ramping up the potential of the vertical and horizontal optical lattices, where the wavelength of horizontal lattices is $\lambda = 532$ nm and the lattice spacing is 266 nm. The vibrational frequencies along the three axes at the fluorescence imaging stage are $(\omega_x, \omega_y, \omega_z) = 2\pi \times (300, 300, 15.7)$ kHz, corresponding to the lattice depths of $(U_x, U_y, U_z) = k_B \times (300, 300, 250)$ μK, respectively.

Before observation of isolated atoms, we adjust the tilt of the objective using visibility of Moiré pattern between horizontal optical lattices and cooling beams. Here Moiré pattern results from the difference of spacing of two standing waves. We show the result of tilting adjustment of the objective in figure 4.3. Note that we install the tilting adjustment system of the objective and the schematics of the holding jig for imaging system is shown in appendix E.

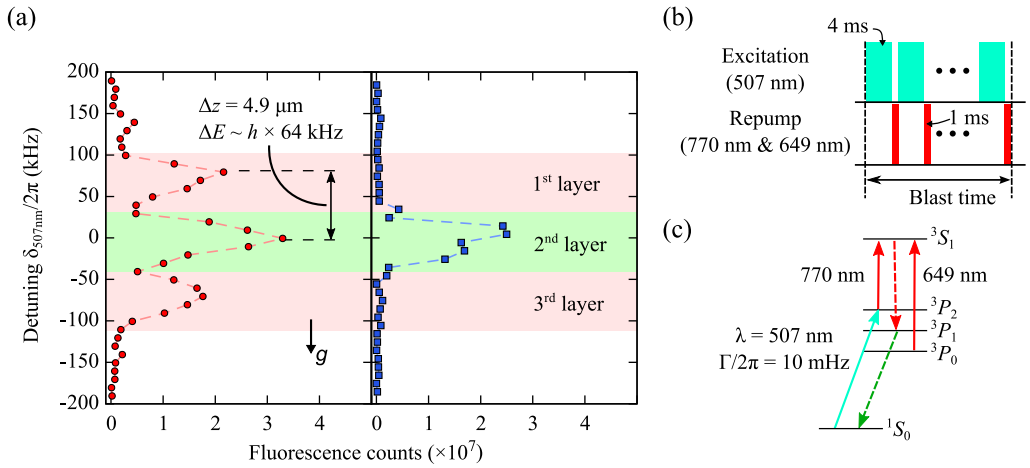

Figure 4.2: Pick up a single layer. (a) Spectroscopy of atoms in the vertical lattice using the $^1S_0$-$^3P_2(m_J = -1)$ transition at a bias magnetic field $B_z = 1.4\,\mathrm{G}$ and a magnetic field gradient $\Delta B = 6.2\,\mathrm{mG}/\mu\mathrm{m}$. The left and right panels show the spectrum without and with blowing away atoms in the additional (1st and 3rd) layers, respectively. A layer separation of $\Delta z = 4.9\,\mu\mathrm{m}$ corresponds to the Zeeman shift $\Delta E_{\mathrm{Zeeman}} = h \times 64\,\mathrm{kHz}$. The arrow with g shows the direction of gravity. (b) Sequence of preparing only atoms in a single-layer (2nd layer). We blow away the atoms trapped in the 1st and 3rd layers by alternately exciting the atoms into the $^3P_2$ state followed by the rapid inelastic collision decay and repumping back them into the $^1S_0$ state. The blast time is typically 250 ms. (c) Low-lying energy levels of ^{174}Yb atoms relevant for blast.

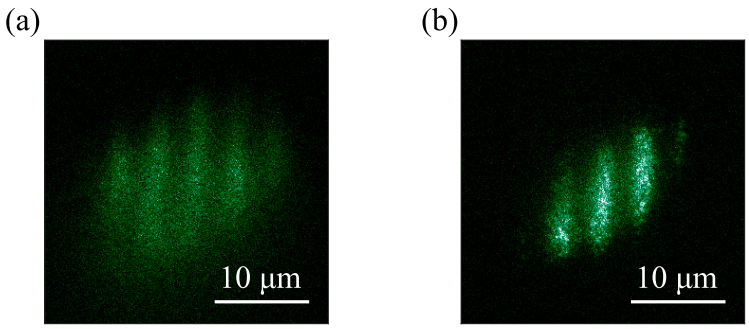

Figure 4.3: Visibility of Moiré pattern between 532 nm optical lattices and 556 nm cooling beams. (a) Misalign of the tilt of objective. The image is blurred. (b) Correctly align of the tilt of objective. Note that we modulate the phase of the standing wave of the 556 nm optical molasses along x-axis by modulating its retro-reflecting mirror.

4.2 Narrow-line laser cooling in an optical lattice

An important prerequisite for realizing a QGM is to preserve the atoms at their sites during fluorescence imaging. The $^1S_0$-$^1P_1$ transition provides high-resolution imaging with the diffraction limited resolution of a FWHM of 274 nm in our system. The high Doppler cooling limit temperature $T_D = 690\,\mu$K, however, makes quite difficult to preserve atoms at their sites. In addition, the lack of hyperfine structure in the ground state $^1S_0$ of bosonic Yb atoms makes impossible to apply sub-Doppler cooling techniques such as polarization-gradient cooling and Raman sideband cooling. To resolve this difficulty, we simultaneously cool the atoms with Doppler and sideband cooling using the $^1S_0$-$^3P_1$ narrow-line transition.

To efficiently cool all the atoms in an optical lattice with the narrow-line transition $^1S_0$-$^3P_1$, we need to suppress the inhomogeneity of light shift between the $^1S_0$ and $^3P_1$ states, otherwise the detuning for cooling is not optimized simultaneously for all atoms. Homogeneous light shifts of the ground and excited states enable us to excite the state from (g, n) to $(e, n-1)$ with any oscillation quantum number n, that is, we can efficiently cool atoms by sideband cooling technique, schematically shown in figure 4.4(a). Note that (g, n) and (e, n) indicate the ground and excited

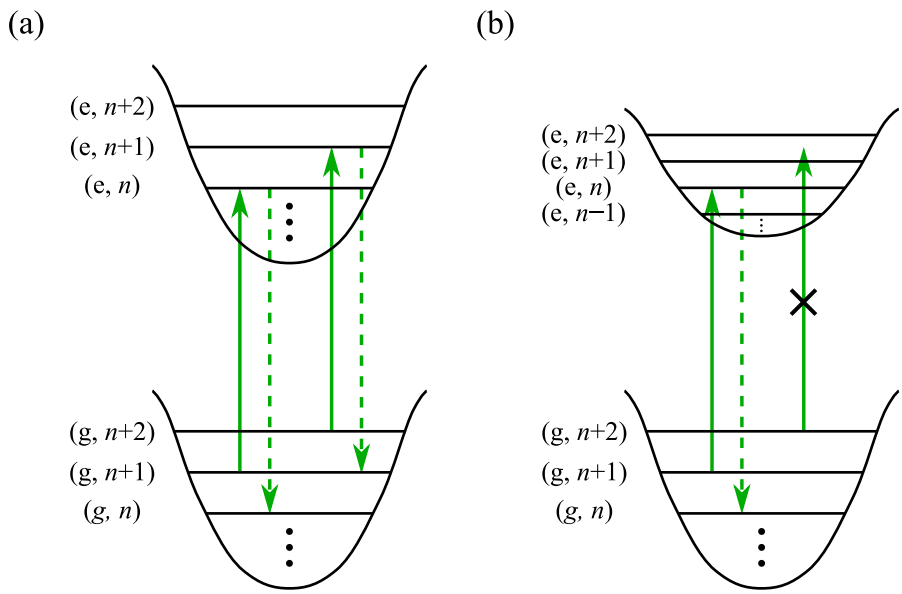

Figure 4.4: Cooling efficiency of sideband cooling with or without potential inhomogeneity between the ground state and excited state. (a) $\alpha_g = \alpha_e$. The (g, n) state with any oscillation quantum number n can be excited to the $(e, n-1)$ state with the same laser frequency. (b) $\alpha_g > \alpha_e$. Only the $(g, n+1)$ state with a certain oscillation quantum number n can be excited to the (e, n) state. Note that (g, n) and (e, n) indicate the ground and excited states with the oscillation quantum number n, respectively.

states with the oscillation quantum number n, respectively. On the other hand, figure 4.4(b) shows the energy levels with the inhomogeneity of light shift between the ground and excited states. In this case, we can only excite the state from $(g, n+1)$ to (e, n) with a certain oscillation quantum number n, resulting in the low cooling efficiency of sideband cooling.

The light shift in the ground state $^1S_0$ is given by $\Delta E_g^L = -(h/4)\alpha_g I$, where I is the laser intensity of the wavelength $\lambda = 532\,\mathrm{nm}$ and $\alpha_g = 37.9\,\mathrm{Hz/(W/cm^2)}$ is the calculated scalar polarizability in the $^1S_0$ state. The light shift in the magnetic sublevel m_J of the $^3P_1$ state is given as [138]

$$\Delta E_e^L = -\frac{h}{4}\alpha_e(m_J, \theta)\ I, \tag{4.1}$$

where

$$\alpha_e(m_J, \theta) = \alpha_e^S - \alpha_e^T \frac{1 - 3\cos^2\theta}{2}(3m_J^2 - 2). \tag{4.2}$$

Here θ is the angle between the quantization axis and the polarization of laser beams, α_e^S and α_e^T are the scalar and tensor polarizabilities in the $^3P_1$ state, respectively. Importantly, equation (4.2) provides the possibility of tuning the polarizability $\alpha_e(m_J, \theta)$ to coincide with α_g by choosing an appropriate angle θ for m_J, thus canceling the light-shift effects of the $^1S_0$-$^3P_1$ transition.

For this possibility we perform a laser spectroscopy with the $^1S_0$-$^3P_1(m_J = 0)$ transition for two different horizontal optical lattice potentials of 500 and 1250 $\mathrm{E_R}$ with angles θ and measure the resonant frequency shift Δf of two horizontal optical lattice potentials. One example of the performed laser spectroscopy is shown in figure 4.5(a). Using equation (4.1), the resonant frequency difference Δf can be written as

$$\Delta f = \frac{750 E_R}{h}\left(\frac{\alpha_e(m_J = 0, \theta)}{\alpha_g} - 1\right). \tag{4.3}$$

In figure 4.5(b), we show the measured resonant frequency shift Δf with several angles θ and the fit result with equation (4.3). As a result, we accurately determine α_e^S and α_e^T as 22.4(2) and $-7.6(1)\,\mathrm{Hz/(W/cm^2)}$, respectively. With these values, our current setup of the polarizations of all the lattice beams parallel to the vertical axis provides $\alpha_e(m_J = 0, \theta = 0)/\alpha_g = 0.99$. In our experiment, however, we slightly tilt a magnetic field from the vertical direction by an angle 6.1° which gives $\alpha_e(m_J = 0, \theta = 6.1°)/\alpha_g = 0.98$. This setup enables us to excite the atoms into the $^3P_1(m_J = 0)$ state, when the polarizations of the 556 nm cooling light along the horizontal axes are set to vertical, and those along the vertical axis horizontal (see figure 4.1(b)). Note that the light shift of the $^1S_0$-$^1P_1$ transition for probing is smaller than the natural linewidth of this transition of 29 MHz, and so it is not a problem. The total

intensities of 399 nm and 556 nm beams correspond to the saturation parameters of $s_{399} \sim 1 \times 10^{-3}$ and $s_{556} \sim 1$, respectively. With this dual molasses, Moiré patterns of about 6 μm pitch are observed as a result of the interference between the cooling molasses beam of 556 nm and the optical lattice of 532 nm. To erase this unwanted Moiré pattern, we modulate the phase of the standing wave of the 556 nm optical molasses by modulating retro-reflecting mirrors via the attached piezo transducers, as explained in detail in ref. [142].

The fine tuning of the relative angle between a magnetic field and lattice laser polarizations indeed gives us a reasonably narrow resonance of the ${}^1S_0$-${}^3P_1(m_J = 0)$ transition for atoms in the optical lattice during fluorescence imaging. Figure 4.6(a) shows the spectra of atoms in our deepest horizontal optical lattices of $U_x = U_y = 1500\,\mathrm{E_R}$, where $E_R = h^2/2m\lambda_L^2 = k_\mathrm{B} \times 200\,\mathrm{nK}$ is recoil energy of lattice beam. The top panel shows the fluorescence counts of 399 nm probe molasses light as a function of a frequency of 556 nm cooling molasses beams along the horizontal axes, in which we simultaneously apply the probe light and weak cooling molasses lights, $s_{399} \sim 1 \times 10^{-3}$ and $s_{556} \sim 0.6$, and we can observe many fluorescence counts during a 400 ms exposure time only when the cooling is efficient at favorable detunings. We obtain the optimal frequency $f_R = -337(18)$ kHz with the width of 318(12) kHz (FWHM). The bottom panel shows the optical density measured by absorption imaging with a 556 nm beam irradiated along the horizontal axis as a function of a frequency of the 556 nm probe light. In this measurement we do not apply 399 nm and 556 nm molasses beams. Note that we set a zero frequency detuning as the resonance frequency of this spectrum. We determine the optimal detuning of cooling beam along the horizontal axes $\delta_{556}/2\pi = f_R = -337(18)$ kHz. The same measurements are done at several horizontal lattice depths of 250 to $1500\,\mathrm{E_R}$, as shown in figure 4.6(b). In our lattice system, Lamb-Dicke parameters are $\eta_\mu = \sqrt{\hbar k^2/(2m\omega_\mu)} = (0.11, 0.11, 0.48)$, where k is a wavevector of 556 nm light, and $\mu = x, y, z$. Although the frequency separation between the cooling sideband f_R and the carrier transition $f = 0$, corresponding to the trap frequencies ω_x and ω_y, is not large enough compared with the natural linewidth of 184 kHz for the 556 nm cooling transition, the responsible cooling mechanism along the x- and y-axes should be sideband cooling because the optimal detuning of cooling beam along the horizontal axis depends on the horizontal lattice trap depth and is consistent with the trap frequency along the horizontal axis, as shown in figure 4.6(c).

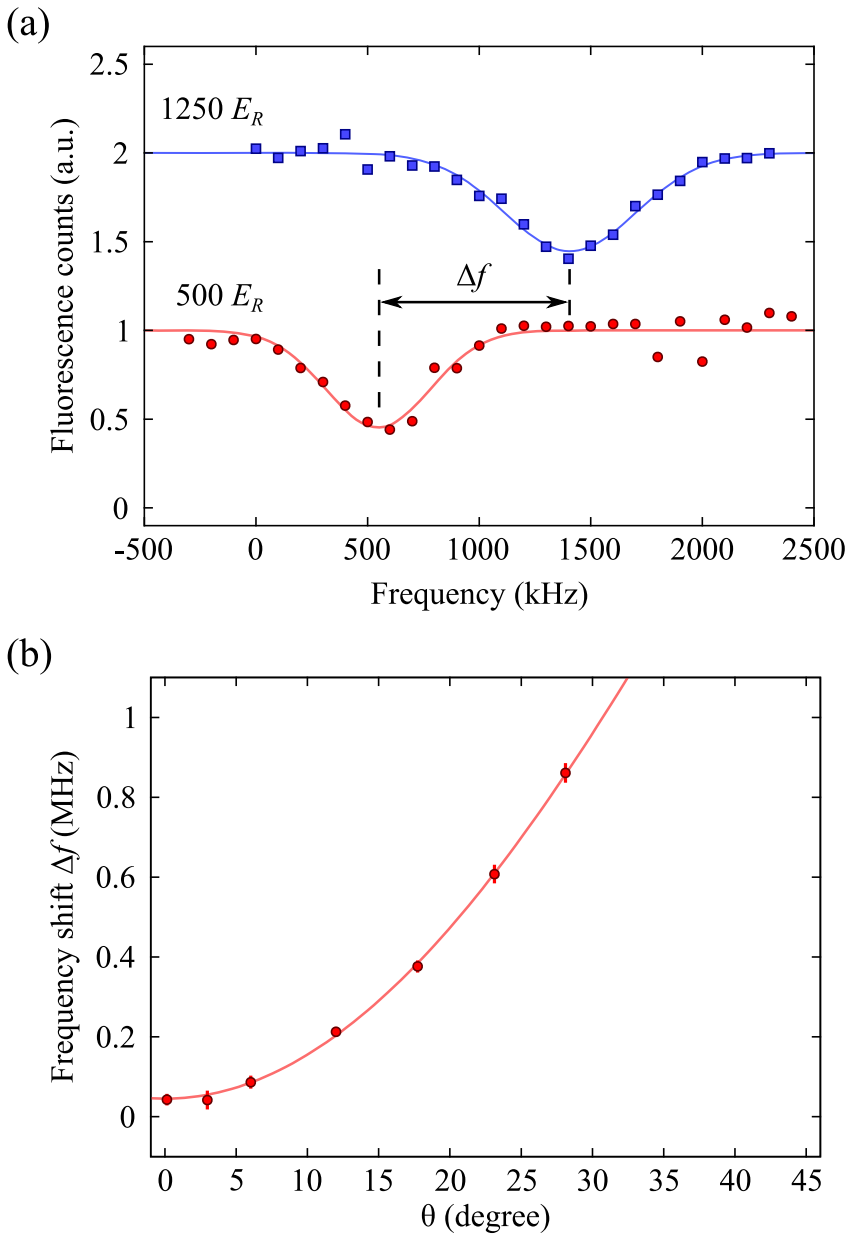

Figure 4.5: Resonant frequency shift Δf of the $^1S_0$-$^3P_1(m_J = 0)$ transition in two different horizontal optical lattices with angles θ. (a) Laser spectroscopy with the $^1S_0$-$^3P_1(m_J = 0)$ transition for two different horizontal optical lattice potentials of $500\,\mathrm{E_R}$ (red circles) and $1250\,\mathrm{E_R}$ (blue squares). A red and blue curves show a fit to the data. (b) Measured resonant frequency shift Δf of the $^1S_0$-$^3P_1(m_J = 0)$ transition with various angles θ. A red curve is a fit with equation (4.3) and yields $\alpha_e^S = 22.4(2)\,\mathrm{Hz/(W/cm^2)}$ and $\alpha_e^T = -7.6(1)\,\mathrm{Hz/(W/cm^2)}$.

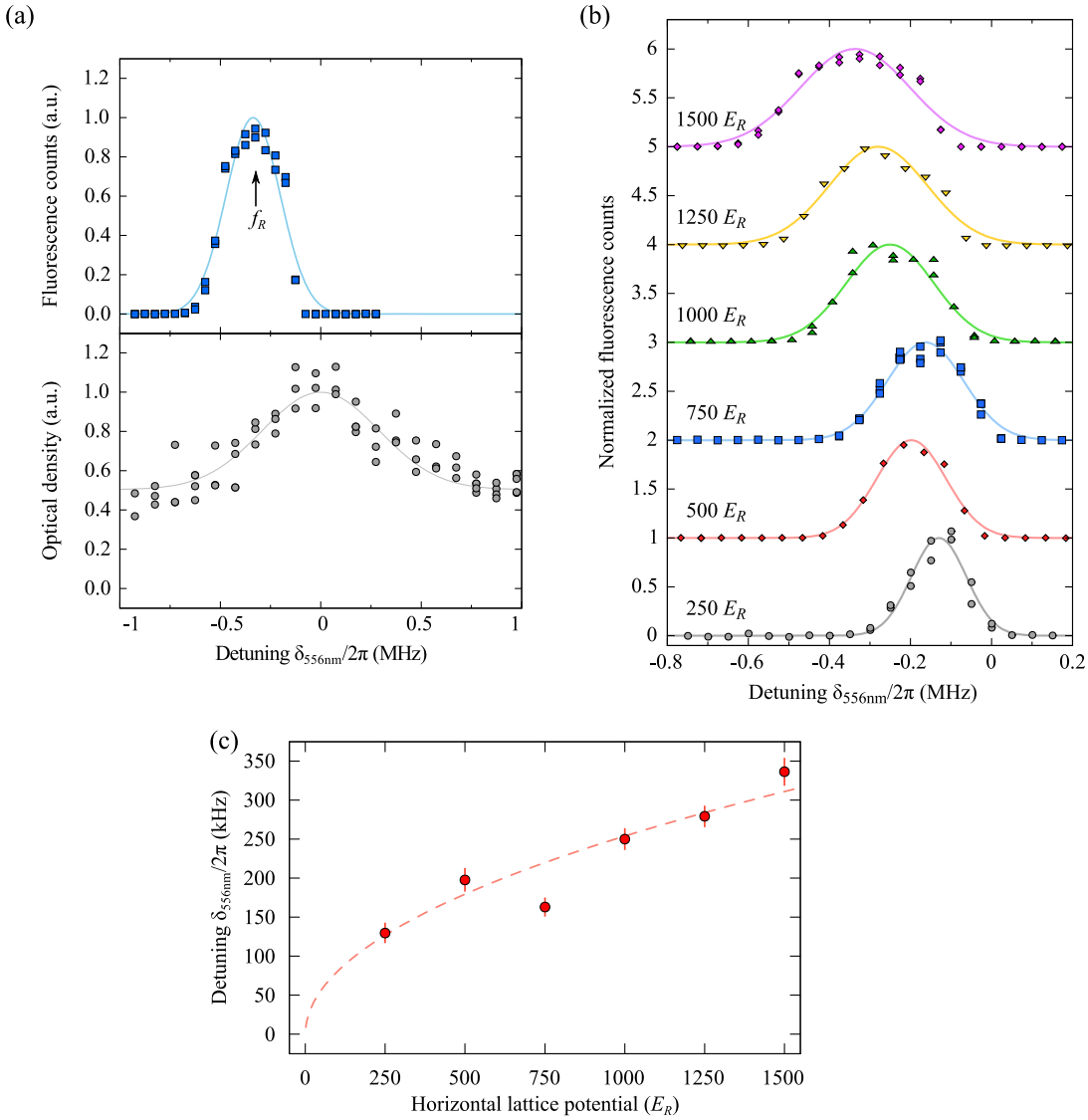

Figure 4.6: Optimal detuning of cooling beam along horizontal axis. (a) Spectra of atoms in a deep optical lattice with $U_x = U_y = 1500\ E_R$ as a function of the detuning $\delta_{556}/2\pi$ of 556 nm cooling molasses along horizontal axes. The top panel (blue squares) shows the fluorescence counts of 399 nm probe molasses with cooling of 556 nm molasses beam along the horizontal axis. The bottom panel (grey circles) shows the optical density measured by absorption imaging with a 556 nm beam irradiated along the horizontal axis. The lines in graphs show fit to the data. (b) Spectra as a function of the detuning $\delta_{556}/2\pi$ of 556 nm cooling molasses along horizontal axes in the horizontal lattice potential depths $U_{x(y)}$ of 250 to 1500 $\mathrm{E_R}$. Solid lines in a graph show fits. (c) Dependence of the optimal detuning of 556 nm cooling molasses on horizontal optical lattice depths. Red circles show the experimental data. A dashed red line shows the calculated trap frequency in an horizontal optical lattice with equation (3.9).

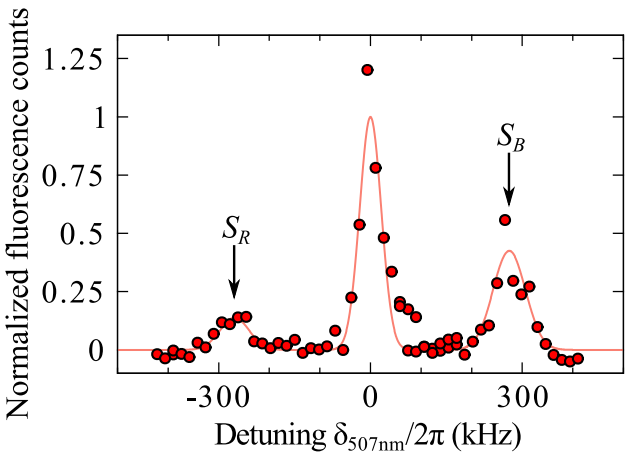

Figure 4.7: Cooling temperature evaluation by ultranarrow laser spectroscopy. Laser spectroscopy of atoms using the ultranarrow $^1S_0$-$^3P_2$ ($m_J = 0$) transition after cooling by sideband (horizontal axis) and Doppler (vertical axis) cooling of 556 nm. The line shows fit to the data. The ratio of the red to the blue sideband peaks S_R/S_B is 0.32(6), and the mean oscillation quantum number along horizontal axis $\langle n \rangle = 0.22(4)$, corresponding to the temperature along horizontal axis $T_H = 7.4(13)\,\mu$K. The error in the determination of the mean vibrational occupation number $\langle n \rangle$ comes from a fitting error of the peak heights of red- and blue-sidebands (S_R and S_B).

The temperature of the atoms during the fluorescence imaging is accurately measured by a laser spectroscopy using the ultranarrow transition $^1S_0$-$^3P_2(m_J = 0)$. Figure 4.7 shows the spectrum obtained, which clearly shows three peaks corresponding to the red- and blue-sidebands and the main carrier. From the ratio of the red to the blue sideband peaks $S_R/S_B = 0.32(6)$, we can evaluate a mean oscillation quantum number in a horizontal optical lattice $\langle n \rangle = (1 - S_R/S_B)^{-1/2} - 1 = 0.22(4)$, corresponding to the atomic temperature of $k_\mathrm{B}T_H = \hbar\omega/\ln(1 + \langle n \rangle^{-1}) = k_\mathrm{B} \times 7.4(13)\,\mu$K [92–94]. The value is in good agreement with the theoretical one of $k_\mathrm{B}T_H = \hbar\omega/\ln(1 + 16\omega^2/5\Gamma^2) = k_\mathrm{B} \times 6.4\,\mu$K based on a sideband cooling theory [93]. Note that this expression is valid for a narrow enough laser linewidth compared to Γ and low enough laser power for no need of considering a saturation effect. The temperature along the vertical direction is measured by a time-of-flight method to be $12(1)\,\mu$K. The optimal detunings are determined for various lattice depths, and are independent of the lattice depth, which suggests that the dominant cooling mechanism is Doppler cooling. This is reasonable if we consider the small trap frequency of 15.7 kHz along the vertical direction compared with the linewidth of 184 kHz.

The unique feature of our scheme is the separation of the cooling and probing processes during the fluorescence imaging. We can therefore study the effect of the cooling beams alone. Here we study the temporal evolution of the temperature

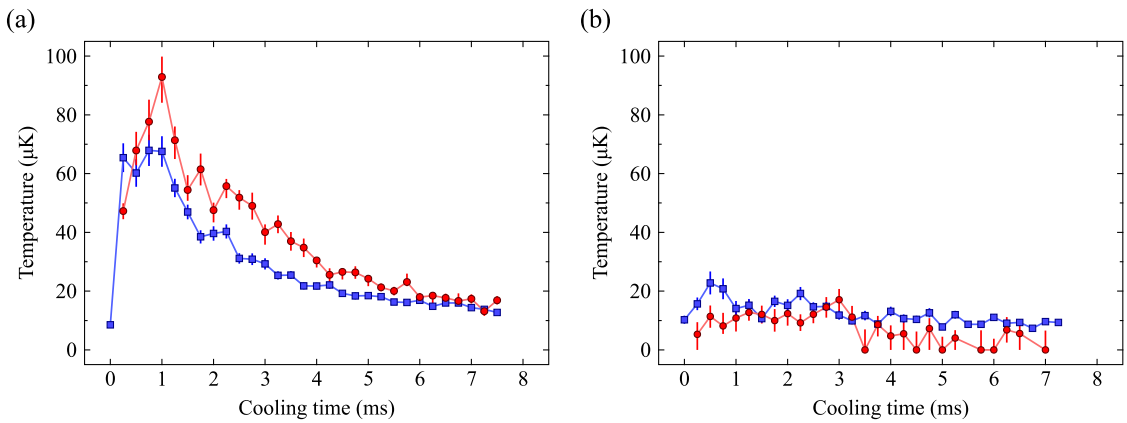

Figure 4.8: Temporal evolution of the temperature (a) without and (b) with applying a PA pulse. In both graphs, temperatures are measured by a time-of-flight method and the red circles and blue squares show the temperature along the horizontal and vertical direction, respectively. Note that probe light is not applied in this measurement. The temperature in (a) is rapidly increased because the atoms in the multiply-occupied sites are heated through the light-assisted collision process, where the atomic loss is not dominant (see the main text). Although the similar trend in (b) as that in (a) could come from the heating by light-assisted collision of a small number of atoms remaining in multiply-occupied sites which was not removed by the PA pulse, it is difficult to discuss the detail of the behavior due to the fluctuations of the data, especially at the temperature lower than 10 μK. Note that the PA pulse is well detuned from atomic resonance and there is essentially no effect on the temperature of the remaining atoms. The error bars show the total error including a fitting and an estimation error.

with narrow-line laser cooling, especially at the early stage of cooling, to investigate what happens during the cooling process. This is especially interesting because the atom loss rate for the light-assisted collision associated with the $^1S_0 + {}^3P_1$ states is small [143] and the atoms in multiply-occupied sites would be heated without loss, differently from the case of alkali atoms. In this measurement, the temperature is measured by a time-of-flight method with absorption imaging. To correctly estimate the temperature along the horizontal axis, we numerically calculate the size of the atom cloud after a time-of-flight, assuming an initial Boltzman occupation of the each vibrational level and a ballistic expansion of the cloud. Figure 4.8(a) shows the results of the measurements. The temperatures rapidly increase within several milliseconds followed by the rather slow decrease towards the steady-state value obtained by the ultranarrow line laser spectroscopy of figure 4.7(c). This behavior is explained as an effect of a light-assisted collision due to the near-resonant cooling light. Namely, atoms in multiply-occupied sites should be heated by release of the kinetic energy subsequent on a light-assisted collision. This is confirmed by further measurements with applying a photoassociation (PA) pulse for removal of multiply-

occupied sites before imaging, shown in figure 4.8(b). In spite of the fluctuation of data, it is clear that the behavior of the temperatures of figure 4.8(b) is different from that of figure 4.8(a). Although all the following single-site resolved imaging data presented in this chapter are measured without the application of PA light, this initial heating effect is negligible because the multiply-occupied sites are almost absent in sparse atomic samples used for our QGM measurement.

4.3 Site-resolved imaging

We image the atomic fluorescence onto the EMCCD camera (Andor iXon^{EM} Blue). In figure 4.9(a) we show one illustrative example of the obtained images. Note that, just before the fluorescence imaging, we intentionally select only about 2% of the atoms for easier evaluation of the performance of the QGM. Such dilution of the atoms is done by performing a weak excitation with the $^1S_0$-$^3P_2(m_J = -1)$ transition, and then returning the atoms back into the ground state $^1S_0$. Figure 4.9(b) shows our measured PSF, obtained by averaging over 10^4 fluorescence images of individual atoms. We find that our PSF can be well approximated by a double Gaussian:

$$PSF(r) = A\left[\exp\left(-\frac{r^2}{2\sigma_1^2}\right) + B\exp\left(-\frac{1}{2}\left(\frac{r-r_0}{\sigma_2}\right)^2\right)\right] + C \tag{4.4}$$

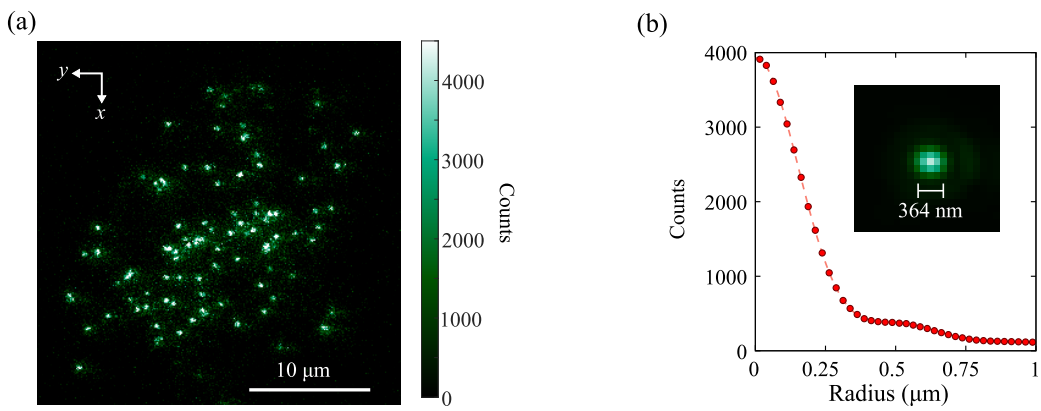

Figure 4.9: Site-resolved fluorescence imaging (a) Site-resolved imaging of ^{174}Yb atoms on a sparsely-filled 266 nm-period optical lattice. (b) The measured PSF averaged over 10^4 individual single atoms and azimuthal average of the PSF. The line is a fit with a double Gaussian of equation equation (4.4) and yields $A = 3850(10)$ counts, $\sigma_1 = 154(1)$ nm, $\sigma_2 = 153(10)$ nm, $r_0 = 516(9)$ nm, $B = 0.068(2)$, and $C = 89(4)$ counts.

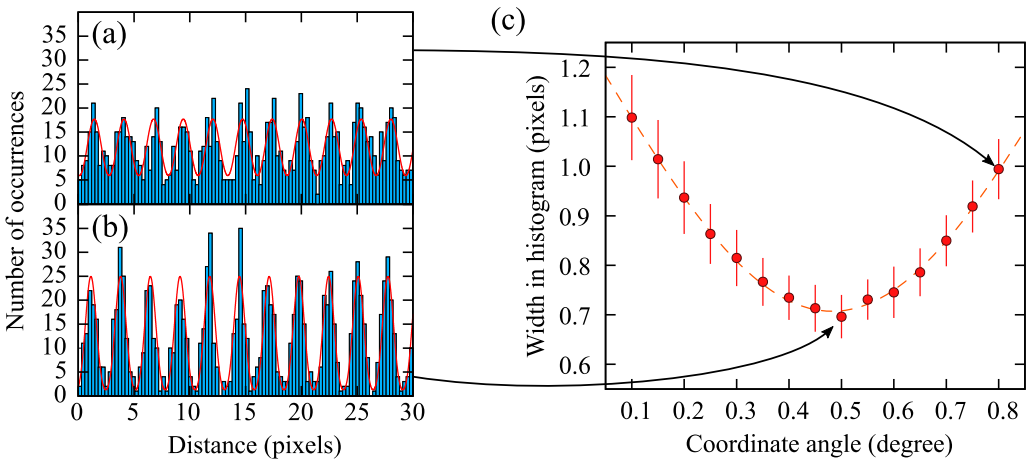

Figure 4.10: Determination of lattice configurations. (a) and (b) The histogram of the mutual distances in the coordination rotated by an angle $\phi = 0.8°$ and $0.5°$, respectively. (c) Determination of lattice angle and spacing. The red dashed line is a fit by $\sigma(\phi) = \sigma_0 \left[1 + \beta \left\{1 - \cos\left(\gamma\left(\phi - \phi_0\right)\right)\right\}\right]$ and yields a minimum width at rotation angle of $\phi_0 = 0.482(3)°$.

with widths σ_1, σ_2, main and relative amplitudes A, B, a spatial offset r_0, and an overall count offset C. The fit result shows our PSF is well described with $\sigma_1 = 154(1)$ nm and $\sigma_2 = 153(10)$ nm, and also has a FWHM of 364 nm, and we detect on average 200 photons per atom within 400 ms fluorescence time. In our imaging system, the spherical aberration remains, making the resolution of PSF worse than ideal one. Our system has a total fluorescence collection efficiency of 6.0%, given by the objective's solid angle of $\Omega/4\pi = 17\%$, 51% total transmission through the imaging optics, and quantum efficiency of 70% of our EMCCD camera. The corresponding atomic fluorescence rate of ~ 8300 photons/s is large enough to unambiguously identify the presence or absence of an atom for each lattice site. Note that the maximum number of detected photons is limited by the cooling rate of the narrow transition [142]. Although the resolution of measured PSF is about 1.4 times larger than the lattice spacing, we successfully determine the atomic distribution by deconvolution of images.

For reconstructing an atom distribution from our obtained image, we first determine a lattice angle and spacing from the isolated, single-site resolved signals [47]. Our lattice axes are oriented approximately along the vertical and horizontal axes with respect to the images. The histogram of the mutual distances in the coordination rotated by a small angle ϕ is shown in figure 4.10(a) and (b). We fit a periodic array of Gaussians to the observed histogram. Figure 4.10(c) shows the width of the Gaussians in the histogram as a function of a coordinate rotation angle. The red dotted line is a fit by $\sigma(\phi) = \sigma_0 \left[1 + \beta \left\{1 - \cos\left(\gamma\left(\phi - \phi_0\right)\right)\right\}\right]$. The minimum width

of the histogram is obtained at the coordinate rotation angle of 0.482(3)° and the lattice constant of 2.66(1) pixels on CCD plane corresponding to the lattice constant of 266 nm. From the same analysis of the other lattice axis, we also obtain the coordinate rotation angle of −0.664(4)° and lattice constant of 2.65(1) pixels on CCD plane corresponding to the lattice constant of 266 nm. Thus, the magnification ratio of our imaging system is 159.7(4) and one pixel of our CCD camera corresponds to 100.2(3) nm on the objective plane. These values are used for the deconvolution analysis of our images.

Here we breifly describe the deconvolution procedure of our fluorescence image [144]. First step is to determine a PSF, a lattice spacing, and a coordinate rotation angle from the isolated, single-site resolved signals, as is explained in the above. From the determined PSF of equation (4.4) and the location of lattice sites, we next calculate a trial image

$$I_{\mathrm{est}}(\boldsymbol{r}, \boldsymbol{\alpha}) = \sum_n \alpha_n PSF\left(|\boldsymbol{r} - \boldsymbol{r}_n|\right), \tag{4.5}$$

where $\boldsymbol{r}$ represents a position in an image plane, $\boldsymbol{r}_n$ a position of a lattice site n, α_n a fitting parameter corresponding to a probability of finding an atom at a lattice site n, and $\boldsymbol{\alpha} = (\alpha_1, \alpha_2, \alpha_3, \cdots, \alpha_n)$. Note that α_n represents a fitted value of a peak fluorescence count at the n-th lattice site. Finally we determine the parameters $\boldsymbol{\alpha}$ by minimizing a quantity $\Delta(\boldsymbol{\alpha}) = \sum_{\boldsymbol{r}} \left(I_{\mathrm{raw}}(\boldsymbol{r}) - I_{\mathrm{est}}(\boldsymbol{r}, \boldsymbol{\alpha})\right)^2$, where $I_{\mathrm{raw}}(\boldsymbol{r})$ is a raw fluorescence image. Figure 4.11(a) shows a raw image of the limited region of Figure 4.9(a) with grid lines showing lattice separation and orientation. In figure 4.11(b), we show a reconstructed atom distribution where red circles and black dots represent the atoms and the lattice sites, respectively. In figure 4.11(c), we also show the reconstructed atom distribution convoluted with the model PSF of equation (4.4), which is compared with the raw image of figure 4.11(a). As a typical example of this deconvolution procedure, we show in figure 4.11(d) a histogram of α_n determined in several regions of 9×9 sites picked up from raw images.

An important aspect of QGM is the high-fidelity of the imaging process characterized by loss and hopping rates during the fluorescence imaging. For this purpose, we take two successive images of the same atoms with 400 ms exposure time and 300 ms delay between the two images, and observe the change in the atom distribution. We precisely tune the detuning δ_H of cooling molasses along the horizontal axes, and evaluate the loss and hopping rates during the fluorescence image from the two successive images. Figure 4.12(a) and (b) show the results of reconstructed atom distributions at $\delta_H/2\pi = -394$ and -206 kHz, respectively. For optimized parameters, we achieve loss rates of 6.5(18)% and hopping rates of 6.7(15)% for 400 ms

exposures of clouds with fillings of ~ 0.02 (see figure 4.12(c)). These rates, which include reconstruction errors, give a detection fidelity of 87(2)% for sparse clouds.

Here we discuss the origins of the measured loss and hopping rates. The thermal hopping cannot explain the observed rates since the average occupation number during the fluorescence imaging is as low as 0.22. Instead, several possible mechanisms can be considered such as the branching from the $^1P_1$ to lower states [145], a vibrational quantum number-changing transition during the absorption and fluorescence cycle of the $^1S_0$-$^1P_1$ transition, and the photon scattering from the $^3P_1$ state due to the 532 nm lattice beams. The loss rate estimated with the lifetime about 10 s during fluorescence imaging is 6.8%. This value is in good agreement with the measured loss rates, shown in figure 4.13. We also note that one of the limiting factors of the lifetime is the irradiation of the 399 nm probe light itself.

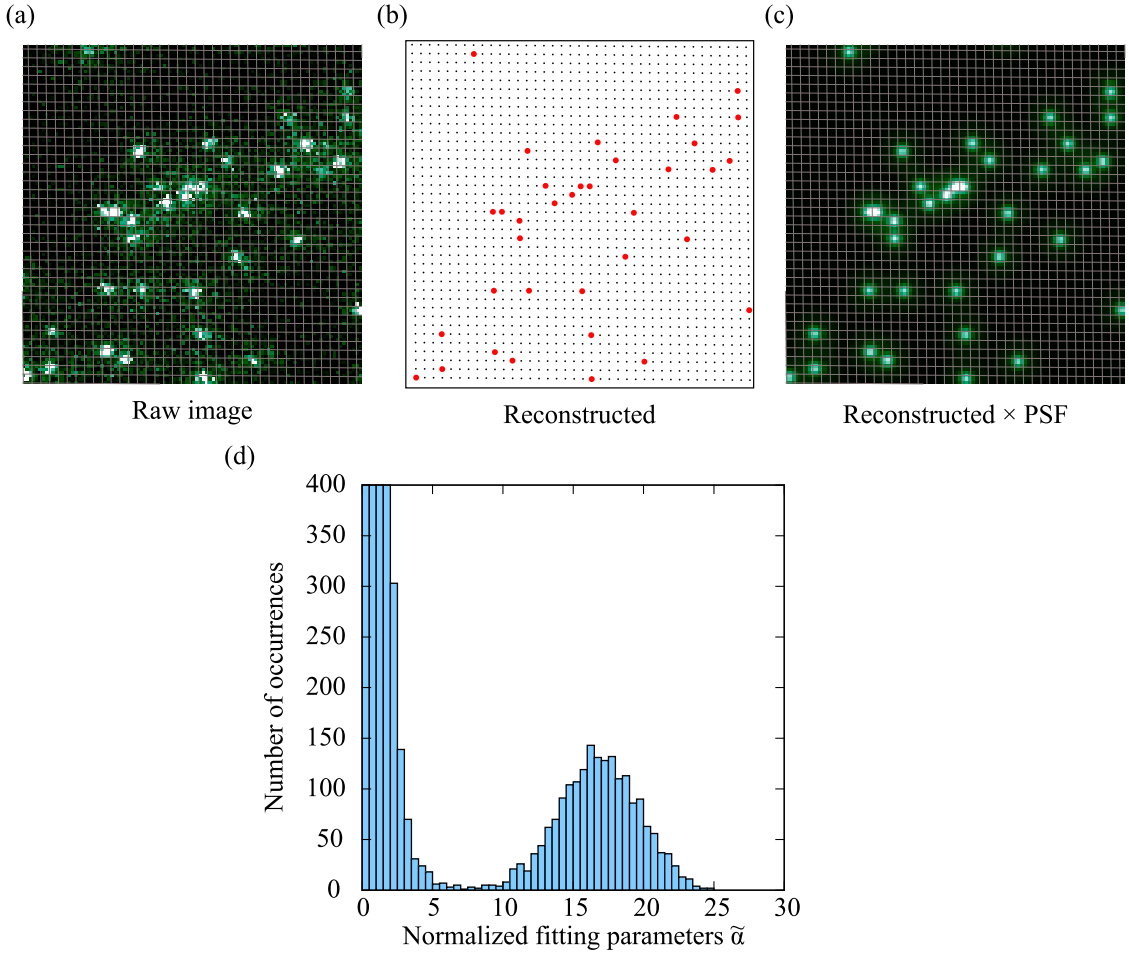

Figure 4.11: Deconvolution of fluorescence imaging. (a) Raw image of sparsely filled lattice with grid lines showing lattice separation and orientation. (b) Reconstructed atom distribution. Red circles and black dots represent the atoms and the lattice sites, respectively. (c) Numerically reconstructed atom distribution on lattice sites. The image is convoluted with the model PSF of equation (4.4) and reconstructed atom distribution of (b). (d) Histogram of normalized fitting parameters $\tilde{\boldsymbol{\alpha}}$ as a result of deconvolution. The left peak corresponds to empty sites, the right peak to those occupied by a single atom. Note that $\tilde{\boldsymbol{\alpha}}$ show the fitting parameters $\boldsymbol{\alpha}$ normalized by a maximum value of $I_{raw}(\boldsymbol{r})$.

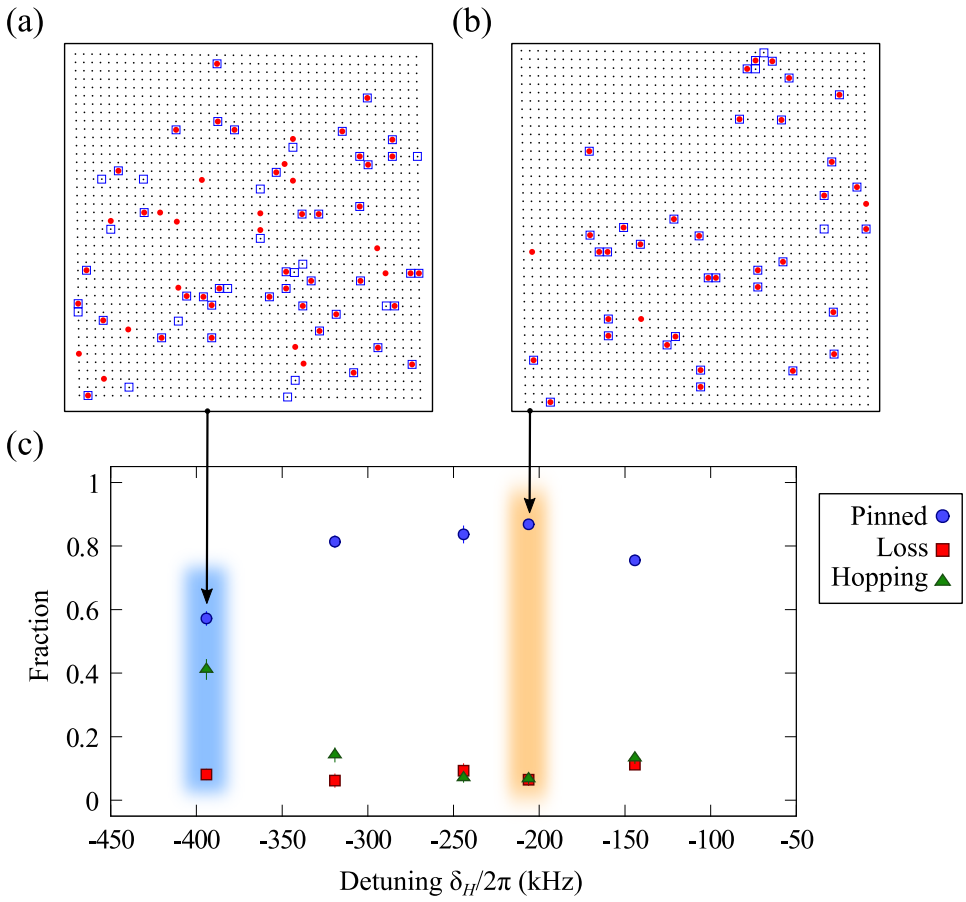

Figure 4.12: Detection fidelity of fluorescence imaging. (a) and (b) Reconstructed atom distributions at $\delta_H/2\pi = -394$ and-206 kHz, respectively. Red circles and blue squares in the panels show the lattice sites occupation of the first and second image, respectively. (c) The pinned, lost, and hopping fractions. The fraction of pinned atoms (blue circles) shows the number of atoms preserved at the same lattice sites in the two successive fluorescence images (400 ms exposure time, 300 ms delay between the two images). The fraction of lost atoms (red squares) shows difference of the number of atoms between the two images. The fraction of hopping atoms (green triangles) shows the number of atoms appearing on a previously empty site in the second image. All fractions are normalized to the number of atoms in the first image.

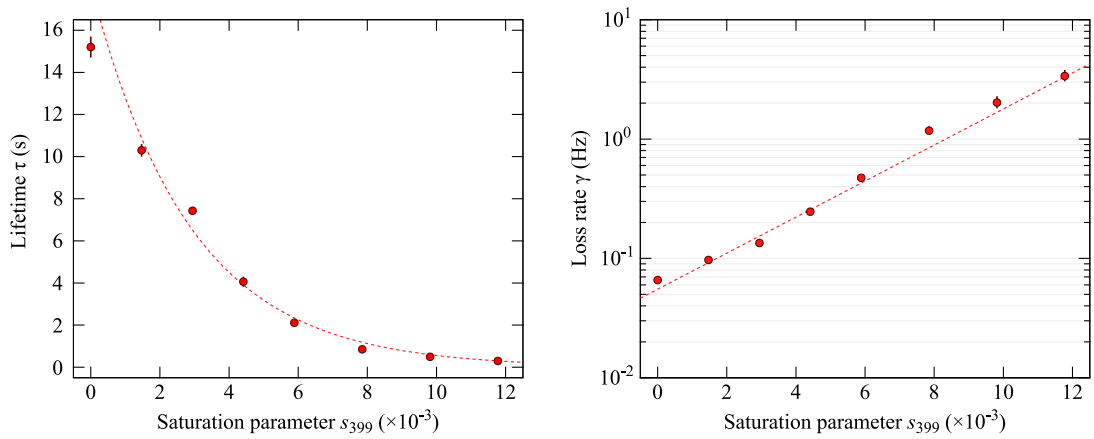

Figure 4.13: Dependence of lifetime on 399 nm probe saturation parameter s_{399}. Left panel shows the dependence of lifetime on intensity of probe beam. Right panel shows the loss rate in each intensity of probe light. A red dotted line in figure shows a fit to the data. Note that we apply 556 nm cooling beam with saturation parameter $s_{556} \sim 1$.

4.4 Conclusion

In conclusion, we demonstrate a bosonic ^{174}Yb QGM in a 2D optical lattice with a short lattice constant of 266 nm. The atoms are preserved in the lattice sites during fluorescence imaging by narrow-line laser cooling which successfully combines Doppler cooling and sideband cooling. The resulting temperature is $T = 7.4(13)\,\mu$K, corresponding to a mean oscillation quantum number along the horizontal axes 0.22(4). The PSF has a reasonably small width comparable to the ideal value, enabling the identification of the presence and absence of atoms by the deconvolution analysis. The high fidelity of the imaging process, which is an important aspect of QGM, is confirmed by the measurement of loss rate of 6.5(18)% and hopping rate of 6.7(15)% for 400 ms exposure time.

While we perform the experiment with bosonic ^{174}Yb atoms, our method is applicable for a QGM for other Yb isotopes, including fermionic ^{171}Yb and ^{173}Yb. In fact, our preliminary result shows that we can successfully obtain site-resolved images for fermionic ^{171}Yb atoms. In addition, the sideband cooling demonstrated in this work can be straightforwardly applied to other alkaline-earth atoms such as strontium, especially for an optical lattice with magic wavelength. The realization of a QGM with enough fidelity for Yb atoms in a Hubbard-regime optical lattice opens up the possibilities for studying various kinds of quantum many-body systems, and also long-range-interacting systems such as Rydberg states.

Chapter 5

Faraday quantum gas microscope

5.1 Experimental setup for Faraday quantum gas microscope

In chapter 4, we demonstrate the site-resolved fluorescence imaging of single isolated atoms with a dual molasses technique. In this chapter, instead of fluorescent photons, we detect a polarization rotation of a linearly polarized probe light transmitted through atoms in a 2D optical lattice with a polarizing beam splitter (PBS) placed in front of a camera, which is schematically shown in figure 5.1. Here θ and $\hat{e}_\theta$ are defined as the angle of a PBS with respect to the incident probe polarization and its unit vector, respectively.

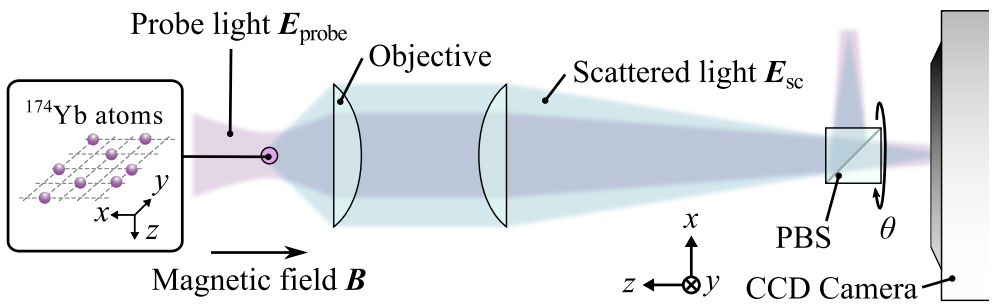

Figure 5.1: Experimental setup for Faraday QGM. We detect a polarization rotation of a linearly polarized probe light of 399 nm transmitted through ^{174}Yb atoms in a 2D optical lattice with a PBS placed in front of a CCD camera. The high-resolution objective with NA = 0.75 is just above the glass cell. The PBS angle θ is set to be $\pi/4$ for the Faraday imaging, and is $\pi/2$ and 0 for DFFI and absorption imaging, respectively.

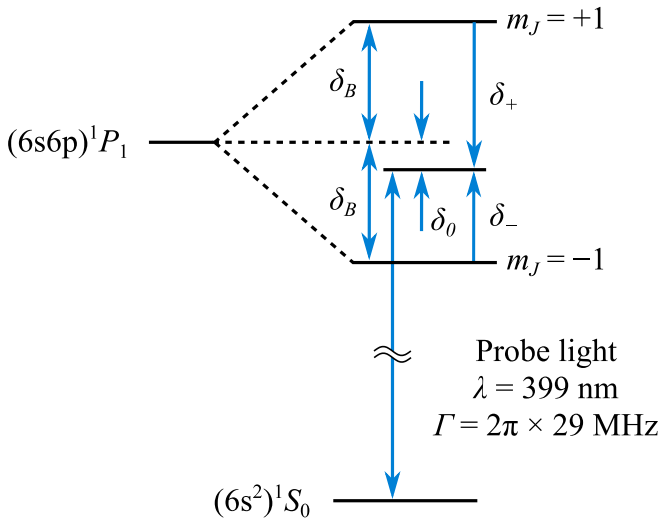

Figure 5.2: Low-lying energy levels of ^{174}Yb atoms relevant for the dispersive Faraday effect. Note that δ_0 and $\delta_\pm$ represents the detuning of a probe laser beam with respect to the $^1S_0$-$^1P_1(m_J = 0)$ and the $^1S_0$-$^1P_1(m_J = \pm 1)$ transition, respectively, and $\delta_B = g_J \mu_B |\boldsymbol{B}| / \hbar$ is a Zeeman shift in the $^1P_1(m_J = \pm 1)$ state due to the magnetic field $\boldsymbol{B}$.

Low-lying energy levels associated with probing of Faraday imaging are shown in figure 5.2. We apply a magnetic field $\boldsymbol{B}$ for inducing a Faraday effect and $\boldsymbol{B}$ is almost parallel to the z-axis which is the propagation direction of a probe beam, shown in figure 5.1. In figure 5.2, The detuning of a probe laser beam with respect to the $^1S_0$-$^1P_1(m_J = \pm 1)$ transition is $\delta_\pm = \delta_0 \mp \delta_B$. Here δ_0 represents the detuning of the probe laser beam with respect to the $^1S_0$-$^1P_1(m_J = 0)$ transition and $\delta_B = g_J \mu_B |\boldsymbol{B}| / \hbar$ is a Zeeman shift in the $^1P_1(m_J = \pm 1)$ state due to the magnetic field $\boldsymbol{B}$, g_J the Landé g-factor of $^1P_1$ state (see table 2.2), and μ_B a Bohr magneton. Since the applied magnetic field is almost parallel to z-axis, we have negligible excitation for $^1S_0$-$^1P_1(m_J = 0)$ transition.

Note that we use bosonic ^{174}Yb atoms loaded into a single layer of 2D optical lattice for Faraday QGM and, to achieve a better signal-to-noise ratio of Faraday QGM, the probe beam has a strong intensity which causes the residual heating effect so that we simultaneously apply cooling beams during imaging process.

5.2 Faraday imaging

In this section, I describe Faraday imaging with the PBS angle $\theta = \pm\pi/4$ where half of the probe light is reflected and the other half is transmitted. In this setup, we can detect a polarization rotation of a linearly polarized probe light with high

sensitivity.

5.2.1 Optical spectrum

We apply a magnetic field of 40 G and measure an optical spectrum of Faraday imaging. The signal amplitude corresponds to the ensemble average of atoms. The Faraday imaging shows a dispersive frequency dependence around the $^1S_0$-$^1P_1(m_J = \pm 1)$ resonances ($\delta_0 = \pm 2\pi \times 58$ MHz), which can be fitted with a following equation:

$$A_{\mathrm{FI}}(\delta_0) = \left| \frac{(\boldsymbol{E}_{\mathrm{probe}} + \boldsymbol{E}_{\mathrm{sc}}(\delta_0)) \cdot \hat{e}_\theta}{\boldsymbol{E}_{\mathrm{probe}} \cdot \hat{e}_\theta} \right|^2, \tag{5.1}$$

where

$$\boldsymbol{E}_{\mathrm{sc}}(\delta_0) \propto \left(\frac{\hat{e}_+}{1 + i2(\delta_0 - \delta_B)/\Gamma} + \frac{\hat{e}_-}{1 + i2(\delta_0 + \delta_B)/\Gamma} \right). \tag{5.2}$$

Here $\boldsymbol{E}_{\mathrm{probe}}$ represents a linearly polarized input probe light and $\boldsymbol{E}_{\mathrm{sc}}(\delta_0)$ an induced scattered electric field. In figure 5.3, a red (blue) curve shows a fit with equation (5.1) with the PBS angle $\theta = \pi/4$ $(-\pi/4)$.

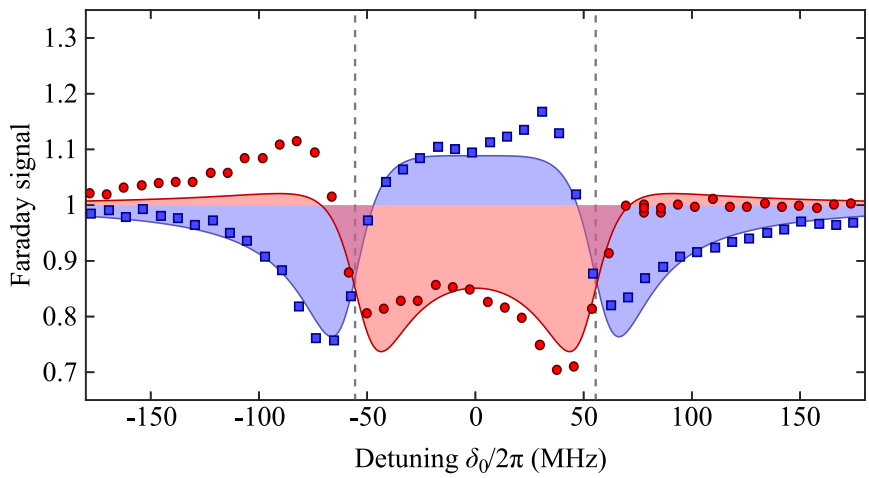

Figure 5.3: Spectrum of Faraday imaging ($\theta = \pm\pi/4$). A magnetic field of a 40 G is applied for Faraday imaging. A red (blue) curve shows a fit with equation (5.1) with the PBS angle $\theta = \pi/4$ $(-\pi/4)$. The signal strength in each spectrum is derived by the analysis of the ensemble average. The resonance positions are indicated by grey dashed lines.

5.2.2 Site-resolved imaging

A polarization rotation due to the Faraday effect for a single atom can be understood as an interference effect between a linearly polarized input probe beam $\boldsymbol{E}_{\mathrm{probe}}(r)$

and an induced scattered electric field by a single atom. Based on a diffraction theory [140] and a scattering theory [146], a scattered field $\boldsymbol{E}_{\mathrm{sc}}(r)$ at a detector is described as

$$\boldsymbol{E}_{\mathrm{sc}}(r) = -\frac{\sqrt{3\eta}}{2}\mathrm{NA}\frac{2J_1(k\mathrm{NA}r)}{k\mathrm{NA}r}E_0\left(\frac{\hat{\boldsymbol{e}}_+}{1-i\left(2\delta_B/\Gamma\right)}+\frac{\hat{\boldsymbol{e}}_-}{1+i\left(2\delta_B/\Gamma\right)}\right), \tag{5.3}$$

where E_0 represents the amplitude of electric field of input probe light, η the photon collection efficiency described in equation (3.15), NA the numerical aperture of objective, $J_1(x)$ the Bessel function of the first kind, k the wavenumber of probe light, and $\hat{\boldsymbol{e}}_\pm$ the polarization unit vector for circularly polarized light $\sigma_\pm$, respectively. Note that we set the PBS angle $\theta = \pi/4$ and the detuning $\delta_0 = 0$. The total detected field $E_{\mathrm{detect}}(r)$ after a PBS is given as $E_{\mathrm{detect}}(r) = [\boldsymbol{E}_{\mathrm{probe}}(r) + \boldsymbol{E}_{\mathrm{sc}}(r)]\cdot\hat{\boldsymbol{e}}_\theta$. Here, in our experimental setup, the beam waist of the probe light is $\sim 37\,\mu$m, much larger than the experimentally measured resolution $\sigma_{\mathrm{exp}} = (k\mathrm{NA}_{\mathrm{exp}})^{-1} = 130\,$nm with $\mathrm{NA}_{\mathrm{exp}} = 0.49$, enabling to consider the distribution of the probe light as uniform. Note that the theoretically predicted resolution $\sigma_{\mathrm{ideal}} = 85\,$nm with NA $= 0.75$. A Faraday image, normalized as one for the background level, can be described as

$$\begin{aligned} I_{\mathrm{FI}}(r) &= \left|E_{\mathrm{detect}}(r)/(E_0/\sqrt{2})\right|^2 \\ &= \left|1-\sqrt{\frac{3\eta}{2}}\mathrm{NA}\frac{1+(2\delta_B/\Gamma)}{1+(2\delta_B/\Gamma)^2}\frac{2J_1(k\mathrm{NA}r)}{k\mathrm{NA}r}\right|^2 \end{aligned} \tag{5.4}$$

It is worthwhile to note that this spatial profile of an image of a single atom, namely the PSF of Faraday imaging, is different from that of the ordinary fluorescence imaging which is given by

$$I_{\mathrm{FL}} \propto \frac{1}{1+(2\delta_B/\Gamma)^2}\left(\frac{2J_1(k\mathrm{NA}r)}{k\mathrm{NA}r}\right)^2. \tag{5.5}$$

The difference clearly comes from the presence or absence of the interference between the probe light $\boldsymbol{E}_{\mathrm{probe}}$ and the scattered light $\boldsymbol{E}_{\mathrm{sc}}$. The interference is absent in a fluorescence image. On the other hand, the interference term $2J_1(x)/x$ is dominant at the PBS angle $\theta = \pm\pi/4$ for a Faraday image.

For easier evaluation of the performance of the site-resolved Faraday imaging, we intentionally select only several percent of the atoms by ultranarrow-line laser spectroscopy of the $^1S_0$-$^3P_2$ transition and prepare a sparse atom cloud for the measurement. In figure 5.4(a), I show one illustrative example of the Faraday imaging and figure 5.4(b) shows the measured PSF, obtained by averaging about 30 isolated individual atoms. We find that our measured PSF of Faraday imaging is well

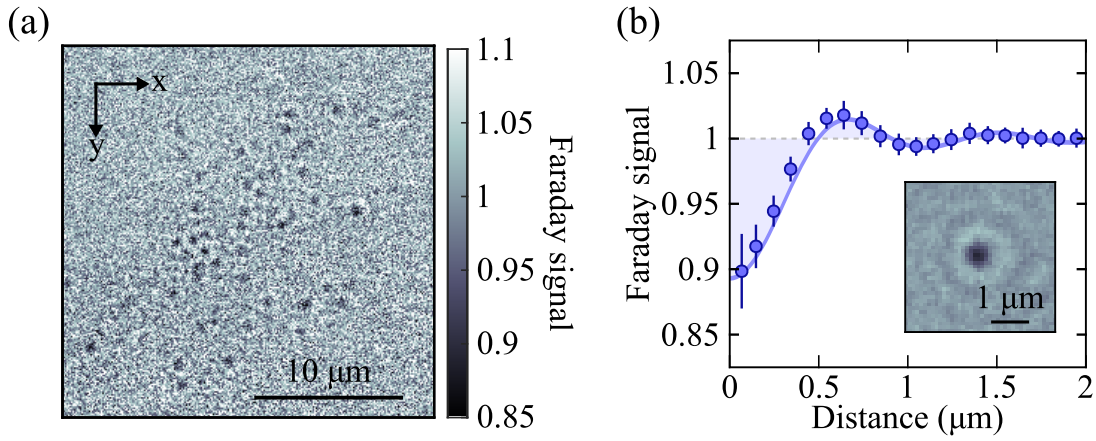

Figure 5.4: Site-resolved Faraday image. (a) One illustrative example of the Faraday imaging. The detuning of the probe beam is $2\pi \times 56\,\mathrm{MHz}$ with the saturation parameter $s_{399} = 0.84 \times 10^{-3}$. The measurement duration is 400 ms. (b) Measured PSF averaged about 30 individual single atoms and azimuthal average of PSF. The blue line is a fit with equation (5.4) with NA = 0.49(2).

fitted with the theoretical formula of equation (5.4) shown as a blue solid line in figure 5.4(b). Note that our Faraday imaging method, if applied to an atomic ensemble, is equivalent to the phase-contrast polarization imaging method developed in ref. [147] and exploited for non-destructive probing of a BEC.

5.2.3 Faraday rotation angle for a single atom

$I_{\mathrm{FI}}(r)$ given in equation (5.4) is also given by $I_{\mathrm{FI}}(r) = \left[\sqrt{2}\cos(\pi/4 + \phi(r))\right]^2$, by introducing a position-dependent Faraday rotation angle $\phi(r)$ defined as

$$\boldsymbol{E}_{\mathrm{total}}(r) = \boldsymbol{E}_{\mathrm{probe}} + \boldsymbol{E}_{\mathrm{sc}}(r) = E_0 \frac{e^{+i\phi(r)}\hat{e}_+ + e^{-i\phi(r)}\hat{e}_-}{\sqrt{2}}. \tag{5.6}$$

Therefore, $\phi(r)$ can be calculated with a following equation:

$$\phi(r) = \cos^{-1}\left[\sqrt{I_{\mathrm{FI}}(r)/2}\right] - \pi/4. \tag{5.7}$$

From the data of figure 5.4(b) and equation (5.7), we evaluate the spatial distribution of the Faraday rotation angle of a single atom and its azimuthal average shown in figure 5.5. The observed Faraday rotation angle reaches 3.0(2) degrees for a single atom with the detuning of $2\pi \times 56\,\mathrm{MHz}$.

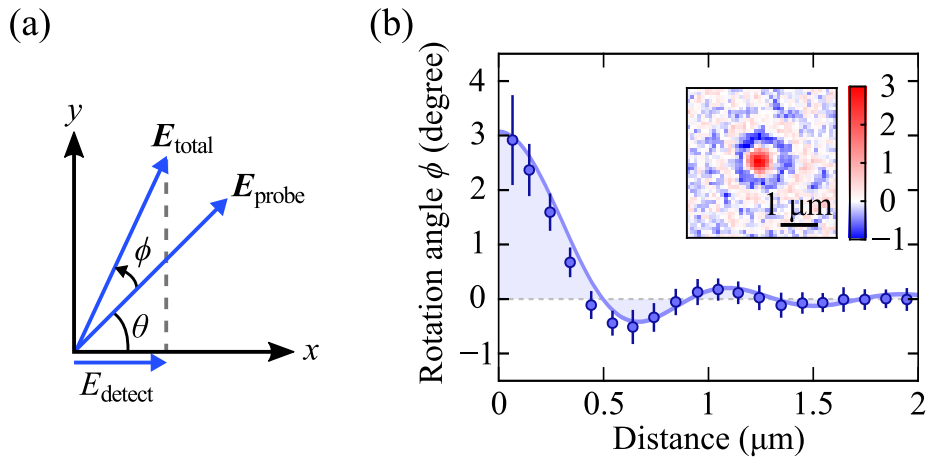

Figure 5.5: Faraday rotation angle of single atom. (a) Schematics of Faraday rotation angle. Note that we can detect only $|E_{\text{detect}}|^2$ in our present imaging system. (b) Azimuthal average of Faraday rotation angle evaluated with equation (5.7). Inset: Spatial distribution of Faraday rotation angle. The detuning of the probe light is $2\pi \times 56\,\text{MHz}$ with the saturation parameter $s_{399} = 0.84 \times 10^{-3}$. A peak Faraday rotation angle reaches 3.0(2) degrees.

5.2.4 Deconvolution of Faraday imaging

For non-destructive measurement with single-site resolution, it is quite important to determine the atom distribution by deconvolution of a Faraday image. We demonstrate the decision of the atom distribution by deconvolution of a Faraday image and successfully determine the atom distribution. Here the basic procedure of the deconvolution is the same as that on fluorescence imaging of QGM, with a PSF of equation (5.4) being the main difference.

In the same condition of figure 5.4, we show a raw image of Faraday imaging in figure 5.6(a), and the reconstructed atom distribution convoluted with the model PSF is shown in figure 5.6(b). A histogram of the fitted amplitudes of the scattered field $\boldsymbol{E}_{\text{sc}}(r)$ in each site is shown in figure 5.6(c) and a black dashed line indicates the chosen threshold value.

On the other hand, we also demonstrate the decision of the atom distribution by deconvolution process of a Faraday image with the detuning of $2\pi \times 10$ MHz with respect to the ${}^1S_0$-${}^3P_1(m_J = -1)$ resonance under the magnetic field of 40 G. This deconvolution result is shown in figure 5.7.

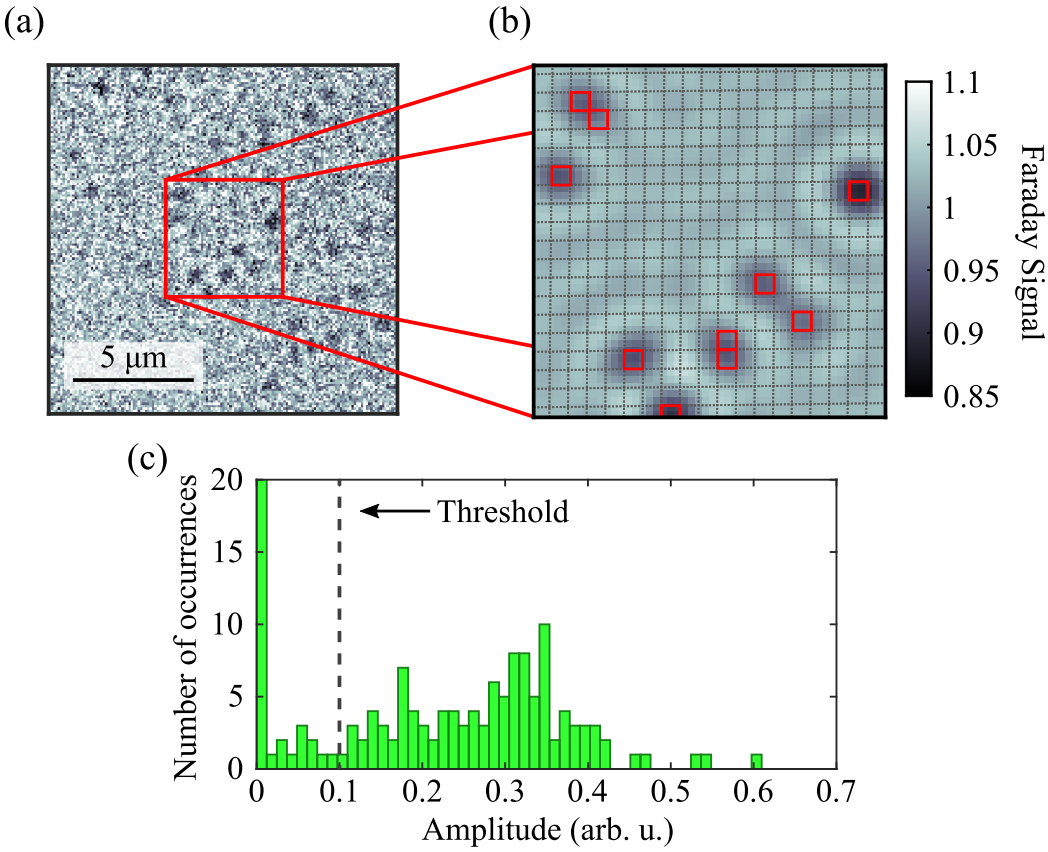

Figure 5.6: Deconvolution result of Faraday QGM. (a) Raw Faraday image of sparsely filled atoms in a 2D optical lattice. Note that the detuning of probe light is $2\pi \times 56\,\mathrm{MHz}$ with the saturation parameter $s_{399} = 0.84 \times 10^{-3}$. (b) Numerically reconstructed atom distribution on lattice sites. The image is convoluted with the model PSF of equation (5.4) and reconstructed atom distribution. Red squares and grey dotted lines represents the atoms and the lattice separations, respectively. (c) Histogram of the fitted amplitudes of the scattered field $\boldsymbol{E}_{\mathrm{sc}}(r)$ in each site. A black dashed line shows the threshold of the presence or absence of atoms.

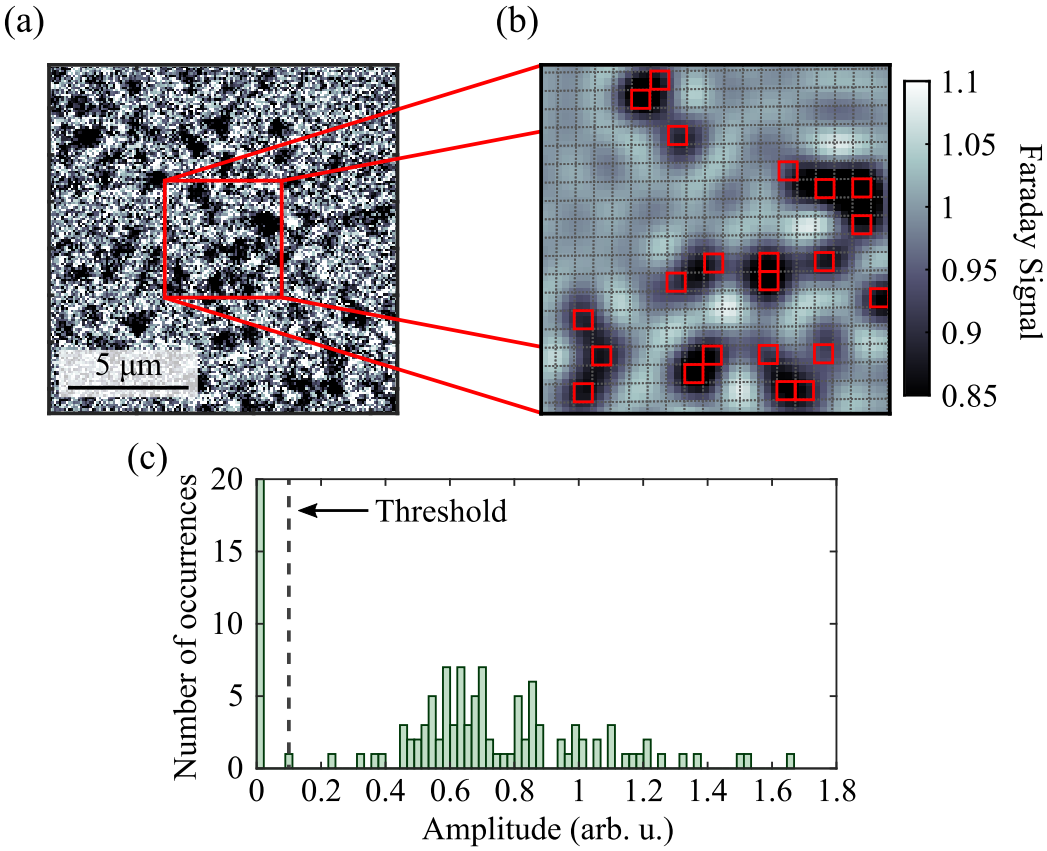

Figure 5.7: Deconvolution result of Faraday QGM with the near resonance light. (a) Raw Faraday image of sparsely filled atoms in a 2D optical lattice. Note that, differently from the data in figure 5.4(a), this image is taken with the detuning of $2\pi \times 10\,\mathrm{MHz}$ with respect to the ${}^1S_0$-${}^3P_1(m_J = -1)$ resonance under the magnetic field of 40 G. (b) Numerically reconstructed atom distribution on lattice sites. The image is convoluted with the model PSF of equation (5.4) and reconstructed atom distribution. Red squares and grey dotted lines represents the atoms and the lattice separations, respectively. (c) Histogram of the fitted amplitudes of the scattered field $\boldsymbol{E}_{\mathrm{sc}}(r)$ in each site. A black dashed line shows the threshold of the presence or absence of atoms.

5.3 Dark field Faraday imaging

In this section, I describe a dark field Faraday imaging (DFFI) with the PBS angle $\theta = \pi/2$. In this case, all of the probe light is reflected by the PBS and only the scattered light can be transmitted through and detected at a detector. Thus, this configuration of DFFI [148] enables us to obtain a back-ground-free signal like a fluorescence imaging.

5.3.1 Optical spectrum

We apply a magnetic field of 40 G and measure an optical spectrum of DFFI. The signal of DFFI can be described by

$$A_{\mathrm{DFFI}}(\delta_0) \propto |\boldsymbol{E}_{\mathrm{sc}}(\delta_0) \cdot \hat{e}_\theta|^2 \propto \left| \frac{1}{1 + i2(\delta_0 - \delta_B)/\Gamma} - \frac{1}{1 + i2(\delta_0 + \delta_B)/\Gamma} \right|^2 . \quad (5.8)$$

A green solid and a blue dashed lines in figure 5.8 show fits with equation (5.8) and a Lorentzian function, respectively. The green solid line is in better agreement with the experimental data than the blue dashed line.

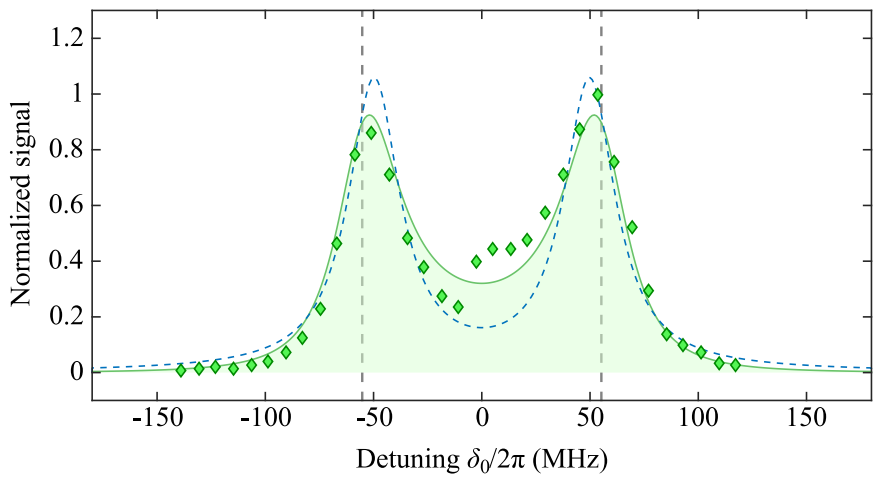

Figure 5.8: Spectrum of DFFI ($\theta = \pi/2$). A magnetic field of a 40 G is applied for DFFI. A green solid and a blue dashed lines show fits with Eq. (5.8) and a Lorentzian function, respectively. The signal strength in each spectrum is derived by the analysis of the ensemble average. The resonance positions are indicated by grey dashed lines.

5.3.2 Site-resolved imaging

For easier evaluation, only several percent of the atoms are selected and cooling beams are applied to suppress the heating effect and to keep atoms within the respective lattice sites. Figure 5.9(a) shows the DFFI signal of site-resolved image of single atoms. Here the detuning is $2\pi \times 56$ MHz, which is the same as figure 5.4(a) of the Faraday imaging. Although this DFFI signal looks quite similar to that of fluorescence imaging, the DFFI signal originates from a dispersive interaction just like a Faraday signal. Figure 5.9(b) shows the measured PSF, obtained by averaging about 30 individual atoms. We find that the measured PSF is well fitted with the theoretical formula given as

$$I_{\mathrm{DFFI}}(r) \propto \left(\frac{2\delta_B/\Gamma}{1+(2\delta_B/\Gamma)^2} \frac{2J_1(k\mathrm{NA}r)}{k\mathrm{NA}r} \right)^2, \tag{5.9}$$

and a green solid line in figure 5.9(b) shows a fit with equation (5.9). Note that we set the detuning $\delta_0 = 0$.

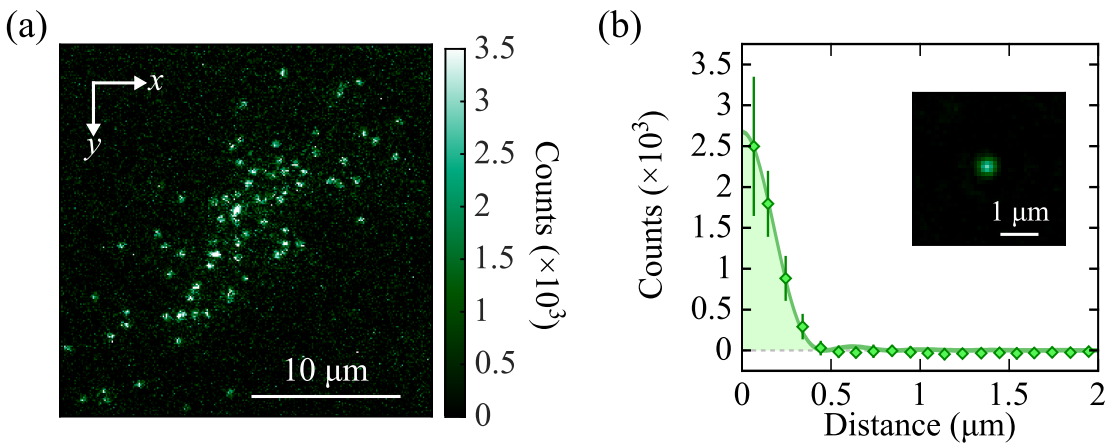

Figure 5.9: Site-resolved DFFI ($\theta = \pi/2$). (a) One illustrative example of DFFI. The detuning of the probe beam is $2\pi \times 56$ MHz with the saturation parameter $s_{399} = 1.1 \times 10^{-3}$. (b) Measured PSF averaged about 30 individual single atoms and azimuthal average of PSF. The green solid line shows a fit with equation (5.9) with NA = 0.52(1). This measurement takes the duration of 400 ms.

5.3.3 Detection fidelity

We measure the detection fidelity of Faraday QGM in the same way of fluorescence imaging. Here the images of DFFI are used for measurement of the detection fidelity because DFFI gives us a back-ground-free image which has a high signal-to-noise ratio. We show the intensity dependence of the detection fidelity in figure 5.10 and

the detuning dependence of cooling lights is shown in figure 5.11. In every measurement, we can reach the detection fidelity of $\sim 80\%$ with the proper parameters and the detection fidelity of 84(17)% is obtained with the optimal intensities and detunings of the probe and cooling beams. This detection fidelity is almost the same quality of that of fluorescence imaging.

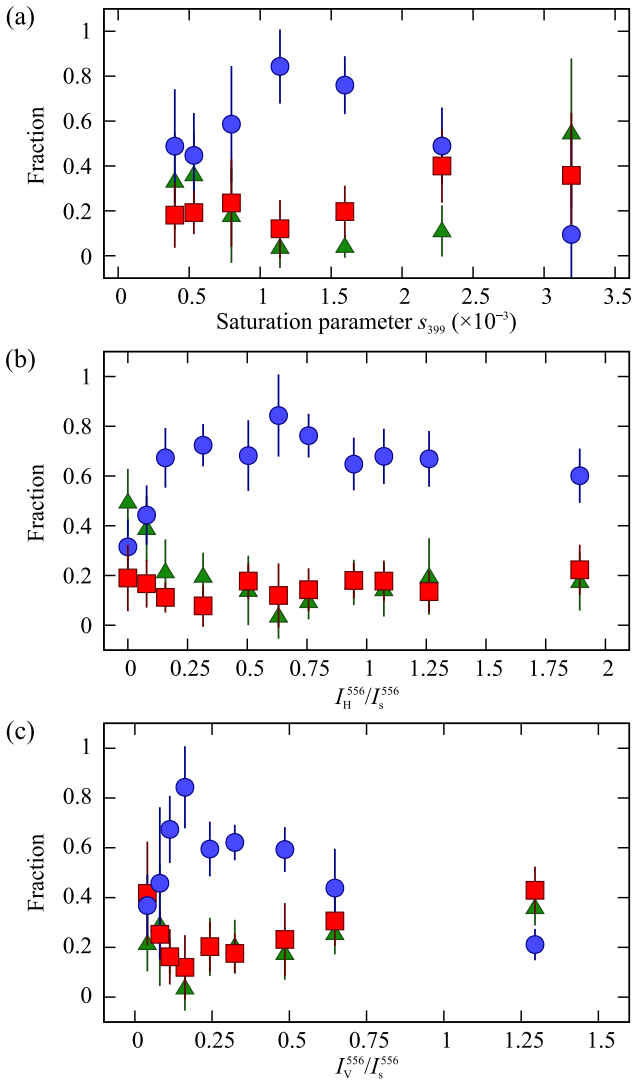

Figure 5.10: Intensity dependence of the detection fidelity of Faraday imaging. (a) Intensity dependence of the probe light. (b) Intensity dependence of the cooling light along horizontal axis with the saturation parameter of the probe beam $s_{399} = 1.1 \times 10^{-3}$. (c) Intensity dependence of the cooling light along vertical axis with the saturation parameter of the probe beam $s_{399} = 1.1 \times 10^{-3}$. Blue circles, red squares, and green triangles in figure indicate the fraction of pinned, lost, and hopping atoms. Note that the detuning of the probe beam is $2\pi \times 56$ MHz in all measurements.

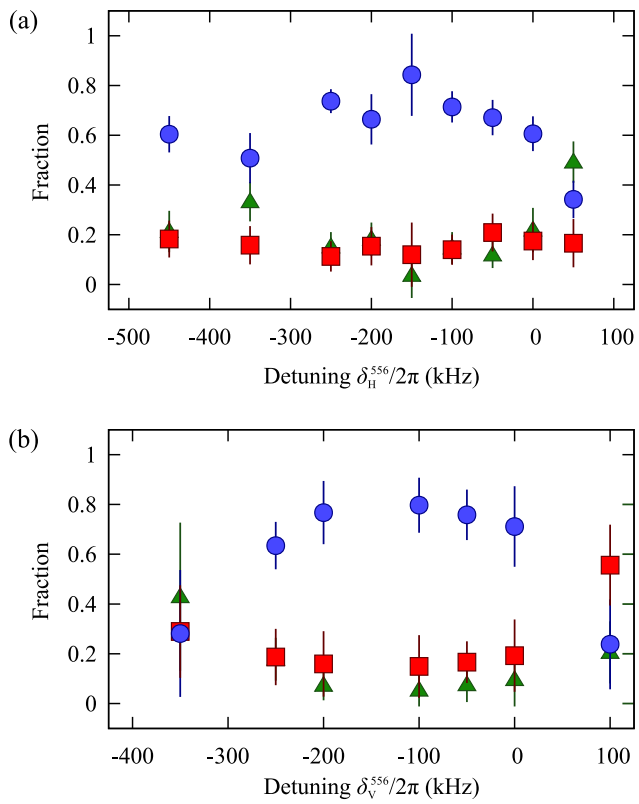

Figure 5.11: Cooling laser detuning dependence of the detection fidelity of Faraday imaging. (a) Detuning dependence of the cooling light along horizontal axis. (b) Detuning dependence of the cooling light along vertical axis. Blue circles, red squares, and green triangles in figure indicate the fraction of pinned, lost, and hopping atoms. Note that the detuning of the probe beam is $2\pi \times 56$ MHz with the saturation parameter $s_{399} = 1.1 \times 10^{-3}$ in all measurements.

5.4 Absorption imaging

In this section, I describe a absorption imaging with the PBS angle $\theta = 0$. This configuration is the standard set up for an ensemble measurement.

5.4.1 Optical spectrum

We measure an optical spectrum of absorption imaging with a magnetic field of 8 G. The absorption imaging shows a resonant character, which can be fitted with $-\log[A_{\mathrm{FI}}(\delta_0)]$ with the PBS angle $\theta = 0$ shown in figure 5.12.

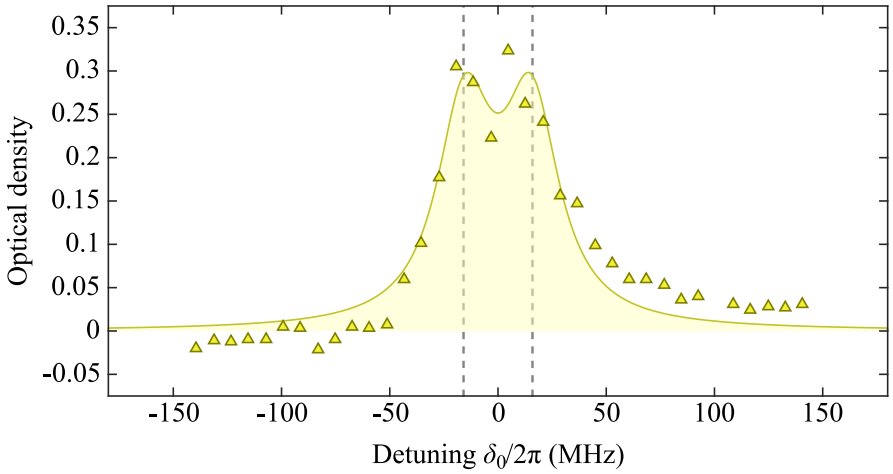

Figure 5.12: Spectrum of absorption imaging ($\theta = 0$). A magnetic field of a 8 G is applied for absorption imaging. The signal strength in each spectrum is derived by the analysis of the ensemble average. The resonance positions are indicated by grey dashed lines.

5.4.2 Site-resolved imaging

For easier evaluation of the performance of the site-resolved absorption imaging, we intentionally select only several percent of the atoms and prepare a sparse atom cloud for the measurement. Here the detuning is taken as $2\pi \times 11$ MHz within the linewidth of the probe transition. In this case, similarly to the Faraday imaging, a probe light makes destructive (and also constructive) interference with scattered light. In figure 5.13(a), we show one illustrative example of the absorption imaging, which clearly shows a site-resolved image of single atoms. Figure 5.13(b) shows the measured PSF, obtained by averaging about 60 individual atoms, which reveals the interference feature like the Faraday imaging. Again we find that our measured PSF

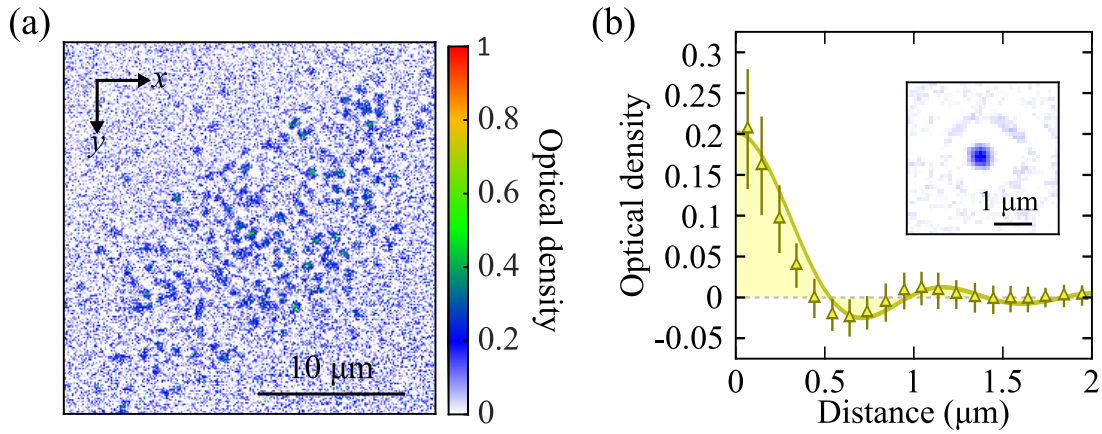

Figure 5.13: Site-resolved absorption imaging ($\theta = 0$). (a) One illustrative example of the absorption imaging. The detuning of the probe beam is $\delta_B = 2\pi \times 11\,\mathrm{MHz}$ with the saturation parameter $s_{399} = 2.9 \times 10^{-3}$. (b) Measured PSF averaged about 60 individual single atoms and azimuthal average of absorption image. The yellow solid line shows a fit with equation (5.10) with NA = 0.46(2). This measurement takes the duration of 400 ms.

is well fitted with the theoretical formula given by

$$I_{\mathrm{AI}}(r) = -\log\left[\left|1 - \sqrt{\frac{3\eta}{2}}\mathrm{NA}\frac{1}{1+(2\delta_B/\Gamma)^2}\frac{2J_1(k\mathrm{NA}r)}{k\mathrm{NA}r}\right|^2\right] \tag{5.10}$$

and a yellow solid line in figure 5.13(b) shows a fit with equation (5.10). A peak optical density of the PSF reaches 0.20(2) corresponding to the absorption rate 18(1)%. This value is much larger than that of the previous work of single atoms and ions [149, 150].

5.5 Non-destructive nature of Faraday imaging

The inherent non-destructive nature of the Faraday imaging method originates from the dispersive character of a Faraday effect, represented by the detuning dependence of the signal expressed by equation (5.4). The Faraday signal, which is the interference term of equation (5.4), is inversely proportional to the detuning ($\propto 1/\delta$) at a large detuning limit. This should be compared with the destructive effect of photon scattering rate Γ_{sc} by probe light, which is expressed by equation (5.5) and proportional to $1/\delta^2$ at a large detuning limit. Therefore, by taking a large detuning, we can improve the ratio of the signal strength to the destructive effect of the photon scattering in Faraday imaging. In figure 5.14, we plot the detuning dependence of the ratio of the Faraday imaging signal strength S to the photon scattering rate

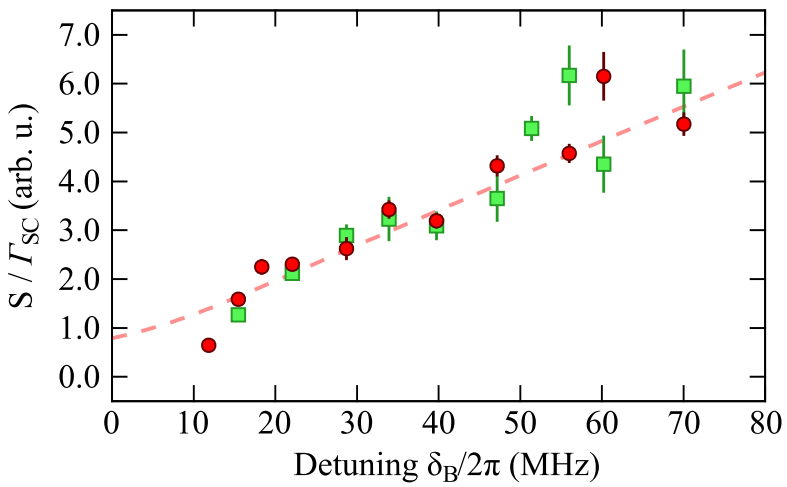

Figure 5.14: Ratio of signal strength S to photon scattering rate Γ_{sc} for Faraday imaging. The green squares represent the data obtained from the signals of isolated atoms, and red circles represent the ensemble measurements. A red dashed line shows a theoretically fitted curve.

Γ_{sc} in arbitrary units. Note that we represent the Faraday imaging signal strength S by the averaged signal of the isolated atoms in the Faraday imaging. On the other hand, the averaged signal of the isolated atoms in fluorescence imaging taken in the same condition is used as a measure of the photon scattering rate Γ_{sc}. The ratios obtained in this way are denoted by green squares. We also plot the ratios obtained by ensemble measurements as red circles. The experimental results are in good agreement with the theoretical prediction represented by a red dashed line and in particular show the linear increase with the detuning, indicating that the Faraday imaging realizes a single-atom observation with a reduced effect of photon scattering. In fact, the saturation parameter at the detuning of $\delta_B = 2\pi \times 70\,\mathrm{MHz}$ corresponding to 0.6×10^{-3}, almost half of the value of the typical fluorescence imaging. This is to be contrasted with the case of the fluorescence imaging where the ratio is constant on the detuning, and is not improved.

On the other hand, the signal of DFFI has a detuning dependence of $\propto 1/\delta_B^2$ at a large detuning limit, and has no non-destructive nature. The experimental results in figure 5.15 show the saturation of the ratio of the signal strength of DFFI S to the photon scattering rate Γ_{sc} at larger detunings, consistent with the theoretical prediction. This indicates that the DFFI has no merit to realize a single-atom observation with a reduced effect of photon scattering.

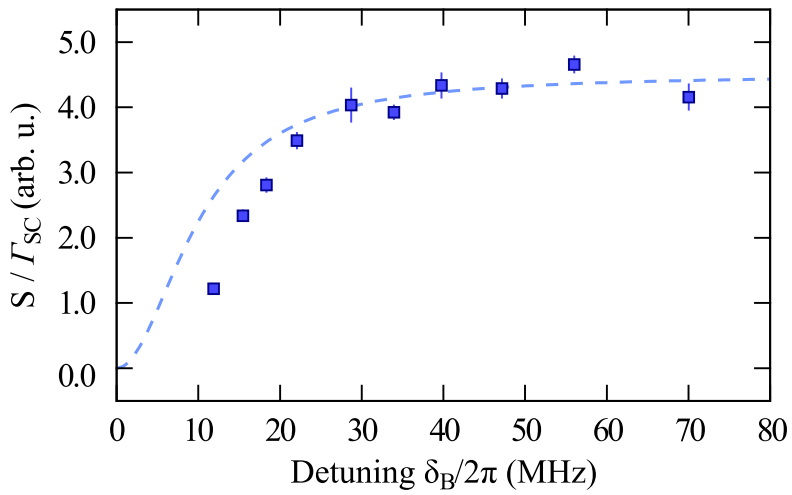

Figure 5.15: Ratio of signal strength S to photon scattering rate Γ_{sc} for DFFI. The blue squares represent the ensemble measurements. A blue dashed line shows a theoretically fitted curve.

5.6 Effect of the probe light for Faraday quantum gas microscope

Usually the fidelity of the imaging can be evaluated by taking two successive images of the same atoms and comparing the atom distributions. The fidelity deduced from such a method includes the fidelity of the deconvolution procedure, which will make a large contribution in the current Faraday imaging, especially at low probe intensities. Here, in order to purely extract the effect of the probe light for Faraday imaging, we apply a probe pulse with the same detuning as the Faraday imaging and with varying intensities during the 400 ms interval between the two images. The timing of taking two consecutive images and applying the probe beam is schematically shown in figure 5.16(a). The consecutive two images to determine the atom distributions are taken by setting the PBS angle to $\pi/2$ (DFFI) so that we can get the background-free image similar to the fluorescence images. Note that the cooling light is also applied to suppress the residual heating effect as in the Faraday imaging. In figure 5.16(b), we show the fidelity normalized by that without the probe light during two images. We find almost no change of pinned, loss, and hopping fractions when the probe intensity is below 2×10^{-2} times the saturation intensity. Above this intensity, we find almost linear increase of the loss and hopping fractions. This behavior is reasonable when considered in terms of the saturation parameter. The observed critical intensity corresponds to the saturation parameter of $s_{399} \sim 10^{-3}$ which is consistent with that observed in the previous experiment,

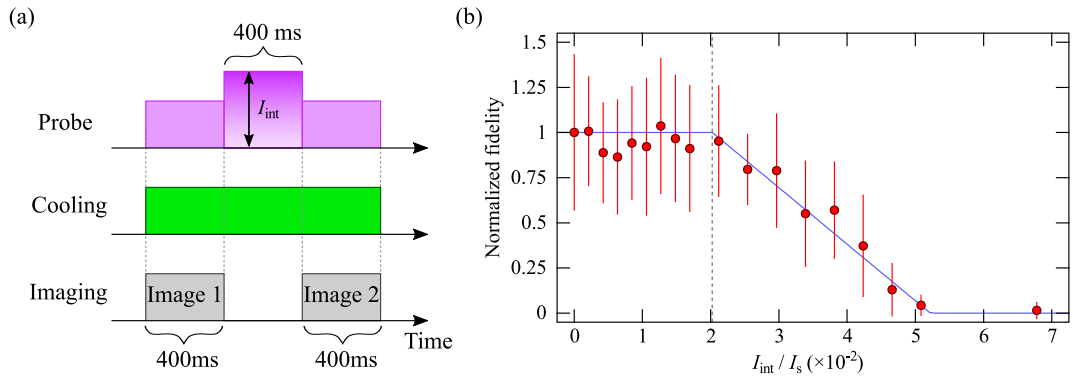

Figure 5.16: Effect of the probe light for Faraday QGM. (a) Timing of taking two consecutive images and varying the probe intensity. The duration of the exposure and the interval time is 400 ms. (b) Measured fidelity normalized by the fidelity without probe light is plotted for various probe intensities I_{int}. Below the intensity $I_{\text{int}} = 2 \times 10^{-2} \times I_s$, the normalized fidelity takes almost the same one. Note that I_s represents the saturation intensity of the probe beam.

where the cooling is balanced with the heating effect of the probe beam.

5.7 Current limitation of Faraday quantum gas microscope

In this section, I discuss the current limitation of the Faraday imaging method and its possible solutions. The Faraday signal is obtained as a result of the interference between the scattered and the probe light beams. The background level of the Faraday signal is, thus, sensitive to the temporal fluctuation and the spatial inhomogeneity of the intensity and the polarization of the probe beam, resulting in a relatively poor signal-to-noise ratio. This problem can in principle be solved by careful stabilization of the probe beam for its intensity, polarization, and spatial profile. In the present experiment, to achieve a better signal-to-noise ratio with only intensity stabilization, the probe beam has a strong intensity which causes the residual heating effect so that cooling during the imaging is required. An interferometric detection of a weak light using a strong local oscillator for a homodyne detection scheme, similar to ref. [129], would enhance the detection sensitivity with a reduced photon scattering rate. The polarization-squeezed light is also useful for the suppression of the polarization noise below the standard quantum limit [151, 152]. The realization of non-destructive limit of the Faraday QGM would significantly relax the experimental hurdle for a QGM setup, such as the necessity of an elaborate cooling scheme in an extremely high optical lattice depth during the imaging. This will

even open the possibilities of various atomic species and even molecules for quantum gas microscopy as well as the occupancy-resolved measurement beyond the current parity measurement.

5.8 Conclusion

In conclusion, we successfully demonstrate site-resolved imaging of single atoms with the Faraday effect. The observed Faraday rotation angle reaches 3.0(2) degrees for a single atom. We demonstrate the non-destructive feature of this Faraday imaging method by investigating the detuning dependence of the signal. In addition, we demonstrate absorption imaging and DFFI of QGM, and reveal the different shapes of PSFs for these imaging methods, which are fully explained by theoretical analysis. Our result is an important step towards an ultimate QND measurement with a single-site resolution. It will furthermore open up the possibilities for quantum feedback control of individual atoms in a quantum many-body system which will have significant impacts on quantum information processing and the physics of quantum many-body system.

Chapter 6

Conclusion and outlook

6.1 Conclusion

This thesis presents the realization of a QGM of Yb atoms with both a fluorescence and a Faraday imaging methods.

- *Fluorescence imaging* (Chapter 4)

  We precisely determine the scalar and tensor polarizabilities of the $^3P_1$ state and successfully reduce the inhomogeneity of light shift between the $^1S_0$ and $^3P_1$ states, resulting in efficiently cooling atoms in a 2D optical lattice with Doppler and sideband cooling and suppressing the heating by probe light with the $^1S_0$-$^1P_1$ transition. The measured lifetime of imaging reaches over 7 s and the resulting temperature is $T = 7.4(13)\,\mu$K, corresponding to a mean oscillation quantum number along horizontal axis of 0.22(4) during the imaging process. In addition, we precisely tune the tilt of objective and successfully realize the high-resolution imaging system where the resolution of imaging system is a FWHM of 364 nm. We detect on average 200 fluorescence photons from a single atom within 400 ms exposure time. Thanks to these results, we successfully demonstrate a site-resolved imaging of individual ^{174}Yb atoms in a 2D optical lattice with fluorescence imaging. Furthermore, taking two successive site-resolved images enables us to estimate the detection fidelity and we achieve the high detection fidelity of 87(2)% with the optimal intensity and detuning of the probe and cooling beams.

- *Faraday imaging* (Chapter 5)

  We successfully demonstrate a site-resolved imaging with the Faraday effect and the observed Faraday rotation angle reaches 3.0(2) degrees for a single atom. Differently from a fluorescence imaging, a site-resolved imaging using

the Faraday effect enables us to suppress the heating by the probe light at a large detuning of probe light. In fact, we observe the linearly increasing feature of the ratio of Faraday signal strength S to photon scattering rate Γ_{sc} at a large detuning. In addition, we perform the different type of site-resolved imaging such as DFFI and absorption imaging and we reveal the different feature of the spatial distribution of single atoms in these imaging methods, which are fully explained by theoretical analysis. In absorption imaging, the peak optical density of the PSF reaches 0.20(2) and this value is much larger than that of previous works for single atoms and ions. We also estimate the detection fidelity of 84(17)% using DFFI which enables us to obtain a background-free signal like a fluorescence imaging. This detection fidelity is almost the same quality of that of fluorescence imaging.

6.2 Outlook

The fluorescence imaging with single-site resolution developed in this thesis is applicable for a QGM of other Yb isotopes including fermionic ^{171}Yb and ^{173}Yb atoms. The QGM of fermionic ^{171}Yb and ^{173}Yb atoms provides us to a platform for studying many fascinating physics such as SU($\mathcal{N}$) physics with single-site resolution. In addition, our imaging method where we simultaneously cool atoms with sideband cooling is straightforwardly applied to other alkaline-earth atom species (e.g. strontium atoms). The realization of a QGM with enough fidelity for Yb atoms in a Hubbard-regime optical lattice opens up the possibilities for studying various kinds of quantum many-body systems such as Bose and Fermi gases, and their mixtures, and also long-range-interacting systems such as Rydberg states.

We successfully demonstrate the site-resolved imaging with the dispersive Faraday effect. In our present setup, however, we need the strong probe beam for site-resolved imaging to compensate for a large noise due to the temporal fluctuation and the spatial inhomogeneity of the intensity and the polarization of the probe beam. Thus, we need to simultaneously cool atoms during Faraday imaging. The interferometric detection of a weak light with a strong oscillator for a homodyne detection and the polarization-squeezed light are quite useful for suppression of the instability of the probe beam. This suppression will enable us to reduce the unfavorable heating, that is, the destructive effect by probe light, resulting in relaxing the experimental hurdle for QGM setup and enabling us to perform the nondestructive Faraday QGM of various atomic species and even molecules as well as occupancy-resolved measurement in each site beyond the current parity measurement. Furthermore, the realization of the nondestructive Faraday QGM will open up

the possibilities for an ultimate quantum control and feedback of individual atoms in a quantum many-body system which will have great impacts on not only the physics of quantum many-body system but also quantum information processing.

Journal articles

List of journal articles to which I contributed during graduate work.

- *"Site-resolved imaging of single atoms with a Faraday quantum gas microscope"*
  R. Yamamoto, J. Kobayashi, K. Kato, T. Kuno, Y. Sakura, and Y. Takahashi
  arXiv:1607.07045 (2016)

- *"Laser spectroscopic probing of coexisting superfluid and insulating states of an atomic Bose-Hubbard system"*
  S. Kato, K. Inaba, S. Sugawa, K. Shibata, R. Yamamoto, M. Yamashita, and Y. Takahashi
  Nat. Commun. **7**, 11341 (2016)

- *"An ytterbium quantum gas microscope with narrow-line laser cooling"*
  R. Yamamoto, J. Kobayashi, T. Kuno, K. Kato, and Y. Takahashi
  New J. Phys. **18**, 023016 (2016)

- *"Optical spectral imaging of a single layer of a quantum gas with an ultranarrow optical transition"*
  K. Shibata, R. Yamamoto, Y. Seki, and Y. Takahashi
  Phys. Rev. A **89**, 031601(R) (2014)

- *"High-Sensitivity In situ Fluorescence Imaging of Ytterbium Atoms in a Two-Dimensional Optical Lattice with Dual Optical Molasses"*
  K. Shibata, R. Yamamoto, and Y. Takahashi
  J. Phys. Soc. Jpn. **83**, 014301 (2013)

- *"Control of Resonant Interaction between Electronic Ground and Excited States"*
  S. Kato, S. Sugawa, K. Shibata, R. Yamamoto, and Y. Takahashi
  Phys. Rev. Lett. **110**, 173201 (2013)

- *"Observation of long-lived van der Waals molecules in an optical lattice"*
  S. Kato, R. Yamazaki, K. Shibata, R. Yamamoto, H. Yamada, and Y. Takahashi
  Phys. Rev. A **86**, 043411 (2012)

- *"Optical magnetic resonance imaging with an ultra-narrow optical transition"*
  S. Kato, K. Shibata, R. Yamamoto, Y. Yoshikawa, and Y. Takahashi
  Appl. Phys. B **108**, 31-38 (2012)

Appendix A

Physical constants

This appendix summarize physical constants in table A.1.

Table A.1: Physical constants taken from ref. [153].

Physical constant	Symbol	Value	Unit
Speed of light in vacuum	c	$2.997\,924\,58 \times 10^{8}$	$\mathrm{m\,s^{-1}}$
Magnetic constant	μ_0	$4\pi \times 10^{-7}$	$\mathrm{N\,A^{-2}}$
Electric constant	ε_0	$8.854\,187\,817 \times 10^{-12}$	$\mathrm{F\,m^{-1}}$
Plank constant	h	$6.626\,069\,57 \times 10^{-34}$	$\mathrm{J\,s}$
Dirac constant	$\hbar$	$1.054\,571\,726 \times 10^{-34}$	$\mathrm{J\,s}$
Elementary charge	e	$1.602\,176\,565 \times 10^{-19}$	C
Electron mass	m_e	$9.109\,382\,91 \times 10^{-31}$	kg
Proton mass	m_p	$1.672\,621\,777 \times 10^{-27}$	kg
(Unified) atomic mass unit	m_u	$1.660\,538\,921 \times 10^{-27}$	kg
Boltzmann constant	k_B	$1.380\,648\,8 \times 10^{-23}$	$\mathrm{J\,K^{-1}}$
Acceleration of gravity	g_n	$9.806\,65$	$\mathrm{m\,s^{-2}}$
Bohr magneton	μ_B	$927.400\,968 \times 10^{-26}$	$\mathrm{J\,T^{-1}}$
Nuclear magneton	μ_N	$5.050\,783\,53 \times 10^{-27}$	$\mathrm{J\,T^{-1}}$
Bohr radius	a_0	$0.529\,177\,210\,92 \times 10^{-10}$	m
Electron g-factor	g_e	$-2.002\,319\,304\,361\,53$	

Appendix B

Towards a quantum gas microscope of fermionic ytterbium atoms

In this appendix, current status of a QGM of fermionic ^{171}Yb atoms with fluorescence imaging is described.

B.1 Atom preparation

The s-wave scattering length of fermionic ^{171}Yb atoms is $-0.15\,\mathrm{nm}$ and quite small for efficient evaporative cooling. For efficient evaporative cooling of ^{171}Yb atoms, we simultaneously load bosonic ^{174}Yb atoms and perform sympathetic evaporative cooling. Here the interspecies scattering length between ^{171}Yb and ^{174}Yb atoms is $22.7\,\mathrm{nm}$, which is large enough for sympathetic evaporative cooling. After sympathetic evaporative cooling, we can obtain $\sim 10^3$ ^{171}Yb atoms with $T/T_F \sim 1$ and we load the ^{171}Yb atoms into a 2D optical lattice by a similar way described in section 4.1.

B.2 Raman sideband cooling

The ^{171}Yb atoms has a nuclear spin $I = 1/2$ and thus we can apply sub-Doppler cooling techniques such as polarization-gradient cooling [81] and Raman sideband cooling [82–89]. Here we apply Raman sideband cooling technique for a QGM of fermionic ^{171}Yb atoms, schematically shown in figure B.1. Note that the trap frequency along vertical axis is quite small, $2\pi \times 15.7\,\mathrm{kHz}$, and cooling mechanism along vertical direction is Doppler cooling.

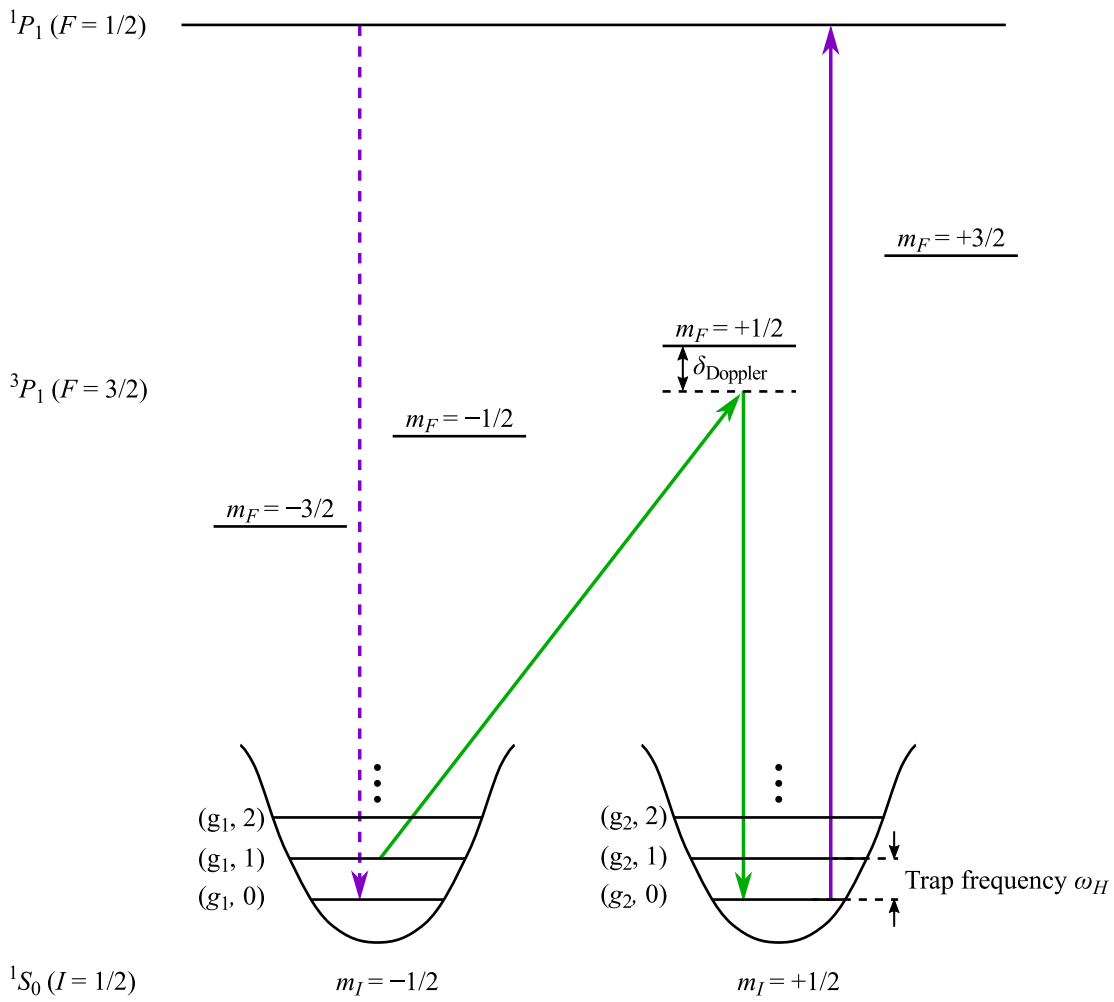

Figure B.1: Raman sideband cooling for fermionic ^{171}Yb atoms. A Raman transition drives atoms into the $^1S_0(I = 1/2, m_I = +1/2)$, removing one vibrational excitation. The probe light of the $^1S_0$-$^3P_1$ transition is used for the optical pumping. Note that δ_{Doppler} indicates the detuning of 556 nm cooling molasses along vertical axis.

B.3 Inhomogeneuity of light shifts between the $^1S_0$ and the $^3P_1$ states

For ^{171}Yb atoms, the light shift in the magnetic sublevel m_F of the $^3P_1$ state is given by [138]

$$\Delta E_e^L = -\frac{h}{4}\alpha_e(F, m_F, \theta)I, \tag{B.1}$$

where

$$\alpha_e(F, m_F, \theta) = \alpha_e^S - (1 - 3\cos^2\theta)\alpha_{nJF}^T \frac{3m_F^2 - F(F+1)}{2F(2F-1)}, \tag{B.2}$$

$$\alpha_{nJF}^T = (-1)^{F+1/2} \times 3\sqrt{5}\sqrt{\frac{2F(2F-1)(2F+1)}{3(F+1)(2F+3)}} \left\{ \begin{array}{ccc} F & 2 & F \\ 1 & 1/2 & 1 \end{array} \right\} \alpha_e^T. \tag{B.3}$$

Here $\alpha_e^S = 22.4(2)\,\mathrm{Hz/(W/cm^2)}$ and $\alpha_e^T = -7.6(1)\,\mathrm{Hz/(W/cm^2)}$ and the notation $\left\{ \begin{array}{ccc} j_1 & j_2 & j_3 \\ j_4 & j_5 & j_6 \end{array} \right\}$ is the Wigner 6-j symbol. Using above equations, the calculated polarizabilities with angles θ is shown in figure B.2. The ratio of $\alpha_e(F, m_F, \theta)/\alpha_g$ with any (F, m_F, θ) is less than 0.8.

B.4 Site-resolved imaging

After the preparation of dilute atoms in a 2D optical lattice, we perform a high-resolution imaging with a narrow-line laser cooling described above and we successfully detect single fermionic ^{171}Yb atoms with single site resolution. We show one illustrative example of fermionic QGM in figure B.3 and we can find many atoms are lost during two successive images. This indicates that the laser cooling during imaging process is not sufficient because of the large inhomogeneity of light shifts between the $^1S_0$ and the $^3P_1$ states described in above section. In fact, the lifetime of fermionic ^{171}Yb atoms during imaging process is 1.2(1) s and quite shorter than that of bosonic ^{174}Yb atoms (see figure B.4). For a QGM of fermionic ^{171}Yb atoms with high detection fidelity, this problem must be solved.

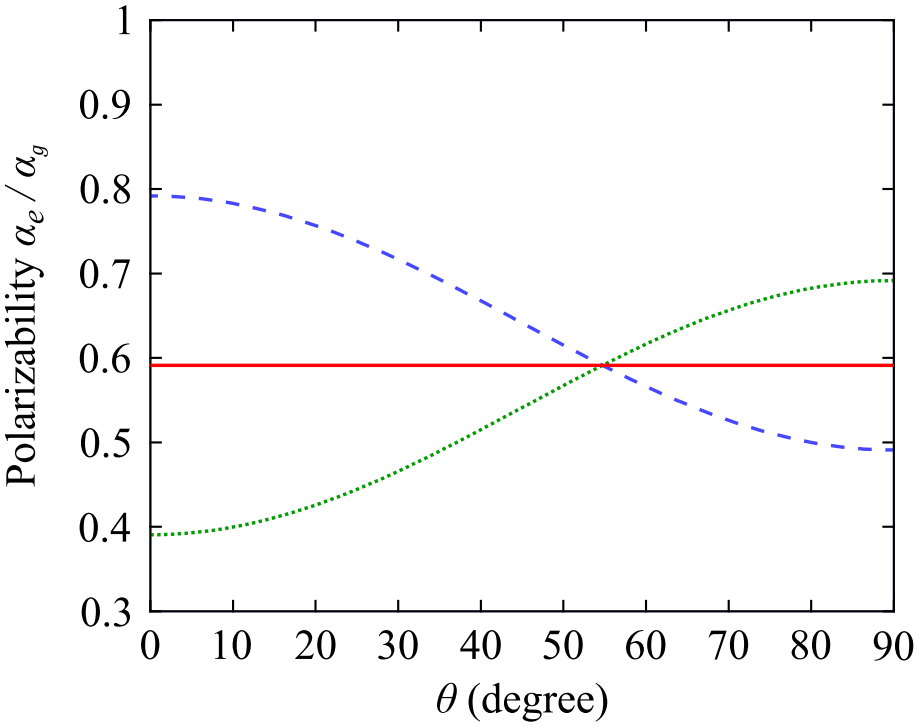

Figure B.2: Theoretically calculated polarizability of $^3P_1$ state for fermionic ^{171}Yb atoms. A red solid, a blue dashed, and a green dotted curves represent the calculated polarizability of $|F, m_F\rangle = |1/2, \pm 1/2\rangle$, $|3/2, \pm 1/2\rangle$, and $|3/2, \pm 3/2\rangle$, respectively. Here F is the quantum number for the total angular momentum $\boldsymbol{F}$ of ^{171}Yb atoms and m_F is its magnetic sublevel, respectively.

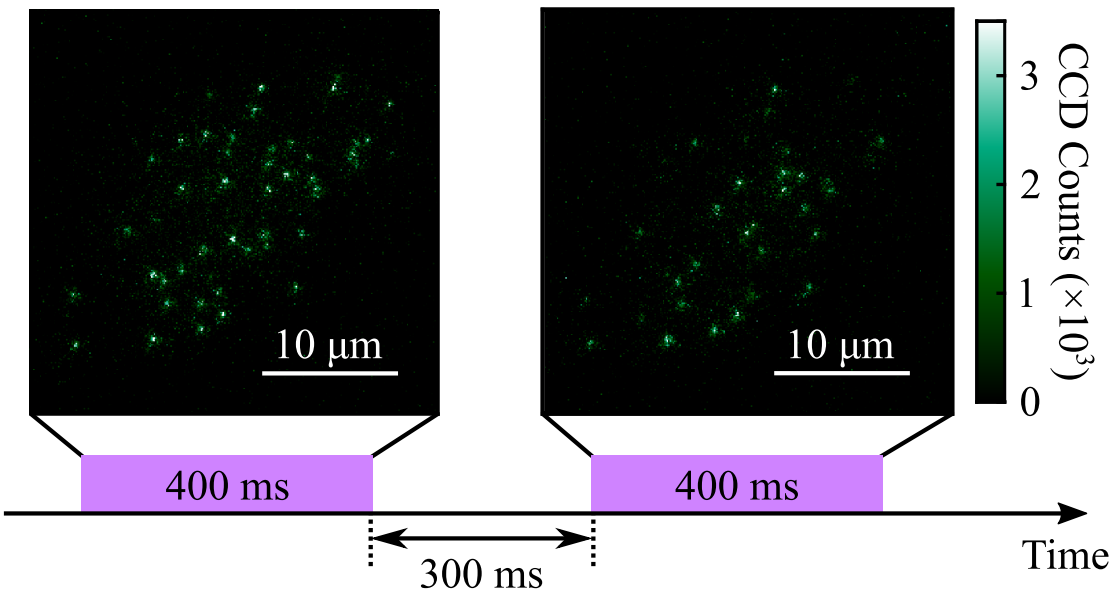

Figure B.3: Site-resolved image of fermionic ^{171}Yb atoms. Note that the exposure time and the interval time between two successive images are 400 ms and 300 ms, respectively.

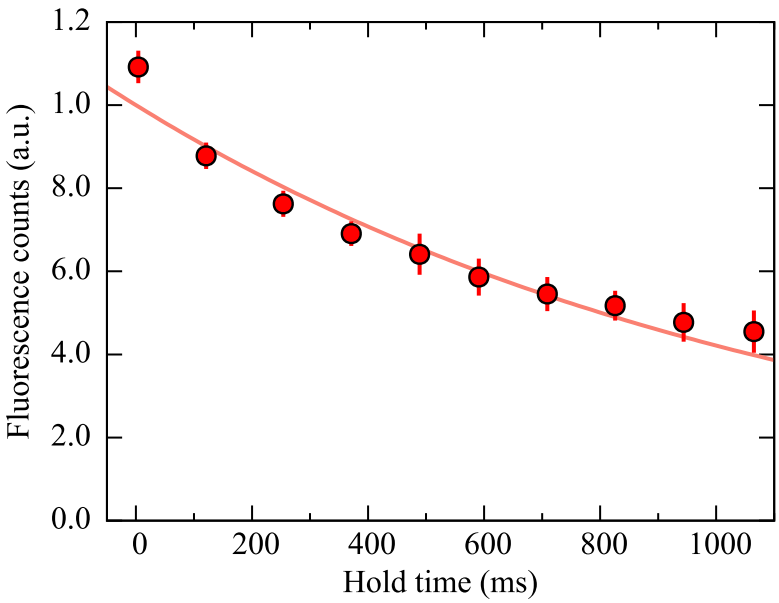

Figure B.4: Lifetime measurement of fermionic ^{171}Yb QGM. Red circles shows the measured data. A red solid line is a fit to the data and yields the lifetime of fluorescence imaging of ^{171}Yb atoms $\tau = 1.2(1)\,\mathrm{s}$.

Appendix C

Transmission rate of a glass cell

In this appendix, the transmission rate of a glass cell (Schott AG BOROFLOAT) for each wavelength is described. A thickness of a glass plate using in this measurement is 3 mm and this thickness is the same as that of a glass cell. The measurement is done by Solid state spectroscopy group in Kyoto university. The result is shown in figure C.1 and the transmission rates of the relevant optical transitions of Yb atoms are summarized in table C.1.

Table C.1: Transmission rate of a glass cell for typical optical transitions of Yb atoms.

Wavelength λ	Optical transition	Transmission rate (%)
399 nm	$(6s^2)^1S_0 \rightarrow (6s6p)^1P_1$	91.32
507 nm	$(6s^2)^1S_0 \rightarrow (6s6p)^3P_2$	91.83
556 nm	$(6s^2)^1S_0 \rightarrow (6s6p)^3P_1$	91.77
578 nm	$(6s^2)^1S_0 \rightarrow (6s6p)^3P_0$	91.74
649 nm	$(6s6p)^3P_0 \rightarrow (6s6p)^3S_1$	92.00
680 nm	$(6s6p)^3P_1 \rightarrow (6s6p)^3S_1$	91.99
770 nm	$(6s6p)^3P_2 \rightarrow (6s6p)^3S_1$	92.11
493 nm	$(6s6p)^3P_2 \rightarrow (6s6d)^3D_3$	91.79
532 nm	(for optical trap and lattice)	91.65

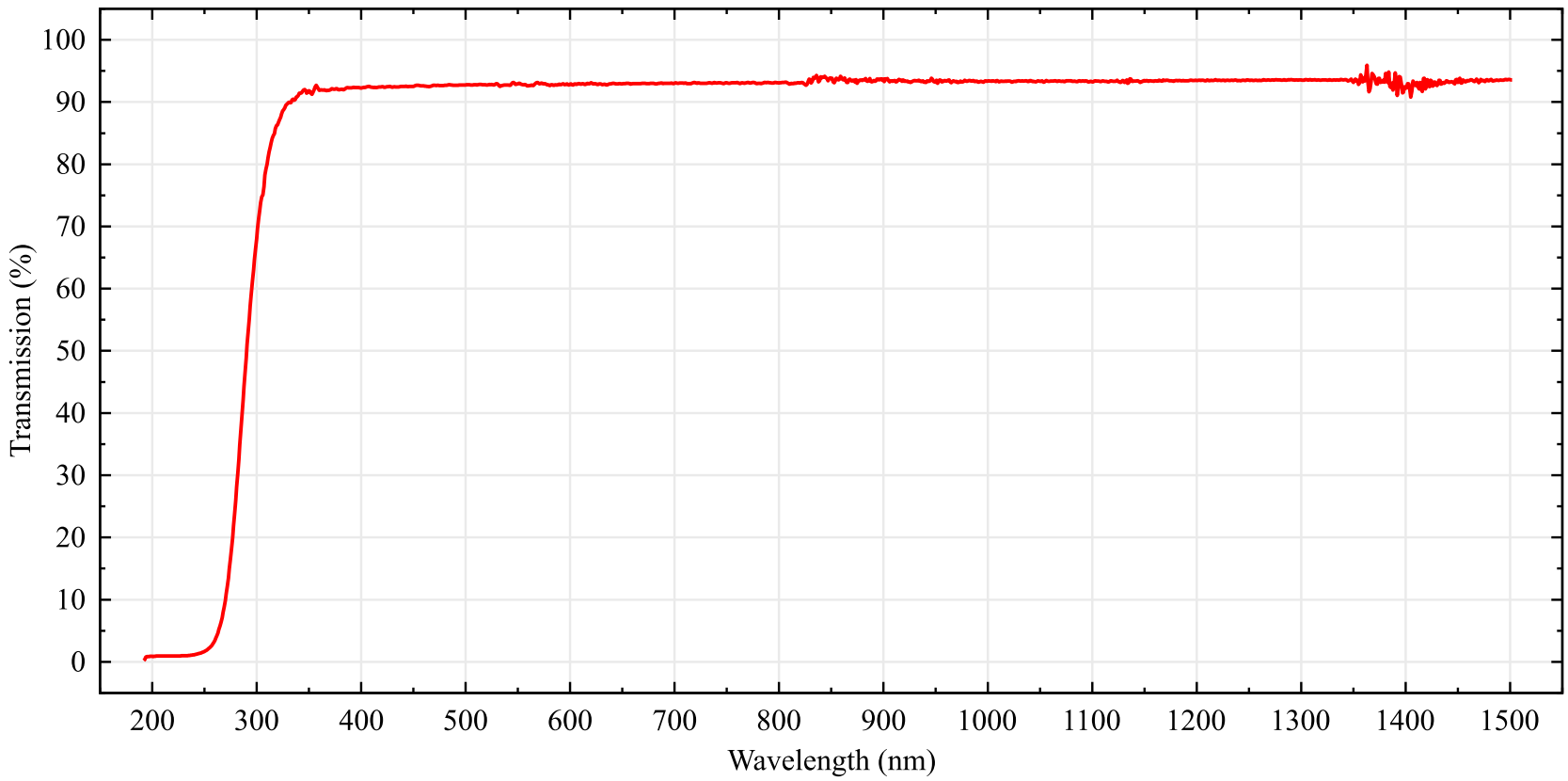

Figure C.1: Transmission rate of a glass cell (Schott AG BOROFLOAT).

Appendix D

Control system

In ultracold atom experiments, we need to control a lot of digital and analog devices with high accuracy. In addition to this requirement, we should prepare a control system where we can easily change parameters and sequences of experiments because we have to take data under various conditions. To meet these requests, we develop the control system for experiments using PXI system (PXIe-1073, National instruments Corporation) inserting two analog output board (PXI-6733, National instruments Corporation) and two DAQ board (PXIe-6363, National instruments Corporation). This PXI system provides us to 64 digital I/O and 24 analog output channels.

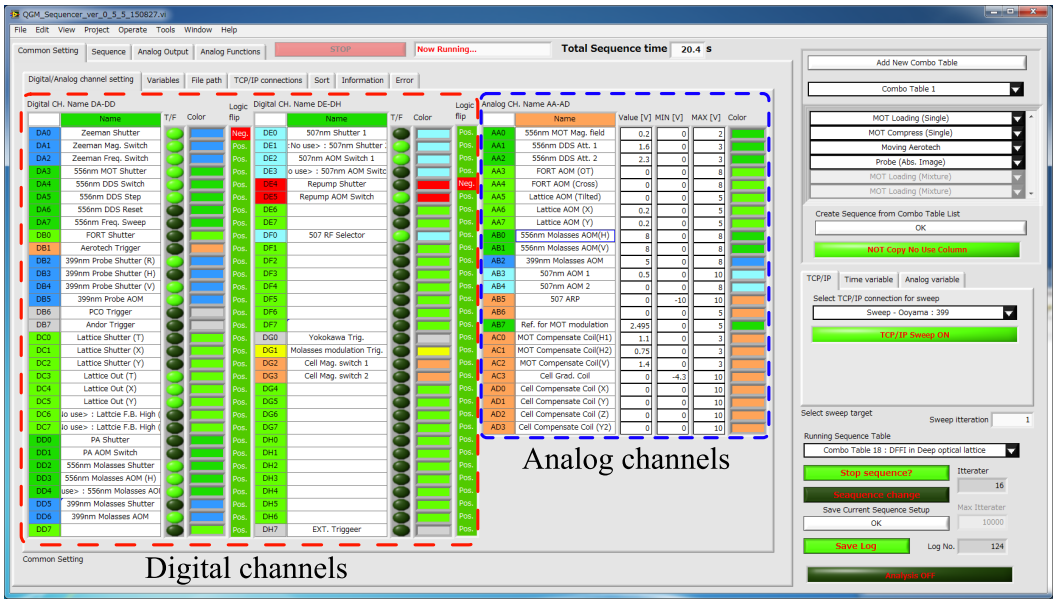

Figure D.1: Control panel for manually controlling digital and analog outputs. Left two columns surrounded by a red dotted line show the digital control part and a right column surrounded by a blue dotted line the analog control part. Note that analog output values are limited between the setting maximum and minimum values.

For controlling these devices, we also develop the control program written in LabVIEW (National instruments Corporation). Figure D.1 shows the panel for manually controlling digital and analog outputs. Here analog output values are limited between the setting maximum and minimum values. We can easily change frequently changing parameters including the duration times and the analog output values (e.g. the atom loading time and the potential depth of optical lattices), shown in figure D.2. Using these parameters or directly input control values, we can construct a timing table of experimental sequence, shown in figure D.3(a). In addition, various analog output groups (see figure D.3(b)) are available in each timing of an experimental sequence. Using a TCP/IP connection, we can sweep a frequency of laser beams, for example cooling beams, after each every sequence (see figure D.4(a)). We can also sweep a parameter of a time duration and an analog output value after every sequence (see figure D.4(b) and (c)).

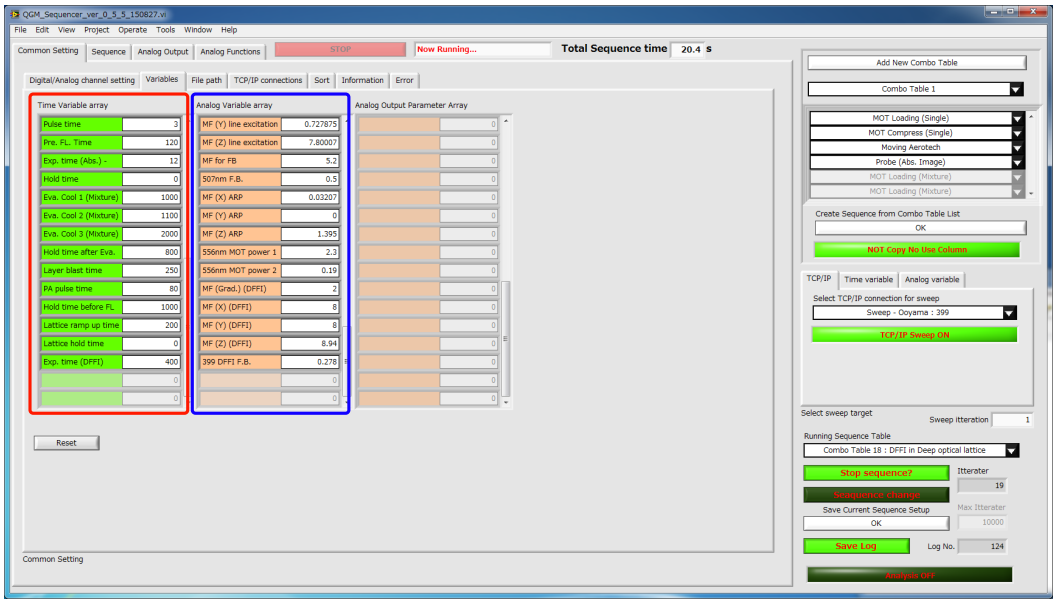

Figure D.2: Control panel for frequently changing parameters. We can change the duration time using the left column surrounded by a red line and the analog output values using the center column surrounded by a blue line.

(a)

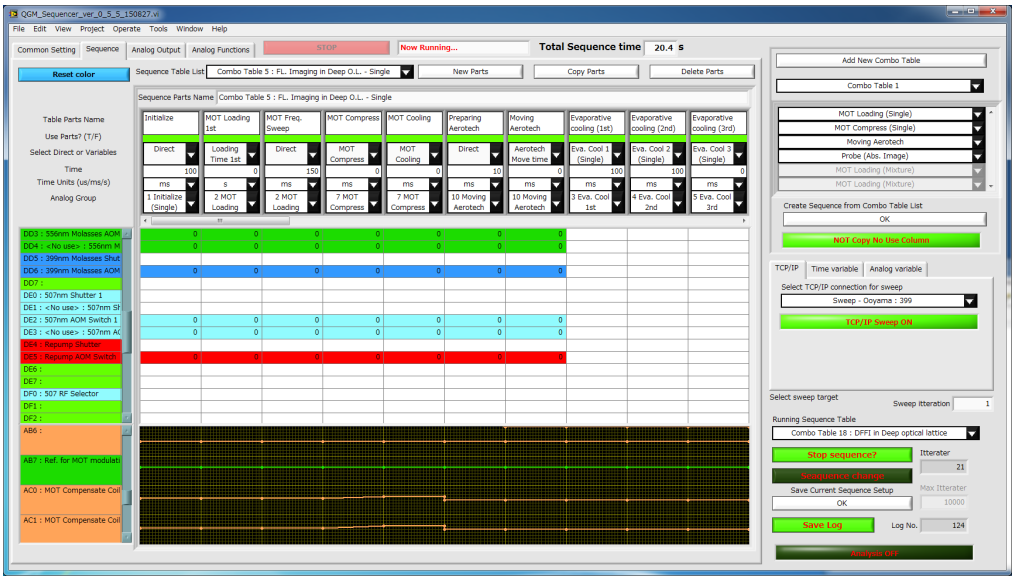

(b)

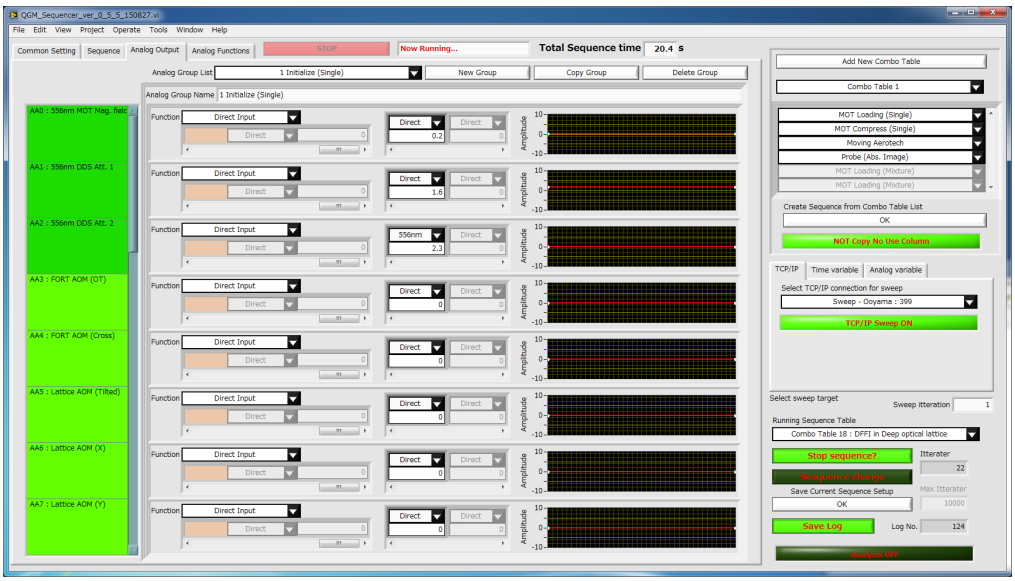

Figure D.3: Control panel for a timing table of an experimental sequence and analog outputs in each timing. (a) Control panel for a timing table of experimental sequence. (b) Control panel for analog outputs in each timing.

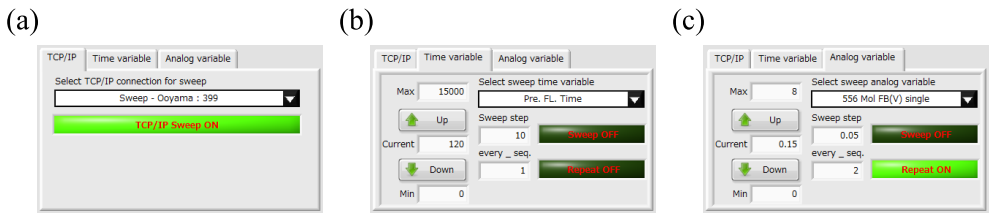

Figure D.4: Selection panel of a frequency sweep and a parameter sweep. (a) A frequency sweep panel thorough TCP/IP connection. (b) and (c) A parameter sweep panel for a duration time and an analog output value.

Appendix E

Schematics of the holding jig for the imaging system

In this appendix, I present a CAD data of the holding jig for a high-resolution objective with the adjustment system of the tilt of it. Here we use a manual swivel stage (ST07A-S1W, Kohzu Precision Co., Ltd.) for the tilting adjustment.

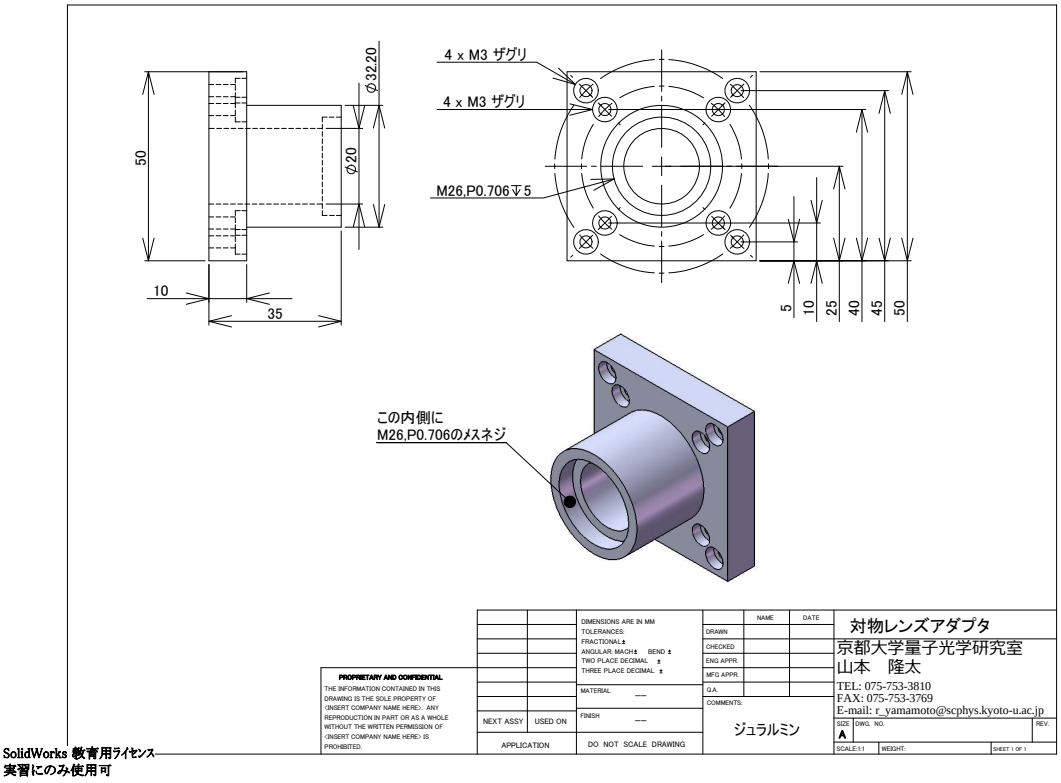

Figure E.1: Schematic of the adapter for objective.

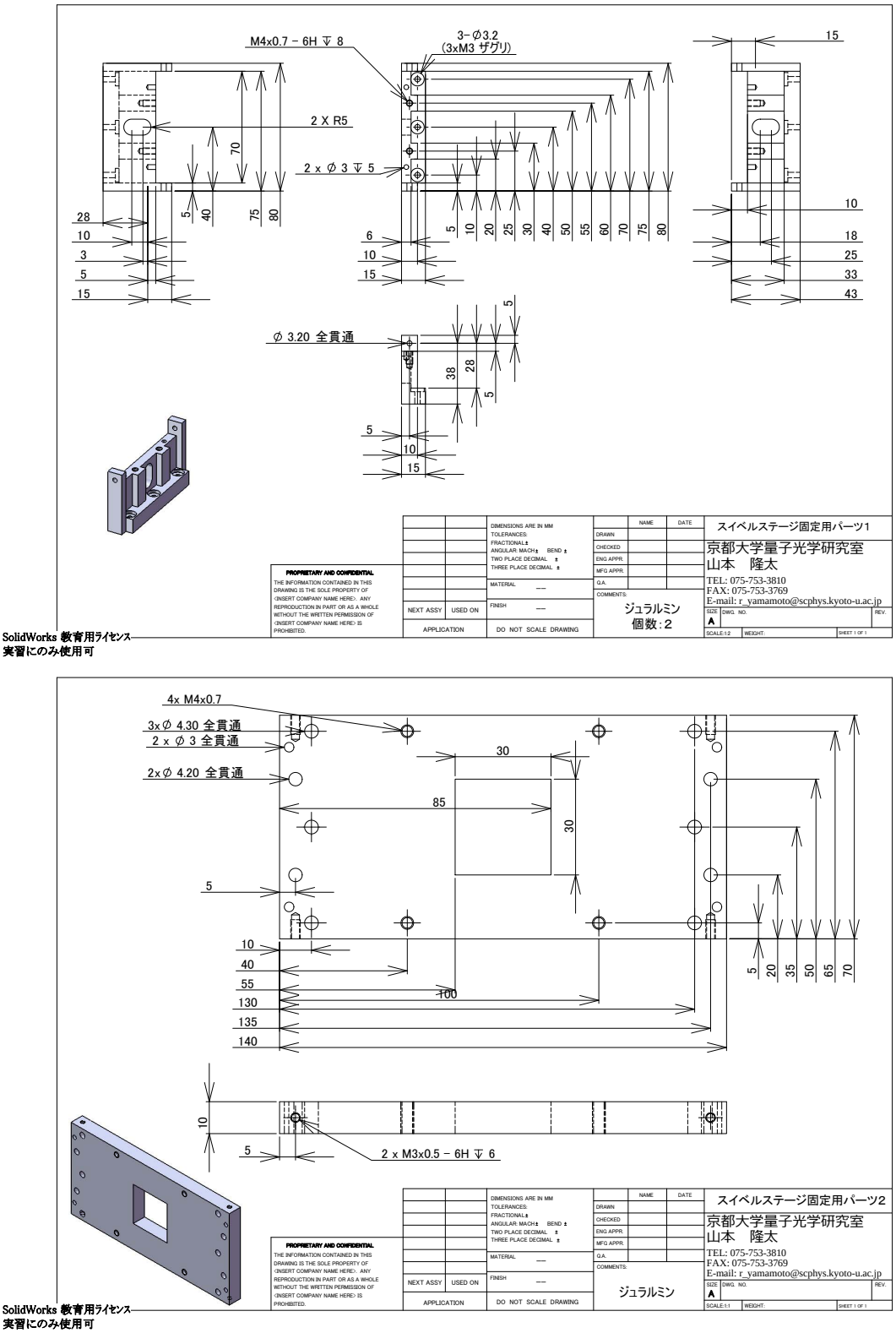

Figure E.2: Schematic of parts of the holding jig for the swivel stage.

Bibliography

[1] Martin Miranda, Ryotaro Inoue, Yuki Okuyama, Akimasa Nakamoto, and Mikio Kozuma, "*Site-resolved imaging of ytterbium atoms in a two-dimensional optical lattice*", Phys. Rev. A, **91**, 063414 (2015).

[2] D. J. Wineland and H. Dehmelt, "*Proposed* 10^{14} $\delta\upsilon/\upsilon$ *laser fluorescence spectroscopy on* $T1^{+}$ *mono-ion Oscillator iii*", Bulletin of the American Physical Society, **20**, 637 (1975).

[3] T. W. Hänsch and A. L. Schawlow, "*Cooling of gases by laser radiation*", Opt. Commun., **13**, 68–69 (1975).

[4] D. J. Wineland, R. E. Drullinger, and F. L. Walls, "*Radiation-Pressure Cooling of Bound Resonant Absorbers*", Phys. Rev. Lett., **40**, 1639–1642 (1978).

[5] W. Neuhauser, M. Hohenstatt, P. Toschek, and H. Dehmelt, "*Optical-Sideband Cooling of Visible Atom Cloud Confined in Parabolic Well*", Phys. Rev. Lett., **41**, 233–236 (1978).

[6] Steven Chu, L. Hollberg, J. E. Bjorkholm, Alex Cable, and A. Ashkin, "*Three-dimensional viscous confinement and cooling of atoms by resonance radiation pressure*", Phys. Rev. Lett., **55**, 48–51 (1985).

[7] M. H. Anderson, J. R. Ensher, M. R. Matthews, C. E. Wieman, and E. A. Cornell, "*Observation of Bose-Einstein Condensation in a Dilute Atomic Vapor*", Science, **269**, 198–201 (1995).

[8] C. C. Bradley, C. A. Sackett, J. J. Tollett, and R. G. Hulet, "*Evidence of Bose-Einstein Condensation in an Atomic Gas with Attractive Interactions*", Phys. Rev. Lett., **75**, 1687–1690 (1995).

[9] K. B. Davis, M. O. Mewes, M. R. Andrews, N. J. van Druten, D. S. Durfee, D. M. Kurn, and W. Ketterle, "*Bose-Einstein Condensation in a Gas of Sodium Atoms*", Phys. Rev. Lett., **75**, 3969–3973 (1995).

[10] Dale G. Fried, Thomas C. Killian, Lorenz Willmann, David Landhuis, Stephen C. Moss, Daniel Kleppner, and Thomas J. Greytak, "*Bose-Einstein Condensation of Atomic Hydrogen*", Phys. Rev. Lett., **81**, 3811–3814 (1998).

[11] S. L. Cornish, N. R. Claussen, J. L. Roberts, E. A. Cornell, and C. E. Wieman, "*Stable* ^{85}Rb *Bose-Einstein Condensates with Widely Tunable Interactions*", Phys. Rev. Lett., **85**, 1795–1798 (2000).

[12] G. Modugno, G. Ferrari, G. Roati, R. J. Brecha, A. Simoni, and M. Inguscio, "*Bose-Einstein Condensation of Potassium Atoms by Sympathetic Cooling*", Science, **294**, 1320–1322 (2001).

[13] A. Robert, O. Sirjean, A. Browaeys, J. Poupard, S. Nowak, D. Boiron, C. I. Westbrook, and A. Aspect, "*A Bose-Einstein Condensate of Metastable Atoms*", Science, **292**, 461–464 (2001).

[14] F. Pereira Dos Santos, J. Léonard, Junmin Wang, C. J. Barrelet, F. Perales, E. Rasel, C. S. Unnikrishnan, M. Leduc, and C. Cohen-Tannoudji, "*Bose-Einstein Condensation of Metastable Helium*", Phys. Rev. Lett., **86**, 3459–3462 (2001).

[15] Tino Weber, Jens Herbig, Michael Mark, Hanns-Christoph Nägerl, and Rudolf Grimm, "*Bose-Einstein Condensation of Cesium*", Science, **299**, 232–235 (2003).

[16] Yosuke Takasu, Kenichi Maki, Kaduki Komori, Tetsushi Takano, Kazuhito Honda, Mitsutaka Kumakura, Tsutomu Yabuzaki, and Yoshiro Takahashi, "*Spin-Singlet Bose-Einstein Condensation of Two-Electron Atoms*", Phys. Rev. Lett., **91**, 040404 (2003).

[17] Axel Griesmaier, Jörg Werner, Sven Hensler, Jürgen Stuhler, and Tilman Pfau, "*Bose-Einstein Condensation of Chromium*", Phys. Rev. Lett., **94**, 160401 (2005).

[18] G. Roati, M. Zaccanti, C. D'Errico, J. Catani, M. Modugno, A. Simoni, M. Inguscio, and G. Modugno, "^{39}K *Bose-Einstein Condensate with Tunable Interactions*", Phys. Rev. Lett., **99**, 010403 (2007).

[19] Takeshi Fukuhara, Seiji Sugawa, and Yoshiro Takahashi, "*Bose-Einstein condensation of an ytterbium isotope*", Phys. Rev. A, **76**, 051604 (2007).

[20] Sebastian Kraft, Felix Vogt, Oliver Appel, Fritz Riehle, and Uwe Sterr, "*Bose-Einstein Condensation of Alkaline Earth Atoms:* ^{40}Ca", Phys. Rev. Lett., **103**, 130401 (2009).

[21] Takeshi Fukuhara, Seiji Sugawa, Yosuke Takasu, and Yoshiro Takahashi, "*All-optical formation of quantum degenerate mixtures*", Phys. Rev. A, **79**, 021601 (2009).

[22] Y. N. Martinez de Escobar, P. G. Mickelson, M. Yan, B. J. DeSalvo, S. B. Nagel, and T. C. Killian, "*Bose-Einstein Condensation of* ^{84}Sr", Phys. Rev. Lett., **103**, 200402 (2009).

[23] Simon Stellmer, Meng Khoon Tey, Bo Huang, Rudolf Grimm, and Florian Schreck, "*Bose-Einstein Condensation of Strontium*", Phys. Rev. Lett., **103**, 200401 (2009).

[24] Simon Stellmer, Meng Khoon Tey, Rudolf Grimm, and Florian Schreck, "*Bose-Einstein condensation of* ^{86}Sr", Phys. Rev. A, **82**, 041602 (2010).

[25] P. G. Mickelson, Y. N. Martinez de Escobar, M. Yan, B. J. DeSalvo, and T. C. Killian, "*Bose-Einstein condensation of* ^{88}Sr *through sympathetic cooling with* ^{87}Sr", Phys. Rev. A, **81**, 051601 (2010).

[26] Seiji Sugawa, Rekishu Yamazaki, Shintaro Taie, and Yoshiro Takahashi, "*Bose-Einstein condensate in gases of rare atomic species*", Phys. Rev. A, **84**, 011610 (2011).

[27] Mingwu Lu, Nathaniel Q. Burdick, Seo Ho Youn, and Benjamin L. Lev, "*Strongly Dipolar Bose-Einstein Condensate of Dysprosium*", Phys. Rev. Lett., **107**, 190401 (2011).

[28] K. Aikawa, A. Frisch, M. Mark, S. Baier, A. Rietzler, R. Grimm, and F. Ferlaino, "*Bose-Einstein Condensation of Erbium*", Phys. Rev. Lett., **108**, 210401 (2012).

[29] Yijun Tang, Nathaniel Q. Burdick, Kristian Baumann, and Benjamin L. Lev, "*Bose-Einstein condensation of* ^{162}Dy *and* ^{160}Dy", New J. Phys., **17**, 045006 (2015).

[30] B. DeMarco and D. S. Jin, "*Onset of Fermi Degeneracy in a Trapped Atomic Gas*", Science, **285**, 1703–1706 (1999).

[31] F. Schreck, L. Khaykovich, K. L. Corwin, G. Ferrari, T. Bourdel, J. Cubizolles, and C. Salomon, "*Quasipure Bose-Einstein Condensate Immersed in a Fermi Sea*", Phys. Rev. Lett., **87**, 080403 (2001).

[32] Andrew G. Truscott, Kevin E. Strecker, William I. McAlexander, Guthrie B. Partridge, and Randall G. Hulet, "*Observation of Fermi Pressure in a Gas of Trapped Atoms*", Science, **291**, 2570–2572 (2001).

[33] Takeshi Fukuhara, Yosuke Takasu, Mitsutaka Kumakura, and Yoshiro Takahashi, "*Degenerate Fermi Gases of Ytterbium*", Phys. Rev. Lett., **98**, 030401 (2007).

[34] Shintaro Taie, Yosuke Takasu, Seiji Sugawa, Rekishu Yamazaki, Takuya Tsujimoto, Ryo Murakami, and Yoshiro Takahashi, "*Realization of a* $\mathrm{SU}(2)\times\mathrm{SU}(6)$ *System of Fermions in a Cold Atomic Gas*", Phys. Rev. Lett., **105**, 190401 (2010).

[35] B. J. DeSalvo, M. Yan, P. G. Mickelson, Y. N. Martinez de Escobar, and T. C. Killian, "*Degenerate Fermi Gas of* ^{87}Sr", Phys. Rev. Lett., **105**, 030402 (2010).

[36] Meng Khoon Tey, Simon Stellmer, Rudolf Grimm, and Florian Schreck, "*Double-degenerate Bose-Fermi mixture of strontium*", Phys. Rev. A, **82**, 011608 (2010).

[37] Mingwu Lu, Nathaniel Q. Burdick, and Benjamin L. Lev, "*Quantum Degenerate Dipolar Fermi Gas*", Phys. Rev. Lett., **108**, 215301 (2012).

[38] K. Aikawa, A. Frisch, M. Mark, S. Baier, R. Grimm, and F. Ferlaino, "*Reaching Fermi Degeneracy via Universal Dipolar Scattering*", Phys. Rev. Lett., **112**, 010404 (2014).

[39] D. Jaksch, C. Bruder, J. I. Cirac, C. W. Gardiner, and P. Zoller, "*Cold Bosonic Atoms in Optical Lattices*", Phys. Rev. Lett., **81**, 3108–3111 (1998).

[40] Markus Greiner, Olaf Mandel, Tilman Esslinger, Theodor W. Hänsch, and Immanuel Bloch, "*Quantum phase transition from a superfluid to a Mott insulator in a gas of ultracold atoms*", Nature, **415**, 39–44 (2002).

[41] Thilo Stöferle, Henning Moritz, Christian Schori, Michael Köhl, and Tilman Esslinger, "*Transition from a Strongly Interacting 1D Superfluid to a Mott Insulator*", Phys. Rev. Lett., **92**, 130403 (2004).

[42] I. B. Spielman, W. D. Phillips, and J. V. Porto, "*Mott-Insulator Transition in a Two-Dimensional Atomic Bose Gas*", Phys. Rev. Lett., **98**, 080404 (2007).

[43] U. Schneider, L. Hackermüller, S. Will, T. h. Best, I. Bloch, T. A. Costi, R. W. Helmes, D. Rasch, and A. Rosch, "*Metallic and Insulating Phases of Repulsively Interacting Fermions in a 3D Optical Lattice*", Science, **322**, 1520–1525 (2008).

[44] Robert Jördens, Niels Strohmaier, Kenneth Günter, Henning Moritz, and Tilman Esslinger, "*A Mott insulator of fermionic atoms in an optical lattice*", Nature, **455**, 204–207 (2008).

[45] Karl D. Nelson, Xiao Li, and David S. Weiss, "*Imaging single atoms in a three-dimensional array*", Nat. Phys., **3**, 556–560 (2007).

[46] Waseem S. Bakr, Jonathon I. Gillen, Amy Peng, Simon Fölling, and Markus Greiner, "*A quantum gas microscope for detecting single atoms in a Hubbard-regime optical lattice*", Nature, **462**, 74–77 (2009).

[47] Jacob F. Sherson, Christof Weitenberg, Manuel Endres, Marc Cheneau, Immanuel Bloch, and Stefan Kuhr, "*Single-atom-resolved fluorescence imaging of an atomic Mott insulator*", Nature, **467**, 68–72 (2010).

[48] Waseem S. Bakr, Amy Peng, M. Eric Tai, Ruichao Ma, Jonathan Simon, Jonathon I. Gillen, Simon Foelling, Lode Pollet, and Markus Greiner, "*Probing the Superfluid-to-Mott Insulator Transition at the Single-Atom Level*", Science, **329**, 547–550 (2010).

[49] Christof Weitenberg, Manuel Endres, Jacob F. Sherson, Marc Cheneau, Peter Schausz, Takeshi Fukuhara, Immanuel Bloch, and Stefan Kuhr, "*Single-spin addressing in an atomic Mott insulator*", Nature, **471**, 319–324 (2011).

[50] Jonathan Simon, Waseem S. Bakr, Ruichao Ma, M. Eric Tai, Philipp M. Preiss, and Markus Greiner, "*Quantum simulation of antiferromagnetic spin chains in an optical lattice*", Nature, **472**, 307–312 (2011).

[51] Christof Weitenberg, Peter Schauß, Takeshi Fukuhara, Marc Cheneau, Manuel Endres, Immanuel Bloch, and Stefan Kuhr, "*Coherent Light Scattering from a Two-Dimensional Mott Insulator*", Phys. Rev. Lett., **106**, 215301 (2011).

[52] Ruichao Ma, M. Eric Tai, Philipp M. Preiss, Waseem S. Bakr, Jonathan Simon, and Markus Greiner, "*Photon-Assisted Tunneling in a Biased Strongly Correlated Bose Gas*", Phys. Rev. Lett., **107**, 095301 (2011).

[53] M. Endres, M. Cheneau, T. Fukuhara, C. Weitenberg, P. Schauß, C. Gross, L. Mazza, M. C. Bañuls, L. Pollet, I. Bloch, and S. Kuhr, "*Observation of*

Correlated Particle-Hole Pairs and String Order in Low-Dimensional Mott Insulators", Science, **334**, 200–203 (2011).

[54] Waseem S. Bakr, Philipp M. Preiss, M. Eric Tai, Ruichao Ma, Jonathan Simon, and Markus Greiner, "*Orbital excitation blockade and algorithmic cooling in quantum gases*", Nature, **480**, 500–503 (2011).

[55] Marc Cheneau, Peter Barmettler, Dario Poletti, Manuel Endres, Peter Schauß, Takeshi Fukuhara, Christian Gross, Immanuel Bloch, Corinna Kollath, and Stefan Kuhr, "*Light-cone-like spreading of correlations in a quantum many-body system*", Nature, **481**, 484–487 (2012).

[56] Manuel Endres, Takeshi Fukuhara, David Pekker, Marc Cheneau, Peter Schauß, Christian Gross, Eugene Demler, Stefan Kuhr, and Immanuel Bloch, "*The 'Higgs' amplitude mode at the two-dimensional superfluid/Mott insulator transition*", Nature, **487**, 454–458 (2012).

[57] Peter Schausz, Marc Cheneau, Manuel Endres, Takeshi Fukuhara, Sebastian Hild, Ahmed Omran, Thomas Pohl, Christian Gross, Stefan Kuhr, and Immanuel Bloch, "*Observation of spatially ordered structures in a two-dimensional Rydberg gas*", Nature, **491**, 87–91 (2012).

[58] Takeshi Fukuhara, Adrian Kantian, Manuel Endres, Marc Cheneau, Peter Schausz, Sebastian Hild, David Bellem, Ulrich Schollwock, Thierry Giamarchi, Christian Gross, Immanuel Bloch, and Stefan Kuhr, "*Quantum dynamics of a mobile spin impurity*", Nat. Phys., **9**, 235–241 (2013).

[59] Takeshi Fukuhara, Peter Schausz, Manuel Endres, Sebastian Hild, Marc Cheneau, Immanuel Bloch, and Christian Gross, "*Microscopic observation of magnon bound states and their dynamics*", Nature, **502**, 76–79 (2013).

[60] Sebastian Hild, Takeshi Fukuhara, Peter Schauß, Johannes Zeiher, Michael Knap, Eugene Demler, Immanuel Bloch, and Christian Gross, "*Far-from-Equilibrium Spin Transport in Heisenberg Quantum Magnets*", Phys. Rev. Lett., **113**, 147205 (2014).

[61] Philipp M. Preiss, Ruichao Ma, M. Eric Tai, Alexander Lukin, Matthew Rispoli, Philip Zupancic, Yoav Lahini, Rajibul Islam, and Markus Greiner, "*Strongly correlated quantum walks in optical lattices*", Science, **347**, 1229–1233 (2015).

[62] P. Schauß, J. Zeiher, T. Fukuhara, S. Hild, M. Cheneau, T. Macrì, T. Pohl, I. Bloch, and C. Gross, "*Crystallization in Ising quantum magnets*", Science, **347**, 1455–1458 (2015).

[63] Philipp M. Preiss, Ruichao Ma, M. Eric Tai, Jonathan Simon, and Markus Greiner, "*Quantum gas microscopy with spin, atom-number, and multilayer readout*", Phys. Rev. A, **91**, 041602 (2015).

[64] Takeshi Fukuhara, Sebastian Hild, Johannes Zeiher, Peter Schauß, Immanuel Bloch, Manuel Endres, and Christian Gross, "*Spatially Resolved Detection of a Spin-Entanglement Wave in a Bose-Hubbard Chain*", Phys. Rev. Lett., **115**, 035302 (2015).

[65] Johannes Zeiher, Peter Schauß, Sebastian Hild, Tommaso Macrì, Immanuel Bloch, and Christian Gross, "*Microscopic Characterization of Scalable Coherent Rydberg Superatoms*", Phys. Rev. X, **5**, 031015 (2015).

[66] Rajibul Islam, Ruichao Ma, Philipp M. Preiss, M. Eric Tai, Alexander Lukin, Matthew Rispoli, and Markus Greiner, "*Measuring entanglement entropy in a quantum many-body system*", Nature, **528**, 77–83 (2015).

[67] Johannes Zeiher, Rick van Bijnen, Peter Schauß, Sebastian Hild, Jae-yoon Choi, Thomas Pohl, Immanuel Bloch, and Christian Gross, "*Many-body interferometry of a Rydberg-dressed spin lattice*", arXiv preprint arXiv:1602.06313, (2016).

[68] Adam M Kaufman, M Eric Tai, Alexander Lukin, Matthew Rispoli, Robert Schittko, Philipp M Preiss, and Markus Greiner, "*Quantum thermalization through entanglement in an isolated many-body system*", arXiv preprint arXiv:1603.04409, (2016).

[69] Jae-yoon Choi, Sebastian Hild, Johannes Zeiher, Peter Schauß, Antonio Rubio-Abadal, Tarik Yefsah, Vedika Khemani, David A. Huse, Immanuel Bloch, and Christian Gross, "*Exploring the many-body localization transition in two dimensions*", Science, **352**, 1547–1552 (2016).

[70] Lawrence W. Cheuk, Matthew A. Nichols, Melih Okan, Thomas Gersdorf, Vinay V. Ramasesh, Waseem S. Bakr, Thomas Lompe, and Martin W. Zwierlein, "*Quantum-Gas Microscope for Fermionic Atoms*", Phys. Rev. Lett., **114**, 193001 (2015).

[71] Elmar Haller, James Hudson, Andrew Kelly, Dylan A. Cotta, Bruno Peaudecerf, Graham D. Bruce, and Stefan Kuhr, "*Single-atom imaging of fermions in a quantum-gas microscope*", Nat. Phys., **11**, 738–742 (2015).

[72] G. J. A. Edge, R. Anderson, D. Jervis, D. C. McKay, R. Day, S. Trotzky, and J. H. Thywissen, "*Imaging and addressing of individual fermionic atoms in an optical lattice*", Phys. Rev. A, **92**, 063406 (2015).

[73] Maxwell F. Parsons, Florian Huber, Anton Mazurenko, Christie S. Chiu, Widagdo Setiawan, Katherine Wooley-Brown, Sebastian Blatt, and Markus Greiner, "*Site-Resolved Imaging of Fermionic* ^{6}Li *in an Optical Lattice*", Phys. Rev. Lett., **114**, 213002 (2015).

[74] Ahmed Omran, Martin Boll, Timon A. Hilker, Katharina Kleinlein, Guillaume Salomon, Immanuel Bloch, and Christian Gross, "*Microscopic Observation of Pauli Blocking in Degenerate Fermionic Lattice Gases*", Phys. Rev. Lett., **115**, 263001 (2015).

[75] Daniel Greif, Maxwell F. Parsons, Anton Mazurenko, Christie S. Chiu, Sebastian Blatt, Florian Huber, Geoffrey Ji, and Markus Greiner, "*Site-resolved imaging of a fermionic Mott insulator*", Science, **351**, 953–957 (2016).

[76] Lawrence W. Cheuk, Matthew A. Nichols, Katherine R. Lawrence, Melih Okan, Hao Zhang, and Martin W. Zwierlein, "*Observation of 2D Fermionic Mott Insulators of* ^{40}K *with Single-Site Resolution*", Phys. Rev. Lett., **116**, 235301 (2016).

[77] Martin Boll, Timon A Hilker, Guillaume Salomon, Ahmed Omran, Immanuel Bloch, and Christian Gross, "*Spin and Charge Resolved Quantum Gas Microscopy of Antiferromagnetic Order in Hubbard Chains*", arXiv preprint arXiv:1605.05661, (2016).

[78] Maxwell F Parsons, Anton Mazurenko, Christie S Chiu, Geoffrey Ji, Daniel Greif, and Markus Greiner, "*Site-resolved observations of antiferromagnetic correlations in the Hubbard model*", arXiv preprint arXiv:1605.02704, (2016).

[79] Lawrence W Cheuk, Matthew A Nichols, Katherine R Lawrence, Melih Okan, Hao Zhang, Ehsan Khatami, Nandini Trivedi, Thereza Paiva, Marcos Rigol, and Martin W Zwierlein, "*Observation of Spatial Charge and Spin Correlations in the 2D Fermi-Hubbard Model*", arXiv preprint arXiv:1606.04089, (2016).

[80] Ryuta Yamamoto, Jun Kobayashi, Takuma Kuno, Kohei Kato, and Yoshiro Takahashi, "*An ytterbium quantum gas microscope with narrow-line laser cooling*", New J. Phys., **18**, 023016 (2016).

[81] J. Dalibard and C. Cohen-Tannoudji, "*Laser cooling below the Doppler limit by polarization gradients: simple theoretical models*", J. Opt. Soc. Am. B, **6**, 2023–2045 (1989).

[82] C. Monroe, D. M. Meekhof, B. E. King, S. R. Jefferts, W. M. Itano, D. J. Wineland, and P. Gould, "*Resolved-Sideband Raman Cooling of a Bound Atom to the 3D Zero-Point Energy*", Phys. Rev. Lett., **75**, 4011–4014 (1995).

[83] S. E. Hamann, D. L. Haycock, G. Klose, P. H. Pax, I. H. Deutsch, and P. S. Jessen, "*Resolved-Sideband Raman Cooling to the Ground State of an Optical Lattice*", Phys. Rev. Lett., **80**, 4149–4152 (1998).

[84] Vladan Vuletić, Cheng Chin, Andrew J. Kerman, and Steven Chu, "*Degenerate Raman Sideband Cooling of Trapped Cesium Atoms at Very High Atomic Densities*", Phys. Rev. Lett., **81**, 5768–5771 (1998).

[85] Andrew J. Kerman, Vladan Vuletić, Cheng Chin, and Steven Chu, "*Beyond Optical Molasses: 3D Raman Sideband Cooling of Atomic Cesium to High Phase-Space Density*", Phys. Rev. Lett., **84**, 439–442 (2000).

[86] Dian-Jiun Han, Steffen Wolf, Steven Oliver, Colin McCormick, Marshall T. DePue, and David S. Weiss, "*3D Raman Sideband Cooling of Cesium Atoms at High Density*", Phys. Rev. Lett., **85**, 724–727 (2000).

[87] A. M. Kaufman, B. J. Lester, and C. A. Regal, "*Cooling a Single Atom in an Optical Tweezer to Its Quantum Ground State*", Phys. Rev. X, **2**, 041014 (2012).

[88] J. D. Thompson, T. G. Tiecke, A. S. Zibrov, V. Vuletić, and M. D. Lukin, "*Coherence and Raman Sideband Cooling of a Single Atom in an Optical Tweezer*", Phys. Rev. Lett., **110**, 133001 (2013).

[89] Y. S. Patil, S. Chakram, L. M. Aycock, and M. Vengalattore, "*Nondestructive imaging of an ultracold lattice gas*", Phys. Rev. A, **90**, 033422 (2014).

[90] Giovanna Morigi, Jürgen Eschner, and Christoph H. Keitel, "*Ground State Laser Cooling Using Electromagnetically Induced Transparency*", Phys. Rev. Lett., **85**, 4458–4461 (2000).

[91] Giovanna Morigi, "*Cooling atomic motion with quantum interference*", Phys. Rev. A, **67**, 033402 (2003).

[92] D. J. Wineland and Wayne M. Itano, "*Laser cooling of atoms*", Phys. Rev. A, **20**, 1521–1540 (1979).

[93] D. J. Wineland, Wayne M. Itano, J. C. Bergquist, and Randall G. Hulet, "*Laser-cooling limits and single-ion spectroscopy*", Phys. Rev. A, **36**, 2220–2232 (1987).

[94] F. Diedrich, J. C. Bergquist, Wayne M. Itano, and D. J. Wineland, "*Laser Cooling to the Zero-Point Energy of Motion*", Phys. Rev. Lett., **62**, 403–406 (1989).

[95] P. D. Lett, W. D. Phillips, S. L. Rolston, C. E. Tanner, R. N. Watts, and C. I. Westbrook, "*Optical molasses*", J. Opt. Soc. Am. B, **6**, 2084–2107 (1989).

[96] M. A. Cazalilla, A. F. Ho, and M Ueda, "*Ultracold gases of ytterbium: Ferromagnetism and Mott states in an SU (6) Fermi system*", New J. Phys., **11**, 103033 (2009).

[97] Shintaro Taie, Rekishu Yamazaki, Seiji Sugawa, and Yoshiro Takahashi, "*An SU (6) Mott insulator of an atomic Fermi gas realized by large-spin Pomeranchuk cooling*", Nat. Phys., **8**, 825–830 (2012).

[98] Kaden R. A. Hazzard, Victor Gurarie, Michael Hermele, and Ana Maria Rey, "*High-temperature properties of fermionic alkaline-earth-metal atoms in optical lattices*", Phys. Rev. A, **85**, 041604 (2012).

[99] Guido Pagano, Marco Mancini, Giacomo Cappellini, Pietro Lombardi, Florian Schäfer, Hui Hu, X. i. a. . J. i. Liu, Jacopo Catani, Carlo Sias, Massimo Inguscio, and Leonardo Fallani, "*A one-dimensional liquid of fermions with tunable spin*", Nat. Phys., **10**, 198–201 (2014).

[100] A. V. Gorshkov, M Hermele, V Gurarie, C Xu, P. S. Julienne, J Ye, P Zoller, E Demler, M. D. Lukin, and A. M. Rey, "*Two-orbital SU (N) magnetism with ultracold alkaline-earth atoms*", Nat. Phys., **6**, 289–295 (2010).

[101] Francesco Scazza, Christian Hofrichter, Moritz Höfer, P. C. De Groot, Immanuel Bloch, and Simon Fölling, "*Observation of two-orbital spin-exchange interactions with ultracold SU (N)-symmetric fermions*", Nat. Phys., **10**, 779–784 (2014).

[102] X Zhang, M Bishof, S. L. Bromley, C. V. Kraus, M. S. Safronova, P Zoller, A. M. Rey, and J Ye, "*Spectroscopic observation of SU (N)-symmetric interactions in Sr orbital magnetism*", Science, **345**, 1467–1473 (2014).

[103] G. Cappellini, M. Mancini, G. Pagano, P. Lombardi, L. Livi, M. Siciliani de Cumis, P. Cancio, M. Pizzocaro, D. Calonico, F. Levi, C. Sias, J. Catani, M. Inguscio, and L. Fallani, "*Direct Observation of Coherent Interorbital Spin-Exchange Dynamics*", Phys. Rev. Lett., **113**, 120402 (2014).

[104] M. Mancini, G. Pagano, G. Cappellini, L. Livi, M. Rider, J. Catani, C. Sias, P. Zoller, M. Inguscio, M. Dalmonte, and L. Fallani, "*Observation of chiral edge states with neutral fermions in synthetic Hall ribbons*", Science, **349**, 1510–1513 (2015).

[105] Simon Stellmer, Rudolf Grimm, and Florian Schreck, "*Production of quantum-degenerate strontium gases*", Phys. Rev. A, **87**, 013611 (2013).

[106] Seiji Sugawa, Kensuke Inaba, Shintaro Taie, Rekishu Yamazaki, Makoto Yamashita, and Yoshiro Takahashi, "*Interaction and filling-induced quantum phases of dual Mott insulators of bosons and fermions*", Nat. Phys., **7**, 642–648 (2011).

[107] Andrei Derevianko and Caleb C. Cannon, "*Quantum computing with magnetically interacting atoms*", Phys. Rev. A, **70**, 062319 (2004).

[108] Andrew J. Daley, Martin M. Boyd, Jun Ye, and Peter Zoller, "*Quantum Computing with Alkaline-Earth-Metal Atoms*", Phys. Rev. Lett., **101**, 170504 (2008).

[109] A. V. Gorshkov, A. M. Rey, A. J. Daley, M. M. Boyd, J. Ye, P. Zoller, and M. D. Lukin, "*Alkaline-Earth-Metal Atoms as Few-Qubit Quantum Registers*", Phys. Rev. Lett., **102**, 110503 (2009).

[110] K. Shibata, S. Kato, A. Yamaguchi, S. Uetake, and Y. Takahashi, "*A scalable quantum computer with ultranarrow optical transition of ultracold neutral atoms in an optical lattice*", Appl. Phys. B, **97**, 753–758 (2009).

[111] Shinya Kato, Seiji Sugawa, Kosuke Shibata, Ryuta Yamamoto, and Yoshiro Takahashi, "*Control of Resonant Interaction between Electronic Ground and Excited States*", Phys. Rev. Lett., **110**, 173201 (2013).

[112] Shintaro Taie, Shunsuke Watanabe, Tomohiro Ichinose, and Yoshiro Takahashi, "*Feshbach-Resonance-Enhanced Coherent Atom-Molecule Conversion*

with Ultranarrow Photoassociation Resonance", Phys. Rev. Lett., **116**, 043202 (2016).

[113] A. Yamaguchi, S. Uetake, S. Kato, H. Ito, and Y. Takahashi, "*High-resolution laser spectroscopy of a Bose-Einstein condensate using the ultranarrow magnetic quadrupole transition*", New J. Phys., **12**, 103001 (2010).

[114] Shinya Kato, Kensuke Inaba, Seiji Sugawa, Kosuke Shibata, Ryuta Yamamoto, Makoto Yamashita, and Yoshiro Takahashi, "*Laser spectroscopic probing of coexisting superfluid and insulating states of an atomic Bose-Hubbard system*", Nat. Commun., **7**, – (2016).

[115] J. Millen, G. Lochead, and M. P. A. Jones, "*Two-Electron Excitation of an Interacting Cold Rydberg Gas*", Phys. Rev. Lett., **105**, 213004 (2010).

[116] P. McQuillen, X. Zhang, T. Strickler, F. B. Dunning, and T. C. Killian, "*Imaging the evolution of an ultracold strontium Rydberg gas*", Phys. Rev. A, **87**, 013407 (2013).

[117] R Mukherjee, J Millen, R Nath, M. P. A. Jones, and T Pohl, "*Many-body physics with alkaline-earth Rydberg lattices*", J. Phys. B: At., Mol. Opt. Phys., **44**, 184010 (2011).

[118] Takeshi Fukuhara, Seiji Sugawa, Masahito Sugimoto, Shintaro Taie, and Yoshiro Takahashi, "*Mott insulator of ultracold alkaline-earth-metal-like atoms*", Phys. Rev. A, **79**, 041604 (2009).

[119] Christine Guerlin, Julien Bernu, Samuel Deleglise, Clement Sayrin, Sebastien Gleyzes, Stefan Kuhr, Michel Brune, Jean-Michel Raimond, and Serge Haroche, "*Progressive field-state collapse and quantum non-demolition photon counting*", Nature, **448**, 889–893 (2007).

[120] Clement Sayrin, Igor Dotsenko, Xingxing Zhou, Bruno Peaudecerf, Theo Rybarczyk, Sebastien Gleyzes, Pierre Rouchon, Mazyar Mirrahimi, Hadis Amini, Michel Brune, Jean-Michel Raimond, and Serge Haroche, "*Real-time quantum feedback prepares and stabilizes photon number states*", Nature, **477**, 73–77 (2011).

[121] Greg A. Smith, Souma Chaudhury, Andrew Silberfarb, Ivan H. Deutsch, and Poul S. Jessen, "*Continuous Weak Measurement and Nonlinear Dynamics in a Cold Spin Ensemble*", Phys. Rev. Lett., **93**, 163602 (2004).

[122] J. Appel, P. J. Windpassinger, D. Oblak, U. B. Hoff, N. Kjærgaard, and E. S. Polzik, "*Mesoscopic atomic entanglement for precision measurements beyond the standard quantum limit*", Proc. Natl. Acad. Sci. U.S.A., **106**, 10960–10965 (2009).

[123] T. Takano, M. Fuyama, R. Namiki, and Y. Takahashi, "*Spin Squeezing of a Cold Atomic Ensemble with the Nuclear Spin of One-Half*", Phys. Rev. Lett., **102**, 033601 (2009).

[124] Monika H. Schleier-Smith, Ian D. Leroux, and Vladan Vuletić, "*States of an Ensemble of Two-Level Atoms with Reduced Quantum Uncertainty*", Phys. Rev. Lett., **104**, 073604 (2010).

[125] R. J. Sewell, M. Koschorreck, M. Napolitano, B. Dubost, N. Behbood, and M. W. Mitchell, "*Magnetic Sensitivity Beyond the Projection Noise Limit by Spin Squeezing*", Phys. Rev. Lett., **109**, 253605 (2012).

[126] Ryotaro Inoue, Shin-Ichi-Ro Tanaka, Ryo Namiki, Takahiro Sagawa, and Yoshiro Takahashi, "*Unconditional Quantum-Noise Suppression via Measurement-Based Quantum Feedback*", Phys. Rev. Lett., **110**, 163602 (2013).

[127] Kevin C. Cox, Graham P. Greve, Joshua M. Weiner, and James K. Thompson, "*Deterministic Squeezed States with Collective Measurements and Feedback*", Phys. Rev. Lett., **116**, 093602 (2016).

[128] K. W. Murch, S. J. Weber, C. Macklin, and I. Siddiqi, "*Observing single quantum trajectories of a superconducting quantum bit*", Nature, **502**, 211–214 (2013).

[129] Syed Abdullah Aljunid, Meng Khoon Tey, Brenda Chng, Timothy Liew, Gleb Maslennikov, Valerio Scarani, and Christian Kurtsiefer, "*Phase Shift of a Weak Coherent Beam Induced by a Single Atom*", Phys. Rev. Lett., **103**, 153601 (2009).

[130] A. Jechow, B. G. Norton, S. Händel, V. Blūms, E. W. Streed, and D. Kielpinski, "*Controllable Optical Phase Shift Over One Radian from a Single Isolated Atom*", Phys. Rev. Lett., **110**, 113605 (2013).

[131] C. J. Hood, M. S. Chapman, T. W. Lynn, and H. J. Kimble, "*Real-Time Cavity QED with Single Atoms*", Phys. Rev. Lett., **80**, 4157–4160 (1998).

[132] P. Maunz, T. Puppe, I. Schuster, N. Syassen, P. W. H. Pinkse, and G. Rempe, "*Cavity cooling of a single atom*", Nature, **428**, 50–52 (2004).

[133] J. D. Thompson, T. G. Tiecke, N. P. de Leon, J. Feist, A. V. Akimov, M. Gullans, A. S. Zibrov, V. Vuletić, and M. D. Lukin, "*Coupling a Single Trapped Atom to a Nanoscale Optical Cavity*", Science, **340**, 1202–1205 (2013).

[134] Yuto Ashida, Shunsuke Furukawa, and Masahito Ueda, "*Quantum critical behavior influenced by measurement backaction in ultracold gases*", arXiv preprint arXiv:1605.06899, (2016).

[135] J. E. Sansonetti and W. C. Martin, "*Handbook of Basic Atomic Spectroscopic Data*", J. Phys. Chem. Ref. Data, **34**, 1559–2259 (2005).

[136] Masaaki Kitagawa, Katsunari Enomoto, Kentaro Kasa, Yoshiro Takahashi, Roman Ciuryło, Pascal Naidon, and Paul S. Julienne, "*Two-color photoassociation spectroscopy of ytterbium atoms and the precise determinations of s-wave scattering lengths*", Phys. Rev. A, **77**, 012719 (2008).

[137] Rudolf Grimm, Matthias Weidemller, and Yurii B. Ovchinnikov. "*Optical Dipole Traps for Neutral Atoms*". volume 42 of *Advances In Atomic, Molecular, and Optical Physics*, pages 95 – 170. Academic Press, (2000).

[138] Fam Le Kien, Philipp Schneeweiss, and Arno Rauschenbeutel, "*Dynamical polarizability of atoms in arbitrary light fields: general theory and application to cesium*", Eur. Phys. J. D, **67** (2013).

[139] 富田 隆文, "散逸により誘起される光格子中 *Bose* 気体の強相関状態", Master's thesis, Kyoto University, (2015).

[140] Lukas Novotny and Bert Hecht. "*Principles of nano-optics*". Cambridge university press, (2012).

[141] S. Kato, K. Shibata, R. Yamamoto, Y. Yoshikawa, and Y. Takahashi, "*Optical magnetic resonance imaging with an ultra-narrow optical transition*", Appl. Phys. B, **108**, 31–38 (2012).

[142] Kosuke Shibata, Ryuta Yamamoto, and Yoshiro Takahashi, "*High-Sensitivity In situ Fluorescence Imaging of Ytterbium Atoms in a Two-Dimensional Optical Lattice with Dual Optical Molasses*", J. Phys. Soc. Jpn., **83**, 014301 (2014).

[143] Jeongwon Lee, Jae Hoon Lee, Jiho Noh, and Jongchul Mun, "*Core-shell magneto-optical trap for alkaline-earth-metal-like atoms*", Phys. Rev. A, **91**, 053405 (2015).

[144] EranA. Mukamel, Hazen Babcock, and Xiaowei Zhuang, "*Statistical Deconvolution for Superresolution Fluorescence Microscopy*", Biophys. J., **102**, 2391–2400 (2012).

[145] K. Honda, Y. Takahashi, T. Kuwamoto, M. Fujimoto, K. Toyoda, K. Ishikawa, and T. Yabuzaki, "*Magneto-optical trapping of Yb atoms and a limit on the branching ratio of the* $^1P_1$ *state*", Phys. Rev. A, **59**, R934–R937 (1999).

[146] Meng Khoon Tey, Gleb Maslennikov, Timothy C. H. Liew, Syed Abdullah Aljunid, Florian Huber, Brenda Chng, Zilong Chen, Valerio Scarani, and Christian Kurtsiefer, "*Interfacing light and single atoms with a lens*", New J. Phys., **11**, 043011 (2009).

[147] C.A. Sackett, C.C. Bradley, M. Welling, and R.G. Hulet, "*Bose–Einstein condensation of lithium*", Appl. Phys. B, **65**, 433–440 (1997).

[148] Miroslav Gajdacz, Poul L. Pedersen, Troels Mørch, Andrew J. Hilliard, Jan Arlt, and Jacob F. Sherson, "*Non-destructive Faraday imaging of dynamically controlled ultracold atoms*", Rev. Sci. Instrum., **84** (2013).

[149] Meng Khoon Tey, Zilong Chen, Syed Abdullah Aljunid, Brenda Chng, Florian Huber, Gleb Maslennikov, and Christian Kurtsiefer, "*Strong interaction between light and a single trapped atom without the need for a cavity*", Nat. Phys., **4**, 924–927 (2008).

[150] Erik W. Streed, Andreas Jechow, Benjamin G. Norton, and David Kielpinski, "*Absorption imaging of a single atom*", Nat. Commun., **3**, 933– (2012).

[151] Y. Takahashi, K. Honda, N. Tanaka, K. Toyoda, K. Ishikawa, and T. Yabuzaki, "*Quantum nondemolition measurement of spin via the paramagnetic Faraday rotation*", Phys. Rev. A, **60**, 4974–4979 (1999).

[152] Alex Kuzmich and Eugene S. Polzik. "*Atomic Continuous Variable Processing and Light-Atoms Quantum Interface*", pages 231–265. Springer Netherlands, Dordrecht, (2003).

[153] Peter J. Mohr, Barry N. Taylor, and David B. Newell, "*CODATA recommended values of the fundamental physical constants: 2010**", Rev. Mod. Phys., **84**, 1527–1605 (2012).

Acknowledgments

本論文は数多くの方々にご指導、ご協力いただくことで書き上げることができました。この場でご指導、ご協力いただいた皆さまに心より感謝を申し上げたいと思います。

高橋義朗教授には学部 4 回生 (Q6) のときより数えて 7 年間もの間懇切丁寧なご指導をしていただきました。私が右も左もわからない Q6 のときに非常に魅力的かつ最先端の実験テーマを提案していただいたことで私の研究は非常に充実したものとなりました。また研究が行き詰まらないように常に適切な助言をいただき、最終的に本論文の成果を達成することができましたのは高橋義朗教授のおかげです。本当にありがとうございました。

小林淳特定准教授にはイッテルビウム原子の量子気体顕微鏡を実現する上で数多くの助言をいただき、ありがとうございました。その中でも実験結果に対する物理的考察は、非常に勉強になることばかりで量子気体顕微鏡を実現する上で欠かすことのできないものでした。

高須洋介助教と吉川豊助教には、スタッフとして研究室運営を支えていただき、ありがとうございました。特に高須洋介助教には、実験装置のトラブルの際に非常に頼りにさせていただき、心より感謝しています。

加藤真也博士 (現在は早稲田大学青木隆朗研究室にて博士研究員をされている) とは、実際に一緒に実験をした期間はそれほど長くありませんでしたが、実験を行う上での心構えを教えていただきました。教えていただいた心構えは今でも私の研究生活の根幹を支えるものとなっています。ありがとうございます。

柴田康介博士 (現在は中央大学東條研究室の助教) とは、最も長い期間 (私が Q6 の時から博士課程 2 回生までの 5 年間) 一緒に実験を行い、様々なことを教えていただき、ありがとうございました。実験の進め方や実験に粘り強く取り組む姿勢などは真似ができないほどのもので私の目標とするところです。また、あっという間に実験の理論考察や計算もなされて、ただただ敬服していました。柴田康介博士と一緒に実験をすることができたのは私にとって非常に幸運なことでした。

加藤宏平博士 (現在は大阪市立大学井上研究室の助教) は、ほんの 1 年間ではありましたが、一緒に実験を行い、また非常に有意義な実験の議論をすることができました。また論文執筆時には、多大なアドバイスをいただきました。ありがとうございました。

蔡恩美博士は、私が博士論文を執筆しはじめてから QGM グループに参加されたのでまだあまり一緒に実験をしていませんが、それでもすでに様々なプロジェクトを進められており、これからの QGM グループを引っ張っていかれるものと思います。

久野拓馬くんとは 2 年と半年の間一緒に実験をしてきました。年末の実験で単一の Yb 原子を一緒にはじめて観測した瞬間は私の研究生活で一生忘れられないものになるでしょう。また他のグループと実験装置（レーザーなど）をシェアしていたり、私の切羽詰まった状況のために土日祝日も関係ない実験スケジュールに付き合わせてしまって申し訳ありませんでした。久野くんはこの 4 月に日立研究所に就職されましたが、一緒に過ごしたこの研究生活を少しでも仕事に活かしていってもらえたら嬉しいです。

山中修也くんと櫻勇人くんとは、まだほんのわずかしか一緒に実験をしていませんが理解力も高く、非常に優秀で頼もしく思っています。今後もこの調子で実験をしていってもらえたら、と思います。

上に名前を挙げていない、現在研究室に在籍している、および過去に研究室に在籍していたメンバーのみなさまとも日々非常に有意義な議論をさせていただき、よい刺激をいただくことができました。そのおかげで楽しく研究生活を過ごすことができました。ありがとうございました。

秘書の清水秀世さん、寺川公美子さんには物品購入や学会参加を含む出張手続きなどさまざまな事務手続きをしていただきました。私が事務処理についてよく理解していないせいでご迷惑をおかけしたことも度々あったと思いますが、事務手続きをしていただいたことで実験に集中して取り組むことができました。ありがとうございました。

物理学教室の用務員の内藤さんには、折に触れては体調を気にしてくださり、ありがとうございました。

また、修士課程では日本学生支援機構より、博士課程の 2 回生と 3 回生では日本学術振興会より経済的な援助をいただけたことに深く感謝いたします。

最後に、博士課程に進学しました私を陰ながら支えてくれた家族に心より感謝いたします。

2016 年 8 月某日

山本 隆太